

Damage in Models of Fracture Nucleation and Propagation

By

JOSEPH DANIEL GRAN
B.S. (California State University, Chico) 2007
M.S. (University of California, Davis) 2008

DISSERTATION

Submitted in partial satisfaction of the requirements for the degree of

Doctor of Philosophy

in

Physics

in the

OFFICE OF GRADUATE STUDIES

of the

UNIVERSITY OF CALIFORNIA

DAVIS

Approved:

John B. Rundle, Chair

James P. Crutchfield

Donald L. Turcotte
Committee in Charge

2011

Damage in Models of Fracture Nucleation and Propagation

COPYRIGHT © 2011

by

JOSEPH DANIEL GRAN

Joseph Daniel Gran

June 2011

Physics

Damage in Models of Fracture Nucleation and Propagation

Abstract

Damage and healing are modeled as a generalized phase transitions including both scaling behaviors and nucleation processes that lead to sudden catastrophic failure. We examine this process in several models of faults in the earth's crust that demonstrate aspects of scaling behavior similar to those seen in experiments and in nature. First, we construct a composite model for earthquake rupture initiation and propagation. Similar to a fiber-bundle model, we assign a time-to-failure for each element from a Poisson distribution. System failure times and modes of rupture propagation are determined as a function of the hazard-rate exponent and the range of interaction. Second, we study a model for frictional sliding with long range interactions and recurrent damage that is parameterized by a process of damage and partial healing during sliding. We show there is a critical point transition and provide a mapping to the mean-field percolation transition (spinodal nucleation). Third, we propose a time-dependent slider-block model which incorporates a time-to-failure function dependent on stress. We associate this new time dependent failure mechanism with stress fatigue. We show the resulting behavior produces both the Gutenberg-Richter scaling law for event sizes and the Omori's scaling law for the rate of aftershocks when we use a power-law time-to-failure function. And last, we discuss a general model for fracture nucleation and growth. We determine the phase diagram and growth modes numerically using a Metropolis algorithm. Distinct modes of fracture nucleation and propagation are seen under certain model parameters. Simulation experiments include a continuous slow loading and instantaneous load quenches. We also model repulsive interactions and compare the resulting symmetry breaking transitions to the anti-ferromagnetic Ising model.

*“To my family and friends
that love me ...*

And to those who appreciate science.”

Acknowledgments

This research has been supported by a grant from the U.S. Department of Energy, Office of Basic Energy Sciences to the University of California, Davis, DE-FG03-95ER14499.

Contents

List of Figures	viii
List of Tables	xiii
Foreword	xiv
1 Introduction	1
1.1 Overview	1
1.2 Statistical Physics Framework	2
1.2.1 Continuous Transitions	4
1.2.2 Classical Nucleation Transitions	6
1.2.3 Spinodal Decomposition/Continuous Ordering	7
1.2.4 Nucleation Near the Spinodal	8
1.3 Evidence of Phase Transitions in Fracture	10
1.3.1 Experimental Data	10
1.3.2 Earthquakes	12
1.4 Numerical Models	15
1.4.1 Fiber-bundle Model	16
1.4.2 Slider-block Model	16
1.4.3 Ising Model	18
1.5 Implementation	19
1.6 References	20
2 A damage-mechanics model for fracture nucleation and propagation	23
2.1 Introduction	23
2.2 The Model	24
2.3 Mean Field Analysis	27
2.4 Simulations	28
2.5 Discussion	34
2.6 References	35
3 A damage model based on failure threshold weakening	37
3.1 Introduction	37
3.2 Model Definition	39

3.2.1	Base Model	41
3.2.2	Threshold damage model	43
3.3	Simulation Results	47
3.4	Analysis	49
3.4.1	Scaling in non-equilibrium systems	49
3.4.2	Ergodic Dynamics	50
3.5	Discussion	51
3.6	References	54
4	A possible mechanism for aftershocks: Damage and time-dependent failures	59
4.1	Introduction	59
4.2	The slider-block model	62
4.3	Time-dependent slider-block model	64
4.3.1	Assumptions	65
4.3.2	Dynamics	67
4.4	Simulation Results	68
4.4.1	Power-law time-to-failure	68
4.4.2	Exponential time-to-failure	73
4.5	Discussion and Conclusions	75
4.6	References	77
5	A numerical study of fracture nucleation	80
5.1	Introduction	80
5.2	Free Energy	81
5.3	Cahn-Hilliard-Cook Theory	82
5.4	Simulation Dynamics	85
5.4.1	Ergodicity	85
5.5	Simulation Results I: $G < 0$	86
5.5.1	Runaway fracture nucleation, $b = 0$	88
5.5.2	Nucleation transition to a stable fractured state, $b \neq 0$	94
5.6	Simulation Results II: $G > 0$	96
5.6.1	Originally proposed free energy: $b = 0$	96
5.6.2	Modified free energy: $b \neq 0$	98
5.6.3	$b \neq 0$, $\gamma < 0$	100
5.7	Summary and Discussion	101
5.8	References	102
6	Conclusions	105
6.1	Summary	105

List of Figures

1.1	This is a depiction of a free energy for a continuous phase change. The state of the system is represented by the black dot. Frame (a) is above the critical point ($T > T_c$). Frame (b) is below the critical point and the system now has a non-zero magnetization. As the temperature is lowered further the stable state increases continuously.	4
1.2	This is a depiction of a free energy for an unspecified system. The state of the system is represented by the black dot and in frame (a) is in the globally stable state. Frames (b-e) show a depict the change in shape of the free energy during a slow field reversal. In frame (f) the system a nucleation transition occurs from the metastable state to the lower-energy stable state.	6
1.3	This is an example of a critical quench in the free energy picture. In frame (a) the system is above the critical temperature and in the only available state. In frame (b) a sudden quench to a temperature below the critical value occurs and the system is now in an unstable state. Due to fluctuations the system evolves to one of the two lower-energy stable states in frame (c).	8
1.4	(a,b) Two typical time δt and energy ε distributions obtained at imposed constant pressure ($P = 0.56$ atm). (c) The exponents α_c (empty circles) and β_c (black points), plotted as a function of the value of the imposed constant pressure. Note that as the pressure increases, the values of the exponents tend to those obtained in the case of constant pressure rate. The error bars represent the statistical uncertainty. (Image reproduced with kind permission of The European Physical Journal and Guarino et al. [2])	11
1.5	This is a Gutenberg-Richter distribution for event magnitudes following two main-shock events. The mainshocks are shown in this figure with the oversized dots above magnitude 6. (Image reproduced with kind permission of Geophysical Research Letters and Shcherbakov et al. [19])	13
1.6	This is an Omori's law plot for four different earthquakes in California. (Image reproduced with kind permission of Geophysical Research Letters and Shcherbakov et al. [19])	14
1.7	This is a diagram of the 2D slider-block model with nearest neighbor interactions. The loader plate is moving at velocity v . (Image courtesy of Dr. John Rundle) . . .	17

2.1	Illustration of the model. A square grid of elements with width L is considered, in this case $L = 17$ so that there are $n_0 = 17^2 = 289$ elements. At time $t = 0$ a uniform load F_0 is uniformly distributed to all the elements. The stress σ_0 on each element is $\sigma_0 = F_0/n_0$. One element has the shortest time to failure $t_{f,\min}$, the failure of this element is the solid square. The stress from this failed element is redistributed equally to all the elements within range r . Here $r = 2$ and is represented by the black line surrounding the failed element. The stress is redistributed equally to the 24 remaining elements within the square.	25
2.2	Three examples of rupture nucleation and propagation are illustrated. We assume $\rho = 3$, $L = 256$, and consider $r = 1, 8$ and 32 . For each case we give the structure for $\alpha = 0.03, 0.10, 0.30, 0.50$ and 0.70 . The dark areas are failed elements.	29
2.3	Dependence of the damage variable α on the nondimensional time $\nu_0 t$ after the application of the constant applied force. (a) Stress exponent $\rho = 3$. (b) Stress exponent $\rho = 6$. Results are given for ranges of interaction $r = 1, 2, 4, 8, 16, 32$ and 64 (mean field). Also shown is the mean-field solution given in Eq. (2.13).	31
2.4	Dependence of the nondimensional time to failure $\nu_0 t_{gf}$ on the interaction length r . Results are given for stress exponents $\rho = 1, 2, 3, \dots, 8$	33
2.5	Cumulative probability function P_c of failure times t_{gf}/\bar{t}_{gf} for several values of the interaction length r , for $\rho = 6$	33
2.6	Dependence of $1 - \alpha$ on the time prior to failure $1 - t/\bar{t}_{gf}$ for $\rho = 6$ and several values of r	34
3.1	(a) A sequence of event areas A are given as a function of event number (natural time) for zero weakening ($w = 0$). A small segment of the total sequence is shown. The largest events are semi-periodic but are much smaller than the lattice area $L^2 = 512^2 = 262,144$. The other parameters of the model run are: $\sigma_F = 100$, $\sigma_R = 25 \pm 25$, $R = 15$ ($q = 960$), $K_C/K_L = 0.10$. (b) Frequency-magnitude statistics for weakening parameter $w = 0$. The frequency of events of area A , is plotted as a function of area A . The smaller events correlate well with the mean-field scaling relation taking $\tau - 1 = 1.49 \pm .01$	42
3.2	A sequence of 1000 event areas A are given as a function of event number N (natural time) for two values of the weakening parameter ($w > w_c$). We show the event sequence for (a) $w = 0.016$ and (b) $w = 0.04$. Comparing this figure to Figure 1(a) illustrates the transition through the critical point, where below the critical point no system wide events occur and above the critical point system wide events occur and grow in frequency as w is increased. System-wide events $A = L^2 = 512^2 = 262,144$ occur quasi-periodically and increase in frequency as w is increased.	44

3.3	Frequency-magnitude statistics for three values of the weakening parameter: $w = w_c$ and two cases where $w > w_c$. The frequency of events of area A , is plotted as a function of area A . At the critical point $w = w_c = 0.012$ there are no system-wide events and the smaller events correlate well with equation 2.3 taking $\tau - 1 = 1.47 \pm .05$. Slightly above the critical point $w = 0.016$ large events begin to appear and there is a non-zero probability of system-wide events occurring. Far beyond the critical point $w = 0.04$ there are system-wide events occurring regularly producing the spike (lone red dot) at $A = 262, 144$, while the smaller events continue to obey the GR scaling relationship with τ very near 2.5.	45
3.4	The order parameter vs the weakening value adjusted by the critical weakening value. The order parameter is defined as the probability of of a system wide event occurring. The plot is on a logarithmic scale emphasizing the power-law dependence of $P(w - w_c)$ with a scaling exponent very near $\beta = 1$. The parameters of the model are the same as in Fig. 3.1.	48
3.5	The inverse TM metric for measuring effective ergodicity is overlayed with the event size sequence as a function of loader plate position, for the "threshold damage model" at the critical point $w = w_c$. A system is effectively ergodic if the stress metric decreases as $1/t$. In (a) we plot the inverse TM metric vs loader plate position (time). This plot shows a linear trend, displaying the system is effectively ergodic from $Vt = 300 - 600$. In (b), we show a detailed view of a break in the ergodicity caused by a large event.	52
3.6	The inverse TM metric and the event size sequence are shown for the "threshold damage model" above the critical point ($w > w_c$). The inverse metric shows a t^2 trend, displaying that this model is not ergodic over the observed time period. The grid-size events, shown with "dots", prevent the system from residing in a meta-stable equilibrium for any extended period of time.	52
4.1	The Gutenberg-Richter scaling for the CA slider-block model with long range interactions is shown here. The scaling relationship shows a scaling exponent of approximately $b' = 1.5$. This agrees previously published results [5]	63
4.2	Here we plot the failure-time functions given in Eqs. (4.10) and (4.11). A time-to-failure is assigned to blocks only if the stress on that block is above the damage threshold, σ_W and below a static failure threshold, σ_F . Above σ_F the time-to-failure is zero and below the damage threshold, σ_W , the time-to-failure is infinite. Here we plot two failure-time functions, a power-law and an exponential. The values of σ_W and σ_F are 97 and 100 respectively, for both functions.	66
4.3	A plot of the magnitude of events vs time. The loader-plate update occurs at $t = 0$ and the mainshock of this sequence occurs a short time later. There are several foreshocks and a long sequence of aftershocks. The aftershocks continue past $t = 100$ but the sequence was truncated for illustrative purposes. The parameters of the model used to produce this time line are the same as those in Fig. 4.1, with $\frac{\sigma_W}{\sigma_F} = 0.97$ and $\rho = 2$	69

4.4	The Gutenberg-Richter scaling for all events during 75 loader-plate updates. This includes the foreshocks, mainshock and aftershocks of each cluster of events. The data is shown as a probability distribution rather than a cumulative distribution function. The corresponding CDF scaling exponent is 1 less than the PDF, which gives a b-value of roughly 0.94. This corresponds well with recorded data for earthquakes.	70
4.5	The number of events following the mainshock are binned and plotted. The bin width here is near 1 unit of time. The mainshock is defined as the largest event area in the sequence after 1 loader-plate update. The data is binned into 1000 equally spaced bins and fit to a power-law. This data is the sum of aftershocks following 75 loader-plate updates. The scaling exponent is $p \approx 1$, which corresponds well with observed values for Omori's law scaling in earthquakes.	72
4.6	A histogram of the ratio of the area of the mainshock over the area of the largest aftershock is shown here. Bath's law suggests that this ratio should correspond to 1 magnitude unit on the Gutenberg-Richter scale.	72
4.7	Various Omori's law scaling exponents, p -values, are plotted for failure-time exponents $\rho = 1 - 4$ as a function of the damage threshold. Each data point reported here is calculated ignoring events of size 1.	74
4.8	Rates of aftershocks for the model using an exponential failure-time function are plotted here. In certain cases there is a well-defined scaling region with a p -value near 1. In other cases the scaling region is significantly reduced in size or non-existent. 76	
5.1	The phase diagram for our model is shown for $b = 0$. We include here both positive and negative interactions. There are four regions to the phase space. Region I has an applied load smaller than the spinodal value p_{sp} and allows fracture to occur via nucleation. Region II has an applied load larger than the spinodal value and thus the free energy has no metastable state. Nucleation does not occur in Region II. If $G < -4$, the free energy curve has no metastable state for all $p > 0$. Regions III has only a single globally stable state and allows only stable uniform positive offsets. Region IV has temperature dependent symmetry breaking phase transitions that result in a lattice structure of sites with positive offset. This is discussed in Sec. 5.6.	87
5.2	The free energy plot illustrates that as p is increased the metastable well vanishes leaving a transition to the lower energy state without nucleation. Nucleation from the metastable well leads to a runaway fracture state.	88
5.3	The average offset for a simulation is plotted against MCS with "crosses". Nucleation occurs and the system transitions to the lower energy state at a larger offset. The inverse TM metric is plotted with "x's" for the same simulation. The linear trend of the TM metric indicates the system is ergodic while in the metastable state, ergodicity is broken when nucleation begins. Here we also plot the average offset vs time for two nucleation transitions after intervention has occurred with "boxes" and "asterisks". Intervention prior to nucleation at $t = 25000$ delays nucleation substantially, while intervention post nucleation at $t = 26000$ hardly deviates the failure time. Thus we can say at approximately $t = 25500$, nucleation occurs and catastrophic failure ensues. The intervention technique agrees with time of the break in ergodicity.	90

5.4	Here we plot the nucleating fracture for 3 different scenarios, where time progress to right. The top line we show, $r = 1$ and $G < 0$. The second line is $r = 8$, $G < 0$. The third line shows $r = 8$ and $G > 0$ and shows the lattice structure nucleation pattern that occurs for positive interaction coefficients.	92
5.5	The linear elastic behavior of the model is shown here. The applied load is stress on the system and the average offset of the lattice is the strain. As the loading rate δp is reduced the system fails at a smaller applied load. The horizontal line is the value of stress beyond which there is no metastable well. The parameters used here are $G = -2$, $\gamma = 1$ and $b = .05$	93
5.6	The free energy plot illustrates that as p is increased the metastable well vanishes leaving a transition to the lower energy state without nucleation. In the phase diagram Region I which allow a metastable state is separated from Region II which does not by the spinodal line.	94
5.7	The average offset for a simulation is plotted against time (MCS) with “crosses”. The initial state of the system is zero offset and quickly moves into the meta-stable region. After sitting in the meta-stable state for a period of time, nucleation occurs and the system transitions to the lower energy state at a larger offset. The inverse TM metric is plotted with “x’s” for the same simulation.	95
5.8	Here we the time evolution of the symmetry breaking phase transition for $b = 0$ with repulsive interactions. The initial decay from a uniform offset field, shows the formations of stripes. These stripes decay into clumps and eventually the system stabilizes in an isolated site lattice structure.	97
5.9	Here we plot an approximate phase diagram for the formation of stripes and clumps of positive offset for fixed parameters $\gamma = 1$, $b = 1e - 4$ and at low temperatures approaching $T \rightarrow 0$. These periodic structures occur by a symmetry breaking phase transition only for positive or repulsive interactions, $G > 0$. We normalize the interaction amplitude to the number of neighbors q . The location of the phase boundaries was determined by testing many parameter sets within the phase space.	99
5.10	Here we show the final state of the system after a phase transition has occurred using repulsive interactions. We set the interaction amplitude to $G = 3$ and $b = 1e - 4$. We increase the applied load from the case where only random sites form percolation-type clusters, to that in which the final state is solid well defined stripes. All the final states depicted here are represented in the phase diagram in Fig. 5.9.	100

List of Tables

2.1 Non-dimensional times of transition from the nucleation phase to propagation phase are given for several values of the interaction range r and stress exponent ρ . The transition times are computed by locating the point of maximum curvature in the curves plotted in Fig. 2.3(a) and 2.3(b).	32
---	----

Foreword

This thesis is a compilation of four manuscripts that have either been published or recently submitted to peer reviewed journals. Each manuscript is reproduced here as a chapter of this thesis. An introduction chapter is included which provides an overview of this research, including a motivation provided by laboratory experiments and field observations, as well a brief introduction to the numerical models used to test new damage and fracture ideas. The thesis is organized as follows: Chapter 1 is the introduction described above. Chapter 2 introduces a time-dependent damage model constructed loosely in the fiber-bundle prescription and examines nucleation and propagation of fractures. This manuscript is published in *Theoretical and Applied Fracture Mechanics* Chapters 3 and 4 are damage models constructed by including modifications to the existing long-range cellular automata slider-block model. In chapter 3, a threshold weakening parameter is introduced and subsequent scaling behaviors are examined. This manuscript is published in *Physica A*. In chapter 4, a time-dependent failure mechanism is introduced and the result is a time-series of fracture events that corresponds well with earthquake scaling laws. This manuscript has been submitted to *Geophysical Journal International*. And last, Chapter 5 introduces a generalized fracture model with a corresponding free energy functional, and is numerically simulated using a Metropolis algorithm. This model is the foundation for subsequent studies of failure with the inclusion of damage, imperfections, dislocations and heterogeneous material properties. This manuscript has been submitted to *Physical Review E*. The thesis concludes with chapter 6, a summary of what has been learned by constructing and testing these models.

Chapter 1

Introduction

1.1 Overview

A fundamental understanding of material failure, particularly the lifetime of geologic materials under stress, can be used anywhere from modifying and improving our nation's underground nuclear waste storage facilities, or determining the structural integrity of depleted oil wells, or improving efficiency of hydro-fracture mining, to forecasting and reducing the risk of globally occurring earthquakes. Earthquakes, for example, occur globally with little indication of their location, size or occurrence time prior to rupture. The importance of learning more about this naturally occurring phenomenon which often leads to massive disaster is quite clear. A focus of this research pertains specifically to understanding the precursory events that lead to earthquakes and the aftershocks that follow them. These efforts are geared towards learning more about the nature of these events from a physical perspective to aid methods in forecasting the whereabouts of the next "big" earthquake.

Failure of solid material is a complex phenomenon, which although researched extensively, is not yet well understood. There are several methods of research in this field including: laboratory experiments, field observations and theoretical analysis which often incorporates the use of computer simulations. Laboratory experiments are well controlled and can provide precise data collection. They are, however, limited in the scale of the sample size, the magnitude of applied loads and the amount of energy released due to the confined nature of the laboratory. In addition, they are often performed on pristine samples with little or no flaws which, arguably, is an inaccurate representation of nature. Field observations, on the other hand, can monitor local seismicity from earthquakes and displacement of faults and quantify fracture on a much larger scale. This work is

restricted since we cannot recreate the stress field of the earth's crust prior to an earthquake in order to reproduce the data collected. It is also quite difficult to quantify the exact details and form of the imperfections and defects in faults that certainly influence the resulting fracture or earthquake. The vast difference in length scales from the laboratory to field data, as well as the differences in material structure, leads scientists to question whether the physics that explains these phenomena remains constant in both situations. There have been quite similar results produced from both the laboratory and the observed earthquake data, however. Namely, a Gutenberg-Richter distribution for the frequency of events of a particular size. This power-law distribution was found in experiments on fracture of chipboard panels [1, 2], and in magnitudes of observed earthquakes [3]. This is just one of several scaling-laws observed in regard to fracture and failure of materials.

Inasmuch as scaling laws are often seen in statistical physics of phase transitions, we use this as a foundation for our research. The goal is to describe the fracture process as a generalized phase transition including either nucleation processes or critical point behavior. A focus is on understanding the importance of damage and imperfections in the material and how these alter the fracture process. In addition, there are fundamental relationships that do not yet have physical understanding behind them. One such relationship is Omori's law [4] for the rate of decay of the number of aftershocks and inter-event scaling [2] for fracture experiments. We test our ideas and theories for damage and healing that might lead to scaling laws with numerical models. These simulations provide an excellent framework to repeat calculations, vary initial conditions and compare fracture processes across length scales.

1.2 Statistical Physics Framework

Many systems in nature undergo phase transitions. A phase change can typically be described with an order parameter, constructed to be zero in one state and non-zero in the other. Situations arise where the order parameter is conserved as the system crosses a phase boundary, but this is not of concern in the research presented here. Phase transitions come in two main varieties labeled continuous or discontinuous, referring to the behavior of the order parameter as a function of temperature during the transition [5, 6]. Common phase transitions include the liquid to gas transition of many fluids including water, and the spontaneous magnetization (or paramagnetic to ferromagnetic transition) of certain materials below a Curie temperature. We will use the phase transition in magnetic materials as a reference for this discussion and again in Sec 1.4.3, where we introduce the Ising model.

In a metal, such as iron or nickel, that allows a magnetic phase transition, atoms that form the lattice structure have associated magnetic dipole moments (or “spins”) from the unfilled outermost electron shells. The orientation of these dipole moments is governed by the thermal energy and the influence from the local magnetic field from near-by spins and/or an external magnetic field. The magnetization, m , of the system is the vector sum of all individual dipole moments. This is the order parameter. This magnetization is zero when the dipoles are randomly oriented and takes a maximum value, typically normalized to 1, when the dipoles are all perfectly aligned. A randomly oriented system occurs at high temperatures when the internal thermal energy is large compared with the coupling energy. At the critical temperature T_c , however, the influence of neighboring interactions between spins becomes energetically relevant to the thermal energy and the dipole moments begin to couple. As the temperature is lowered below, T_c , a net magnetization appears, $|m| > 0$. This is the paramagnetic to ferromagnetic phase change. Since the magnetization changes continuously with temperature below, T_c , this is considered a continuous phase change.

Analytically, phase transitions are best understood in the free energy perspective, since thermodynamic states are associated with extrema of the free energy. Following the phenomenological framework originally proposed by Landau and Ginzburg, a free energy functional can be expressed as:

$$\beta f[\phi] = \int d^d \mathbf{x} \left[a_0 (\nabla \phi)^2 + a_1 \phi^2 + a_2 \phi^3 + a_3 \phi^4 + \dots - h\phi \right] \quad (1.1)$$

Here ϕ represents the coarse grained order parameter of the system, and $\nabla \phi$ represents spatial fluctuations, while constants $a_0 - a_3$ can be positive, negative or zero and often depend on the temperature and as usual, $\beta = 1/kT$. Often symmetry constraints, such as the up/down symmetry in the magnetic system, lead coefficients of odd powers of ϕ to be zero. In addition, to maintain finite probabilities in the Boltzmann distribution the coefficient of the highest order term proportional to ϕ must be positive. Higher order terms become increasingly less important in their contribution to the free energy and the non-analyticities that lead to phase changes. Continuous and discontinuous transitions in a magnetic system, for instance, can be described with just a_1, a_3 and h , where a_1 is a function of temperature and a_3 is a constant:

$$f(m) = \frac{t}{2} m^2 + cm^4 - hm \quad (1.2)$$

where t is the distance away from critical point $t = (T - T_c)/T_c$, c is a constant and h is the external applied field. This is a mean-field free energy. When considering a system with long but finite interactions, the fluctuation term must have a non-zero coefficient.

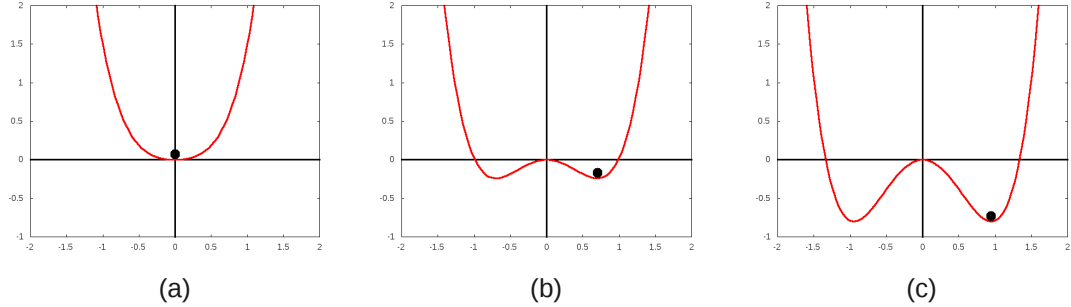


Figure 1.1: This is a depiction of a free energy for a continuous phase change. The state of the system is represented by the black dot. Frame (a) is above the critical point ($T > T_c$). Frame (b) is below the critical point and the system now has a non-zero magnetization. As the temperature is lowered further the stable state increases continuously.

1.2.1 Continuous Transitions

During a continuous phase transition the order parameter evolves from its initial value to its final value in a smooth analytical fashion. A depiction of a continuous phase change in the free energy perspective using Eqn. 1.2 is shown in Figure 1.1. The y-axis is the value of the free energy and the x-axis is the value of order parameter. The state of the system is represented by the solid dot, while the available states are represented by the extrema, locations where the 1st derivative of the free energy is zero. This transition occurs during a quasi-static sweep of a control parameter through the critical point. In Frame (a), above the critical temperature, there is only one available state, a globally stable state at $m = 0$. As the temperature is lowered and the system passes through the critical point, three available states appear. There is an unstable state at $m = 0$ and two stable states at $\pm m$. The system has to choose one of the two low energy stable states, and this process is done randomly. This is shown in Frame (b). The temperature being lowered farther in Frame (c) and the stable state order parameter evolves continuously toward $m = 1$.

Observables in continuous transitions display scaling behavior either above or below the critical point with respect to the control parameters. In the magnetic system the control parameters are the applied field and temperature. The critical point is $T = T_c, h = 0$. The critical field is necessarily zero due to the up/down symmetry of the problem. The order parameter (magnetization)

scales near the critical point:

$$m(T, h = 0) \propto |T - T_c|^\beta \quad (1.3)$$

$$m(T = T_c, h) \propto h^{1/\delta} \quad (1.4)$$

Continuous transitions also display power-law singularities (or divergences) in the response functions [5, 6]. For example the susceptibility in the magnetic system goes as

$$\chi_{\pm}(T, h = 0) \propto |T - T_c|^{-\gamma_{\pm}} \quad (1.5)$$

where the \pm refers to the above and below the critical temperature. The heat capacity also has a singularity at the critical point characterized by the critical exponent α [5, 6]. The divergence of the response functions indicates the behavior macroscopic system is due to long-range correlated fluctuations of the microscopic constituents. The correlations of system can be expressed using a correlation function that decays exponentially with distance as:

$$G(\vec{r}) \propto \exp(-|\vec{r}|/\xi) \quad (1.6)$$

where ξ is the correlation length, or the characteristic length over which fluctuations occur [5, 6]. At the critical point this correlation length diverges:

$$\xi_{\pm}(T, h = 0) \propto |T - T_c|^{-\nu_{\pm}} \quad (1.7)$$

Scaling laws, such as these, are also seen in a critical point phase transition in percolation theory. A common example is site percolation, where sites of a lattice are occupied with an occupation probability p . There is a critical occupation probability p_c that acts much like a critical temperature. At the percolation critical point, for example, the correlation length, or connectedness, diverges. The percolation problem, however, provides us with a model to study the individual droplets, or clusters, of the new phase at the critical point. In the percolation problem, the mean cluster size or the second moment of the cluster size distribution diverges. In addition, the cluster size distribution, itself, scales at the critical point. In the Ising model (see Sec. 1.4.3), cluster identification prescriptions have been formulated which yield these scaling properties.

It is worth noting, many systems, including both models and experimental, exhibit similar values for the scaling exponents described here. These systems are said to be in the same “universality” class. These universality classes can each be described qualitatively by the same free energy functional, although the variables must be redefined for each system. In our research of damage and fracture of materials, we often compare critical exponents to those of magnetic and percolation problems to look for universality.

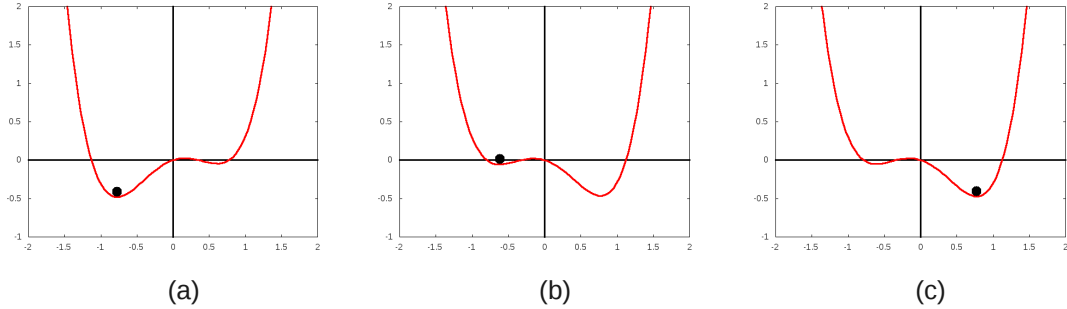


Figure 1.2: This is a depiction of a free energy for an unspecified system. The state of the system is represented by the black dot and in frame (a) is in the globally stable state. Frames (b-e) show a depict the change in shape of the free energy during a slow field reversal. In frame (f) the system a nucleation transition occurs from the metastable state to the lower-energy stable state.

1.2.2 Classical Nucleation Transitions

Discontinuous transitions occur away from the critical point when the system decays from a metastable state to a lower-energy stable state. Note, this lower-energy state could itself be a metastable state. Prior to nucleation, the metastable state has all the properties of a stable state, and thus it is assumed it can be described using equilibrium statistical mechanics. A system can come to reside in a metastable state as a result of either an off-critical quench or a slowly changing external field. Figure 1.2 depicts a nucleation transition in an off-critical quench. This is an abrupt change in the external field at a temperature below the critical value T_c . In Frame (a) the system has a large negative field applied and the system is in the globally stable state with all spins pointing down. In Frame (b) the direction of the external field has flipped. The low energy stable state has now become the higher energy meta-stable state. Thermal fluctuations causes nucleation of the up-spin phase and the system transitions from the meta-stable state to the globally stable (preferred) state in Frame (c).

During a quasi-static sweep of the external field from a positive direction to a negative direction, a plot of the order parameter vs the field will show a discontinuity when the transition occurs. During the phase transition the system passes through a coexistence state, in which both phases of the system occur simultaneously. The coexistence of two phases is associated with a latent heat where energy is either absorbed or released as the phase change occurs but the temperature re-

mains constant. Thermal fluctuations, which intiate the transition, appear as isolated non-interacting droplets or regions of the “new” phase. These droplets have a well-defined boundary and thus a free energy of the interior and surface are also well-defined. Classical nucleation theory states that fluctuations below a specific “critical droplet” size tend to shrink and vanish, while fluctuations larger than the “critical droplet” tend to grow taking the system to its new lower energy state. This can be seen by looking at the free energy of formation of a droplet of the new phase:

$$\epsilon_l = 2hl + \sigma l^{\frac{d-1}{d}} \quad (1.8)$$

where h represents the applied field, l is the size of the droplet and σ is the “surface tension” or simply a material parameter. Again, we assume a spherical compact droplet and a negative h . The first term is due to the bulk of the droplet and tends to lower the free energy of the system as the droplet grows. The second term is from the interaction of the two phases and tends to raise the free energy as the droplet grows. The competition between the bulk and surface term of the free energy of formation determines if a droplet will grow or shrink. If $l > l_c$, the bulk term dominates and the droplet will grow [7]. It is the surface tension of the droplet that inhibits the phase transition. Kinetics of the nucleation transition in the classical approximation was first developed by Becker and Döring, and a field-theoretic formulation of nucleation developed by Langer [8]. Both of which led to an exponential nucleation rate with different proportionality constants:

$$I \propto e^{-\beta \epsilon_{l_c}} \quad (1.9)$$

where ϵ_{l_c} is the free energy of formation of the new phase droplet of critical size l_c and $\beta = 1/k_B T$ [7]. The inverse of the nucleation rate is the lifetime of the metastable state. For shallow quenches past the coexistence curve, ϵ_{l_c} can be quite large making the lifetime exceedingly long. If the system is driven far past the coexistence curve, the lifetime of the meta-stable state is much too short to be described by equilibrium properties. The quench depth for this change in physics is called the Becker-Döring limit and will be discussed below.

1.2.3 Spinodal Decomposition/Continuous Ordering

Spinodal decomposition or continuous ordering describes the process of evolving from an unstable to stable state when the order parameter is conserved or non-conserved respectively. A critical quench from a high temperature ($> T_c$) to a low temperature ($< T_c$) in the magnetic system, for example, can produce an unstable state. As the order parameter is not conserved, this is

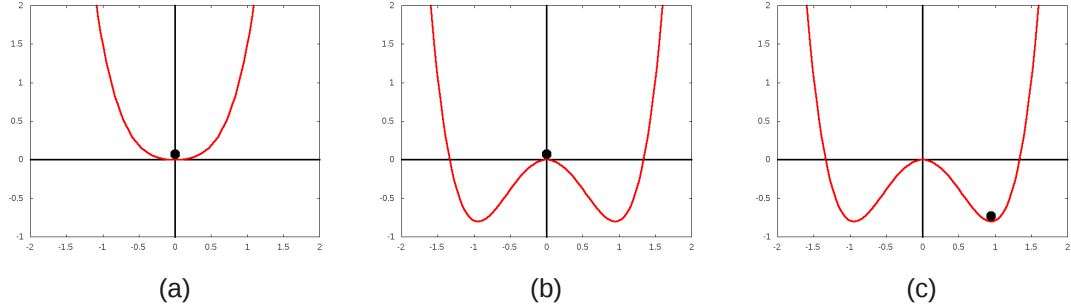


Figure 1.3: This is an example of a critical quench in the free energy picture. In frame (a) the system is above the critical temperature and in the only available state. In frame (b) a sudden quench to a temperature below the critical value occurs and the system is now in an unstable state. Due to fluctuations the system evolves to one of the two lower-energy stable states in frame (c).

an example of a continuous ordering transition. The early time kinetics of spinodal decomposition and continuous ordering are described by the Cahn-Hilliard-Cook (CHC) theory [9, 10, 11]. This linear theory predicts an exponential growth of Fourier modes immediately following the quench to the unstable state. The duration of this exponential growth is proportional to the logarithm of the interaction range. Long-range interaction tend to suppress the noise in the system, thus making fluctuations smaller and the evolution of the system from the metastable state take longer. It should be noted, the CHC theory does not pertain to off-critical quenches where the order parameter is not conserved. The CHC theory was extended to include this situation and to described symmetry breaking transitions by Dominguez et al. [12]. This will be discussed further in Chapter 5.

1.2.4 Nucleation Near the Spinodal

Classical nucleation theory, introduced earlier, can accurately describe systems undergoing shallow quenches with non-interacting compact droplets initiating the phase transition. A shallow quench puts the system in a metastable state near the coexistence curve. If a quench takes the system to a metastable state far from the coexistence curve, the free energy cost of a critical droplet becomes small, of the order kT or the energy of thermal fluctuations. In this case the lifetime of the metastable state becomes increasingly short, and the assumption that the metastable state acts as an equilibrium state is violated. This quench depth, limit of metastability, or cloud point is

called the Becker-Döring limit and for many systems is not the spinodal. It is often the case when systems that nucleate at the cloud point, they do not show scaling or divergence of the susceptibility. As will be discussed shortly, the spinodal acts much like a critical point, and thus will have scaling behaviors for the response functions.

As the range of interaction is increased, the Becker-Döring limit is pushed closer to the spinodal. In practice, a system can never actually reach the spinodal due to fluctuations causing nucleation. The strength of fluctuations decreases as the the range of interaction increases and thus nucleation in the proximity of the spinodal can only occur in long-range systems. The spinodal is a line in phase space that terminates at the critical point and many of the properties of the critical point are observed near at the spinodal line. In the proximity of the spinodal, for long-range interactions, the nucleating droplet is actually a critical fluctuation. This critical fluctuation or “droplet” has a diffuse structure and growth of the “new” phase occurs by a filling-in effect rather than by growth of a compact structure by addition of monomers at the surface. In addition the density of the critical droplet vanishes at the spinodal with the same critical exponent as the order parameter. It must be stressed that nucleation near the spinodal occurs only for systems with long-range interactions that have undergone a deep quench.

Since the spinodal is in fact a critical point, as evident by the phase change initiating by critical fluctuations, the response functions display scaling behaviors. The spinodal is defined by both a spinodal temperature, T_s and a spinodal field h_s , where T_s is below the critical temperature and h_s is dependent on the temperature. For this reason all scaling relations can be expressed in terms of either the proximity to T_s for fixed h_s or vis a versa. The common choice for the scaling field will be $\Delta h = h - h_s$. A theoretical description of spinodal nucleation by Unger and Klein [13, 14], reformulated the work done by Langer [8]. Here it was found the susceptibility and correlation length scale as:

$$\chi_T \approx (\Delta h)^{-\gamma} \quad (1.10)$$

$$\xi \approx (\Delta h)^\nu \quad (1.11)$$

In the same manor as the critical point transition, a frequency-magnitude plot of the size of fluctuations will display a power-law distribution with scaling exponent, τ . A nucleation rate for spinodal nucleation can be expressed as:

$$I \propto e^{-C\beta\Delta F} \quad (1.12)$$

where the ΔF is the free energy cost of a critical fluctuation of the size of the correlation length

given by

$$\Delta F = R^d (\Delta h)^{\frac{3}{2} - \frac{d}{2}} \quad (1.13)$$

As shown here, nucleation near the spinodal has many characteristics that are common to both 1st and 2nd order phase transitions. The nucleation rate has the same functional dependence on the free energy cost of forming the new phase droplet and the scaling properties are the same form as those at the critical point. Spinodal nucleation, however, is a mechanism only for phase transitions in systems with long-range interactions in the edge of the existence of the metastable state. Linear elastic mechanics has demonstrated that long-range elastic interactions are indeed in effect in fracture and formation of cracks. In addition, a deep quench, or spinodal field h_s , is much like a static threshold seen in many friction and failure experiments and models. For these reasons, we investigate nucleation near the spinodal critical point as well as classical nucleation and critical point phenomenon as an explanation of the phenomenon observed in fracture experiments and earthquakes.

1.3 Evidence of Phase Transitions in Fracture

1.3.1 Experimental Data

In addition to knowledge gained from earthquakes, much of the understanding of geologic material failure has come through laboratory experiments [2, 15, 16, 17]. Often experimental friction and fracture data produces scaling laws commonly associated with phase transitions. One such experiment detects acoustic emissions associated with micro-cracks (damage) appearing in the material prior to rupture [2]. The experiment applies a differential pressure, P , to the top and bottom surfaces of a circular chip-board panel. The specimen is held in a confined chamber with four microphones equally spaced around the perimeter of the sample. The microphones record the time and magnitude of acoustic emissions produced by the emergence of micro-fractures. The location of these micro-fractures within the sample is determined from the time delay of the signal to multiple detectors. This experiment was conducted at multiple loading pressures and the results show scaling behavior in both the size-distribution of the micro-cracks and the inter-event time intervals. These scaling behaviors, shown in Fig. 1.4, are indicative of critical phenomena. This figure is reproduced from Guarino et al. [2, Fig. 9]. Fig. 1.4 (a) shows the frequency of inter-event waiting times δt for all micro-fractures during a single run at loading pressure $P = 0.56$ atm. Fig. 1.4 (b) shows, for the same experiment, the distribution of energy-release per micro-fracture leading up to the catastrophic

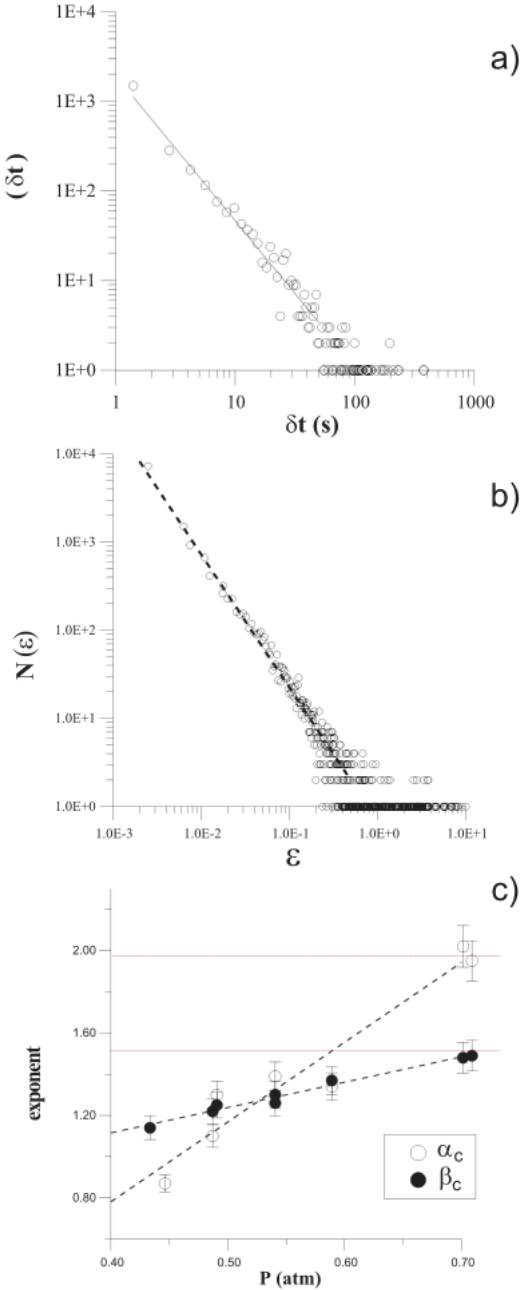


Figure 1.4: (a,b) Two typical time δt and energy ε distributions obtained at imposed constant pressure ($P = 0.56$ atm). (c) The exponents α_c (empty circles) and β_c (black points), plotted as a function of the value of the imposed constant pressure. Note that as the pressure increases, the values of the exponents tend to those obtained in the case of constant pressure rate. The error bars represent the statistical uncertainty. (Image reproduced with kind permission of The European Physical Journal and Guarino et al. [2])

failure of the sample. And last, in Fig. 1.4 (c), the variation of the scaling exponent with the applied load is shown.

In addition to the scaling behavior shown here, experiments such as these have shown initial micro-fracturing occurs randomly throughout the sample but tend to coalesce at the nucleation site of the final macroscopic rupture. This and other evidence of scaling in material failure experiments is strong evidence for the use of statistical physics of phase transitions, which inherently involve scaling and critical point behaviors, as a key factor in understanding the fracture process.

In regard to geological fracturing (earthquakes and faulting), there is another important physical process that is not well understood. This is the concept of material healing or re-strengthening. Healing has been proposed based on both observations of recurring failures along the same fault [18] and in sliding friction experiments in the laboratory [17]. In the laboratory, slide-hold-slide experiments were performed on various rock materials. The strength of the static friction force required to overcome for slip to occur was recorded as a function of the hold-times. It was found for the tested materials the static frictional force increased as $\log(t)$ after a slip event, where t is the time since the last slip occurred. These results suggest a healing process takes places between the sliding surfaces following a shear failure or displacement.

1.3.2 Earthquakes

Earthquakes are often categorized statistically with two primary scaling laws. These are the Gutenberg-Richter distribution for frequency of event magnitudes [3] and Omori's law for the rate of the frequency of aftershocks occurring after a mainshock [4]. A representative example of a Gutenberg-Richter distribution is shown in Fig. 1.5, originally published by [19] and reproduced here.

This plot shows the cumulative number of events of size greater than magnitude m as a function of m . The magnitude here is given by the logarithm of the moment M and thus this figure shows a scaling-law between the moment and cumulative number where the slope is the scaling exponent. The Gutenberg-Richter law for earthquake moments can be written as:

$$N(> M) \propto M^{-b} \quad (1.14)$$

where N is the number of events with moment greater than M .

This frequency-size distribution is a scaling law similar to that seen in the fracture experiment described above [2]. A difference being, this Gutenberg-Richter law is presented as a

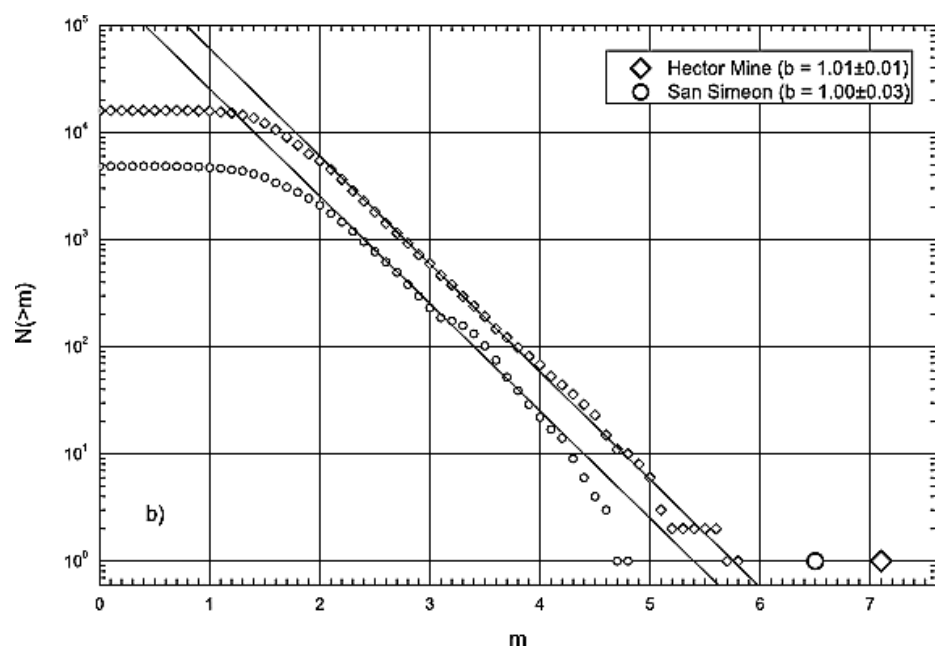


Figure 1.5: This is a Gutenberg-Richter distribution for event magnitudes following two mainshock events. The mainshocks are shown in this figure with the oversized dots above magnitude 6. (Image reproduced with kind permission of Geophysical Research Letters and Shcherbakov et al. [19])

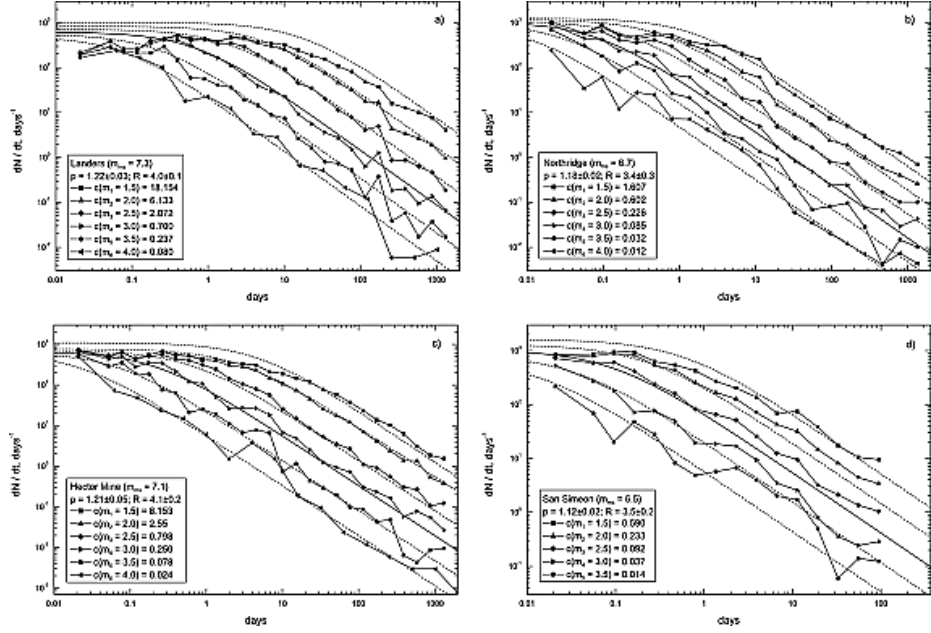


Figure 1.6: This is an Omori's law plot for four different earthquakes in California. (Image reproduced with kind permission of Geophysical Research Letters and Shcherbakov et al. [19])

cumulative distribution (CDF), where the data from Guarino et al. [2] is presented as a probability distribution (PDF). A method of transforming a CDF into a PDF is taking a simple derivative with respect to the dependent variable. This lowers the scaling exponent by 1. A reverse transformation is done by integration. Therefore, a PDF for the frequency-size distribution of earthquakes would show a scaling exponent of $b' = 2$. This is slightly larger than the scaling exponents for the frequency-magnitude distribution of microfractures in the chipboard experiment shown above.

The second scaling law commonly referred to in reference to earthquakes and their aftershocks is Omori's law [4]. This law states the rate of earthquake occurrence following a mainshock decays in time. Omori's law can be written:

$$n(t) = \frac{K}{(c + t)^p} \quad (1.15)$$

where K , c and p are fitting parameters. The scaling exponent p tends to be near $p \approx 1$. Figure 1.6 shows Omori's law plots for 4 earthquakes in California. This plot has also been reproduced from [19]. Each plot in Figure 1.6 has multiple fits based on lower magnitude cutoff. In each case there is clear evidence for decaying power-law with time. Although this behavior is seen after nearly all earthquakes, the physical origin of this scaling relationship is still a topic of debate.

1.4 Numerical Models

Numerical models are essential to test physical ideas and concepts that correspond to laboratory and field observations. Using simulations is also a method of connecting physics in the large and small scales. Within simulations the scale of the problem is easily adjusted and thus comparison of fracture results across several length scales is readily available. Simulations also allow many many realizations of fracture experiments and produce large data sets for statistical analysis. In addition, simulations can be as sophisticated or rudimentary as needed. This allows the ease of testing a very specific situation, with extremely detailed physical parameters or simulating a “toy-model” of fracture with simple physical ideas regarding the rupture process.

Models of material damage often incorporate both failure thresholds and long-range load sharing. The thresholds can be placed on either the stress or the strain of elements in the system. In addition, the thresholds can be time-dependent. The strength of interactions for long-range load sharing can be either constant or decaying with distance. A linear elastic system, for example, will have interactions that decay as $1/r^3$ for a 2D displacement [20]. Aspects of scaling and critical phenomena are often studied using these models [21, 22], as well as nucleation near the spinodal [23] in addition to numerous other physical concepts. As noted earlier, a primary focus of simulations has been placed upon understanding the origins of the frequency-size relationship for event magnitudes in earthquake systems [22, 24] and Omori’s law for aftershocks [25]. Two models of material failure often used to describe earthquakes are the slider-block model, originally proposed by Burridge and Knopoff [26], for shear failure and sliding friction, and the fiber-bundle model [27] for failure under tensile loads. These models involve a system with a large number N of brittle elements with a prescribed distribution of failure strengths. An external force is applied to the system as either a static or time-dependent load. These models often display various failure modes depending on the distribution of strengths and loading conditions. Another model commonly adapted to describe various problems in physics is the Ising model, originally proposed to describe ferromagnetism [5, 6]. Although this model does not immediately lend itself to studying fracture and failure of materials, a change of variables and restructuring of the Hamiltonian (or free energy functional) allows this model to adequately represent failure mechanisms. Below is a brief description of these three models which are used in this research.

1.4.1 Fiber-bundle Model

The fiber-bundle model is a simple representation of tensile failure of composite materials. The model consists of an array of elements that are each given a failure strength drawn from a prescribed distribution. This failure strength can be imposed as either a maximum stress or a maximum strain. A load is then applied uniformly to the array of elements. Typically linear-elastic behavior of the fibers is assumed. If a stress threshold is prescribed, the load is increased until the load matches the strength of the weakest element. This fiber or element then breaks and the stress on it is redistributed. Redistribution can occur either locally (typically nearest-neighbors only), globally (the load redistributed across the entire array), or across a long but finite interaction region. The failed fiber is now completely removed from the system and the load continues to increase, causing more fibers to break, until the entire array of elements has reached their failure threshold. The coalescence of failed elements often resembles nucleating droplets, and is governed by the failure strength prescription, the loading rate and the range of interaction. There are many versions of this model with theoretical support to explain the rupture process [27, 28, 29, 30]. We have constructed a time-dependent version of this model and published the findings in “Theoretical and Applied Fracture Mechanics” and reproduce the manuscript in Chapter 2 [31].

1.4.2 Slider-block Model

The slider-block model is a “toy model” of an earthquake fault. A diagram of this model with nearest-neighbor coupling springs is given in Fig 1.7. The model is constructed by aligning blocks in an array on a frictional surface. These blocks are then connected to each other with coupling springs of spring constant k_c . Each block is also connected to a loader plate, with springs of spring constant k_p , that pulls the blocks along the frictional surface. The loader plate is assumed to move at relatively slow velocities to allow stick-slip behavior of the individual blocks rather than continuous sliding.

The loader plate provides the driving force for the system. As the loader plate moves forward it increases the stress on the blocks through extension of the loader springs. Eventually, the stress on a certain block overcomes the static friction threshold and this block slips forward obeying simple kinematic equations of motion. The mathematical expression of the frictional force is typically modeled as velocity-weakening, but the exact form of this function is not unanimously agreed upon. And, in fact, changing the form of the friction can lead to changes in the failure modes of the model. As the “slipped” block moves forward it transfers stress to its neighbors

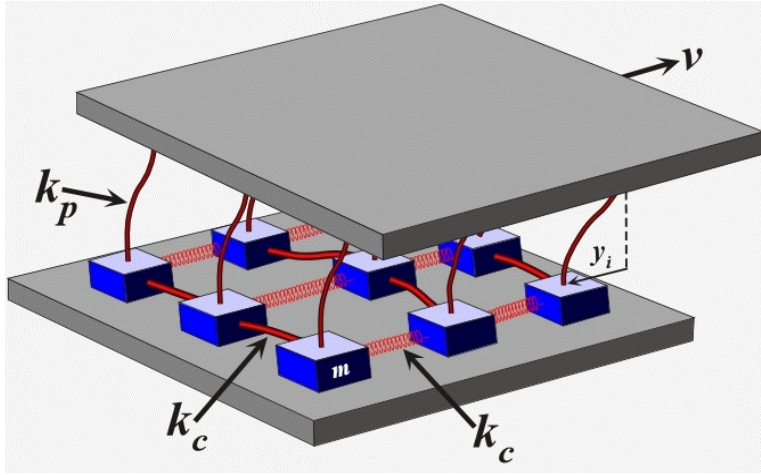


Figure 1.7: This is a diagram of the 2D slider-block model with nearest neighbor interactions. The loader plate is moving at velocity v . (Image courtesy of Dr. John Rundle)

through the coupling springs, potentially causing them to slip as well. All blocks that slip as a consequence of the first slipped block are, together, considered to be a single macroscopic fracture event or earthquake. This process is continued indefinitely, until enough events have been collected to perform statistical analysis.

This model can be simulated using either molecular dynamics (MD) or cellular-automata (CA) update routines. While MD simulations solve specific differential equations that represent the dynamics of the model, they can become labor intensive as the system size grows large. On the other hand, CA models employ simple update rules that can be easily programmed and run considerably faster than MD versions. Also, it has been shown that in the limit of small velocities and long-range interactions, the results of the two routines approach one another [32]. In the research presented here, we use the CA version of the slider-block model. We use this model as the basis for testing two new physical ideas. Namely, failure stress threshold weakening due to insufficient time for healing to occur and stress fatigue which causes failures below the static threshold. In Chapter 3 we reproduce a manuscript describing the threshold weakening model originally published in “Physica A” [33]. Chapter 4 is a manuscript describing the stress fatigue model, submitted to “Geophysical Journal International” and is currently in the peer-review process.

1.4.3 Ising Model

The last model we introduce is the Ising model [5, 6]. This model was originally proposed to describe the paramagnetic to ferromagnetic phase transition described briefly in Section 1.2. This is a coarse grained lattice model in which a magnetic dipole or “spin” is placed at each node of the lattice. These spins can occupy one of two states, up or down. Generalizations of this model, the XY and Heisenberg models, involve allowing spins to assume any position in a plane or solid angle respectively. The order parameter for the Ising model, the average magnetization per site m , is defined as the number of spins pointing up minus the number of spins pointing down divided by the total number of spins N :

$$m = \frac{N_{\uparrow} - N_{\downarrow}}{N} \quad (1.16)$$

Each spin interacts with its neighbors through an interaction potential and with an applied magnetic field. A Hamiltonian for this system can be written as follows:

$$H = -J \sum_{\langle ij \rangle} s_i s_j - h \sum_i s_i \quad (1.17)$$

Here the first summation is over neighboring (interacting) pairs while the second sum is over all sites in the lattice. J is the interaction coupling constant, h is the applied magnetic field and $s = \pm 1$ which represents the state of the spins. In the absence of an applied magnetic field, the magnetization can take either a positive or negative value when the system passes through the critical point. If h takes a nonzero value the system will always have a well-defined globally stable state.

In a critical quench, from $T > T_c$ to $T < T_c$, it is common to measure the correlation time and length of the model. The correlation time can be measured by constructing an autocorrelation function defined as:

$$X(t) = \int dt' [m(t') - \langle m \rangle] [m(t + t') - \langle m \rangle] \quad (1.18)$$

The autocorrelation is expected to fall off as $X(t) \sim \exp(-t/\tau)$ where τ is the correlation time of the system. This is the expected time(iterations) you have to wait for the system to be in a state that is completely independent of the initial state.

The correlation length can be measured using a correlation function. One way to obtain the correlation function is to first calculate the structure factor and simply compute the Fourier transform to invert it. The structure factor is defined as:

$$S(\mathbf{k}) = \frac{1}{N} \langle |\tilde{s}'(\mathbf{k})|^2 \rangle \quad (1.19)$$

where $\tilde{s}'(\mathbf{k})$ is the Fourier transform of $s'_i = s_i - m$. An estimate of the correlation length is the distance at which the correlation function crosses the x-axis. This is distance away at which no spatial correlations exist. As the temperature approaches the critical temperature the correlation length diverges and likely will become larger than the lattice size of the simulation.

The Ising model also allows nucleation transitions from a metastable state to stable state. A metastable state can be prepared by applying a positive external field at high temperature and quenching the system to below the critical point. This will force the system into a globally stable state with all the spins aligned in the upward direction. An instantaneous flip (or quench) of the magnetic field, will now have the system residing in a metastable state (all up spins) with a preferred stable state (all spins pointed down) at a lower free energy. The transition process will occur via nucleation. This is identical to the nucleation transition described in Fig. 1.2. For deep quenches and long-range interactions, this model will display properties of spinodal nucleation.

This model is extremely versatile and is easily adapted to various problems outside the realm of magnetism. In our research we have redefined the parameters of this model and restructured the Hamiltonian to represent the physics of fracture. Namely, we have assigned each cell a continuous crack opening parameter, or “offset”, rather than a binary “spin” state. This offset is positive definite and can assume any value. The field term of the Hamiltonian now represents the applied force or stress and the interaction term is due to elastic interactions within the material. In addition we have added a contribution to the energy due to the cohesion of the two crack surfaces. Aside, from these changes the model is essentially identical to the Ising model. We use the standard Metropolis Monte Carlo dynamics to compute the evolution of the model within the simulations. This is a standard process performed in the Ising model. A manuscript describing our model and its behavior has been submitted to Physical Review E, and reproduced here in Chapter 5.

1.5 Implementation

The bulk of the numerical work has been programmed using C++. This language was chosen both for its object-oriented structure as well as the speed in which it handles numerical calculations. A single model would typically contain on the order of 1000 lines of code. The compiled programs would include multiple user option flags to incorporate various loading schemes as well as several damage and defect prescriptions. The processing of data for statistical analysis was handled using either C++, Python or Bash scripting. In most cases, data files were created and plotting was handled using Gnuplot. For the sake of presentations, topological movies of the rupture

front propagating through the lattice were created using Python. Simulations were run on an Intel Core 2 Quad desktop computer within a Linux environment.

1.6 References

- [1] A. Guarino, A. Garcimartin, M. Zei, and R. Scorratti. An experimental test of the critical behavior of fracture precursors. *Eur. Phys. J. B*, 6:13–24, 1998.
- [2] A. Guarino, S. Ciliberto, A. Garcimartin, M. Zei, and R. Scorratti. Failure time and critical behavior of fracture precursors in heterogeneous materials. *Eur. Phys. J. B*, 26:141–151, 2002.
- [3] B. Gutenberg and C. F. Richter. *Seismicity of the Earth and Associated Phenomena*. Princeton University Press, Princeton, NJ, 1954.
- [4] T. Utsu. A statistical study on the occurrence of aftershocks. *Geophys. Mag.*, 30:521–605, 1961.
- [5] Shang-Keng Ma. *Modern Theory of Critical Phenomena*. Addison-Wesley, Reading, MA, 1976.
- [6] N. Goldenfeld. *Lectures on Phase Transitions and the Renormalization Group*. Addison-Wesley, Reading, MA, 1992.
- [7] J. D. Gunton and M. Droz. *Introduction to the Theory of Metastable and Unstable States*. Number 183 in Lecture Notes in Physics. Springer-Verlag, Berlin Heidelberg, 1983.
- [8] J.S Langer. Theory of the condensation point. *Annals of Physics*, 41(1):108 – 157, 1967.
- [9] J. W. Cahn and J. E. Hilliard. Free energy of a nonuniform system. i. interfacial free energy. *J. Chem. Phys.*, 28:258–267, 1958.
- [10] J. W. Cahn and J. E. Hilliard. Free energy of a nonuniform system. iii. nucleation in a two-component incompressible fluid. *J. Chem. Phys.*, 31:688–699, 1959.
- [11] H. E. Cook. Brownian motion in spinodal decomposition. *Acta Metall.*, 18:297–306, 1970.
- [12] R. Dominguez, K. Barros, and W. Klein. Early time kinetics of systems with spatial symmetry breaking. *Phys. Rev. E*, 79:041121, 2009.

- [13] C. Unger and W. Klein. Nucleation theory near the classical spinodal. *Phys. Rev. B*, 29: 2698–2708, 1984.
- [14] C. Unger and W. Klein. Initial growth modes of nucleation droplets. *Phys. Rev. B*, 31:6127–6130, 1985.
- [15] J. Weeks, D. Lockner, and J. Byerlee. Change in b-values during movement on cut surfaces in granite. *Bull. Seismol. Soc. Am.*, 68(2):333–341, 1978.
- [16] C. Marone. Laboratory-derived friction laws and their application to seismic faulting. *Annu. Te. Earth Planet. Sci.*, 26:643–696, 1998.
- [17] J.H. Dieterich. Time-dependent friction in rocks. *J. Geophys. Res.*, 77:3690–3696, 1972.
- [18] C. Marone, J. E. Vidale, and W. L. Ellsworth. Fault healing inferred from time dependent variations in source properties of repeating earthquakes. *Geophys. Res. Lett.*, 22(22):3095–3098, 1995.
- [19] R. Shcherbakov, D. L. Turcotte, and J. B. Rundle. A generalized Omori’s law for earthquake aftershock decay. *Geophys. Res. Lett.*, 31(L11613), 2004. doi: 10.1029/2004GL019808.
- [20] J. A. Steketee. On volterra’s dislocations in a semi-infinite elastic medium. *Can. J. Phys.*, 36: 192–205, 1958.
- [21] J. M. Carlson and J. S. Langer. Properties of earthquakes generated by fault dynamics. *Phys. Rev. Lett.*, 62:2632–2635, 1989.
- [22] J. B. Rundle and W. Klein. Nonclassical nucleation and growth of cohesive tensile cracks. *Phys. Rev. Lett.*, 63:171–174, 1989.
- [23] W. Klein, M. Anghel, C. D. Ferguson, J. B. Rundle, and J. S. Sa Martins. Statistical analysis of a model for earthquake faults with long-range stress transfer. In J. B. Rundle, D. L. Turcotte, and W. Klein, editors, *Geocomplexity and the Physics of Earthquakes*, Geophysical Monograph 120, pages 43–71. American Geophysical Union, Washington D.C., 2000.
- [24] W. Klein, J. B. Rundle, and C. D. Ferguson. Scaling and nucleation in models of earthquake faults. *Phys. Rev. Lett.*, 78:3793–3796, 1997.
- [25] J. Dieterich. Earthquake simulations with time-dependent nucleation and long-range interactions. *Nonlinear Proc. Geoph.*, 2:109–120, 1995.

- [26] R. Burridge and L. Knopoff. Model and theoretical seismicity. *Bull. Seismol. Soc. Am.*, 57: 341–371, 1967.
- [27] W. I. Newman and S. L. Phoenix. Time-dependent fiber bundles with local load sharing. *Phys. Rev. E*, 63:021507, 2001.
- [28] H. E. Daniels. The statistical theory of the strength of bundles of threads. I. *Proc. Roy. Soc. Lond. A*, 183:405–435, 1945. doi: 10.1098/rspa.1945.0011.
- [29] F. Kun, S. Zapperi, and H. J. Herrmann. Damage in fiber bundle models. *Eur. Phys. J. B*, 17 (2):269–279, 2000.
- [30] S. L. Phoenix and W. I. Newman. Time-dependent fiber bundles with local load sharing. II. General Weibull fibers. *Phys. Rev. E*, 80:066115, 2009.
- [31] G. Yakovlev, J. D. Gran, D. L. Turcotte, J. B. Rundle, J. R. Holliday, and W. Klein. A damage-mechanics model for fracture nucleation and propagation. *Theoretical and Applied Fracture Mechanics*, 53:180–184, 2010.
- [32] Junchao Xia, Harvey Gould, W. Klein, and J. B. Rundle. Near-mean-field behavior in the generalized burridge-knopoff earthquake model with variable-range stress transfer. *Phys. Rev. E*, 77(3):031132, 2008.
- [33] J. D. Gran, J. B. Rundle, D. L. Turcotte, J. R. Holliday, and W. Klein. A damage model based on failure threshold weakening. *Physica A*, 390:1269–1278, 2011.

Chapter 2

A damage-mechanics model for fracture nucleation and propagation

Abstract

In this paper a composite model for earthquake rupture initiation and propagation is proposed. The model includes aspects of damage mechanics, fiber-bundle models, and slider-block models. An array of elements is introduced in analogy to the fibers of a fiber bundle. Time to failure for each element is specified from a Poisson distribution. The hazard rate is assumed to have a power-law dependence on stress. When an element fails it is removed, the stress on a failed element is redistributed uniformly to a specified number of neighboring elements in a given range of interaction. Damage is defined to be the fraction of elements that have failed. Time to failure and modes of rupture propagation are determined as a function of the hazard-rate exponent and the range of interaction.

2.1 Introduction

A composite model is introduced in this paper for the nucleation and propagation of fractures. The model incorporates aspects of damage mechanics, fiber-bundle models, and slider-block models. A square array of elements is considered, these elements are analogous to the fibers in a fiber-bundle model and the blocks in a slider-block model. At time $t=0$ a constant force is applied to the system. Time-to-failure statistics are prescribed. When an element fails the stress on that element is transferred to a prescribed range of adjacent elements. Numerical simulations are used to

study the conditions under which a well defined rupture nucleates and to illustrate the propagation of this fracture over the array. The model is closely related to the fiber-bundle model. The fiber bundle initially consists of n_0 fibers. Subsequently n_f fibers fail and when $n_f = n_0$ the bundle fails. When a fiber fails the load on that fiber is transferred to other fibers. In the equal load sharing case the load is transferred to all other fibers equally. In the local load sharing case the load is transferred to the adjacent fibers within a prescribed interaction region. Two failure criteria have been proposed. The first is static and a failure strength is prescribed statistically for each fiber [1]. As the stress on the fibers increase, more fibers fail. The second failure criterion specifies a statistical time to failure for each fiber that is stress dependent [2, 3]. In terms of applicability the latter approach is now generally accepted. A general review of fiber-bundle models has been given in [4].

Damage mechanics is an empirical continuum approach to material failure [5, 6]. A continuum damage variable α is defined by the relation

$$E = E_0(1 - \alpha) \quad (2.1)$$

where E is the Young's modulus for the damaged material and E_0 is the Young's modulus for the undamaged material. When $\alpha = 1$ failure occurs. A rate equation for the increase in damage is specified. There is a close association between the equal-load sharing fiber-bundle model and damage mechanics if it is assumed that [7]

$$\alpha = \frac{n_f}{n_0} \quad (2.2)$$

Damage mechanics does not consider the propagation of a rupture.

Slider-block models have been studied extensively as models for earthquakes [8, 9, 10, 11, 12]. An array of slider blocks is pulled along a surface with puller springs. When the stress on a block exceeds the static coefficient of friction it slips and stress is transferred to other blocks by connector springs. Extensive studies of the role of stress transfer have been carried out [13]. When a block fails the stress on the block is redistributed equally to neighboring blocks in a given range of interaction. This approach has been used to study a slider-block model in a failure mode [14]. However, no time to failure statistics were incorporated.

2.2 The Model

An illustration of the model is given in Fig. 2.1. A square grid of elements is considered with L elements on a side, for the case illustrated $L = 17$ so that the total number of elements

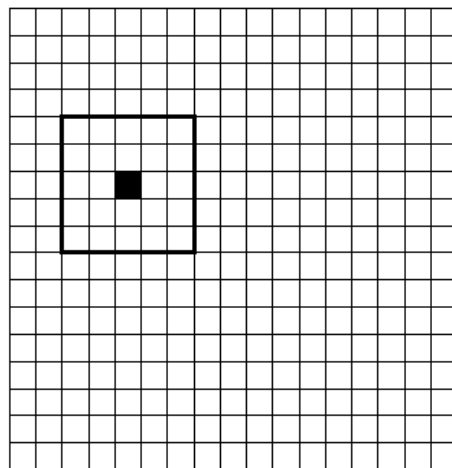


Figure 2.1: Illustration of the model. A square grid of elements with width L is considered, in this case $L = 17$ so that there are $n_0 = 17^2 = 289$ elements. At time $t = 0$ a uniform load F_0 is uniformly distributed to all the elements. The stress σ_0 on each element is $\sigma_0 = F_0/n_0$. One element has the shortest time to failure $t_{f,\min}$, the failure of this element is the solid square. The stress from this failed element is redistributed equally to all the elements within range r . Here $r = 2$ and is represented by the black line surrounding the failed element. The stress is redistributed equally to the 24 remaining elements within the square.

is $n_0 = 17^2 = 289$. At time $t = 0$ a constant load F_0 is applied to the grid and it is uniformly distributed so that each element has a stress

$$\sigma_0 = \frac{F_0}{n_0} \quad (2.3)$$

No additional external forces are applied to the system. A time to failure t_f is assigned randomly to each element from a prescribed distribution. In this paper it is assumed that this distribution is Poisson so that there is no memory of the stress history of an element. The cumulative history of failure times is thus given by

$$P_c(t_f) = 1 - e^{-\nu t_f} \quad (2.4)$$

where ν is the hazard rate. This distribution has been shown to be applicable to the distribution of nucleation times in solid-state physics, specifically the Ising model [15]. A second assumption is that the hazard rate $\nu(\sigma)$ has a power-law dependence on the stress σ on the element

$$\nu(\sigma) = \nu_0 \left(\frac{\sigma}{\sigma_0} \right)^\rho \quad (2.5)$$

where the power-law exponent ρ must be specified and ν_0 is the value of the hazard rate when $\sigma = \sigma_0$. It is found experimentally that values of ρ are in the range 2 – 5 for various fibrous materials [16].

Initially, at $t = 0$, the stresses on all elements are equal with the value σ_0 given in Eq. (2.3). For each element a random number P_c in the range 0 to 1 is chosen. Using this random number the corresponding failure time of the element is obtained from Eq. (2.4) with $\nu = \nu_0$

$$t_f = \frac{1}{\nu_0} \ln[(1 - P_c)^{-1}] \quad (2.6)$$

The first element fails at $t = t_{f,min}$ the smallest of these failure times. This first failed element is illustrated in Fig. 2.1. The failed element is removed from the grid (there is no healing). The stress on the failed element is redistributed equally to all surviving elements in a range of interaction r . For the example illustrated in Fig. 2.1, the range of interaction is $r = 2$. The redistribution is carried out over a square region with $2r + 1$ elements on a side. The maximum number of elements n_{rd} over which the stress is redistributed is

$$n_{rd} = (2r + 1)^2 - 1 \quad (2.7)$$

For the example in Fig. 2.1, $n_{rd} = 24$. In subsequent redistributions some of the elements in the region may have been removed due to previous failures. In this case the stress is redistributed

equally to the surviving elements. If the failed element has no surviving neighbors, the stress on that element is dissipated from the system, reducing the total load.

All surviving elements in the grid are given a new time to failure Δt_f that is determined from Eqs. (2.4) and (2.5) written in the form

$$\Delta t_f = \frac{1}{\nu_0} \left(\frac{\sigma_0}{\sigma} \right)^\rho \ln[(1 - P_c)^{-1}] \quad (2.8)$$

where P_c is a new random number in the range 0 to 1. This approach is appropriate for the Poisson distribution of failures given by Eq. (2.4) since a surviving element has no memory of the prior stress history. Considering the values Δt_f for all elements, the shortest time to failure is determined. At this time this failed element is removed from the grid. This process is continued until all elements have failed. This is the failure time t_{gf} for the grid. At this time the number of failed elements n_f is equal to the number of elements originally on the grid n_0 , $n_f = n_0$. Following the standard association of damage mechanics with the fiber-bundle model we take the damage variable α to be given by Eq (2.2). The damage variable is the fraction of failed elements, failure of the grid occurs at $\alpha = 1$. A primary object of our simulations is to determine α as a function of t ($0 \leq t \leq t_{gf}$).

2.3 Mean Field Analysis

The case in which the stress on a failed element is redistributed equally to the surviving elements on the grid can be solved analytically. This is known as equal-load sharing and is the mean-field limit for this problem. For this case the stresses on all surviving blocks $\sigma_{mf}(t)$ are equal. The condition that the total force F_0 on the grid remains constant for $t > 0$ requires

$$(n_0 - n_f)\sigma_{mf} = n_0\sigma_0 \quad (2.9)$$

The standard breakdown rule for the rate of failure of fibers given in [2, 3, 4] is

$$\frac{d(n_0 - n_f)}{dt} = -\nu(\sigma)(n_0 - n_f) \quad (2.10)$$

where ν is again the hazard rate. If ν is a constant ν_0 the integration of Eq. (2.10) gives the probability distribution given in Eq. (2.4). It is important to note that there is a correspondence between the fiber-bundle formulation and the damage formulation only if the Poissonian failure condition in Eq. (2.4) is used.

The power-law dependence of the hazard rate on stress as given in Eq.(2.5) is assumed to be valid. Combining Eqs. (2.5) and (2.9) gives

$$\nu(n_f) = \nu_0 \left(1 - \frac{n_f}{n_0}\right)^{-\rho} \quad (2.11)$$

and substitution into Eq. (2.10) gives

$$\frac{d(n_0 - n_f)}{dt} = -\frac{\nu_0 n_0^\rho}{(n_0 - n_f)^{\rho-1}} \quad (2.12)$$

Integrating with $n_f = 0$ at $t = 0$ with the definition of the damage variable α given in Eq. (2.2) we find

$$\alpha = \frac{n_f}{n_0} = 1 - (1 - \nu_0 \rho t)^{\frac{1}{\rho}} \quad (2.13)$$

And grid failure occurs at time

$$t_{gf} = \frac{1}{\nu_0 \rho} \quad (2.14)$$

It should be noted that the results given above are applicable for large values of n_0 [4]. Numerical simulations are well approximated by the above results in the equal load sharing (mean-field) limit. These results demonstrate that the appropriate non-dimensional time for our model is $\nu_0 t$.

In the equal load sharing (mean-field) limit failures are spatially random. There is no spatial localization of failure and thus no initiation and propagation of a fracture. In this limit the model is identical to the site-percolation model [17]. This model also consists of a square grid of elements. Percolating elements n_p are picked at random with the probability $p = n_p/n_0$ a variable. This is also a transient problem with increasing p . When $p = p_c$ when a percolating cluster of elements spans the grid [18]. This is a well documented critical point. However, this critical point is not relevant to the total grid failure at $n_p = n_0$.

2.4 Simulations

In order to illustrate the behavior of this model a sequence of numerical simulations have been carried out. In order to carry out a simulation it is necessary to specify: (1) The size of the grid n_0 , (2) the range of interaction r , and (3) the power-law exponent ρ .

In Fig. 2.2 the nucleation and propagation of fractures is illustrated for several typical examples. The power-law exponent introduced in Eq. (2.8) is assumed to have the value =3. In addition, the array has a width $L = 512$ elements so that the total number of elements is $n_0 = 512^2 = 262,144$. Three examples are given with the ranges of interaction $r = 1, 8$ and 32 . The distributions of failed sites (damage) are illustrated for values of the damage variable (fraction of failed elements) $\alpha = 0.05, 0.15, 0.35, 0.55$ and 0.75 . For the nearest neighbor case, $r = 1$, the fracture has just started to nucleate at $\alpha = 0.05$. It subsequently spreads across the array. Note periodic boundary conditions are assumed so that when the propagating fracture reaches the top

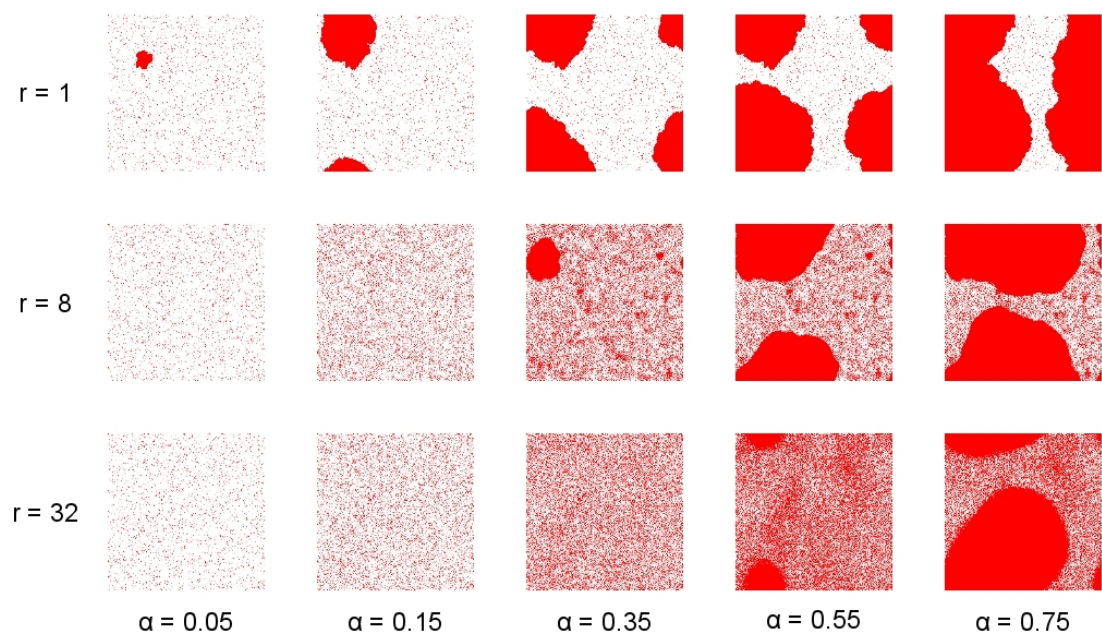


Figure 2.2: Three examples of rupture nucleation and propagation are illustrated. We assume $\rho = 3$, $L = 256$, and consider $r = 1, 8$ and 32 . For each case we give the structure for $\alpha = 0.03, 0.10, 0.30, 0.50$ and 0.70 . The dark areas are failed elements.

boundary of the grid its extension appears at the lower boundary. The propagating fracture is quite irregular and has many indentations. For the intermediate range case $r = 8$ the incipient rupture is delayed until $\alpha = 0.35$. Again the spread of this rupture across the array is clearly illustrated. The rupture in this case is more nearly circular with smoother boundaries. There is also a clearly defined halo of failed elements adjacent to the boundary associated with the $r = 8$ range of stress transfer. For the near mean-field case with $r = 32$ rupture initiation is delayed further and occurs at about $\alpha = 0.55$. The rupture has a diffuse outer boundary as it propagates across the remainder of the array. In the three examples a nucleation phase is followed by a propagation phase. In the mean-field limit $r = 64$ there is no propagation phase. Failed elements are randomly distributed across the grid.

It is also of interest to consider the temporal evolution of the damage variable during rupture nucleation and propagation. Several examples are given in Fig. 2.3. It is important to note that there is considerable variability in each individual simulations. In each case we carry out 500 simulations and the mean times to reach a specified value of the damage variable are obtained. The values of the damage variable α are given as a function of these mean non-dimensional times $\nu_0 t$ after the application of the constant force are given with $L = 129$ and $n_0 = 16,641$ and $\rho = 3$ in Fig. 2.3(a) and $\rho = 6$ in Fig. 2.3(b). Results are given for a sequence of values for the range of interaction from $r = 1$ (nearest neighbor) to $r = 64$ (mean-field). For small values of r the transition from the nucleation phase to the propagation phase is clearly illustrated. For the mean field limit $r=64$ the evolution of the damage variable is in agreement with Eq. (2.13). For $\rho = 3$ the failure takes place at $\nu_0 t_{gf} = 1/3$ and for $\rho = 6$ at $\nu_0 t_{gf} = 1/6$ as predicted by Eq. (2.14). The behavior for the two values of ρ is quite similar except for the reduction in the time to failure for larger ρ as well as a sharper transition from nucleation to propagation.

For all values of the interaction range r for a fixed ρ the initial increase of damage is essentially identical. The transition from rupture nucleation to propagation is governed by the range of interaction. The transition time increases systematically with increasing range of interaction. For a short range of interaction the stress level adjacent to a rupture is greater, increasing the rupture speed and subsequently decreasing the time to failure. When the rupture speed approaches the velocity of shear waves, dynamic affects become important which are not included in this analysis. These effects, however, will not change the times to failure which are dominated by the nucleation phase. The transition from the nucleation phase to the propagation phase is quantified using the

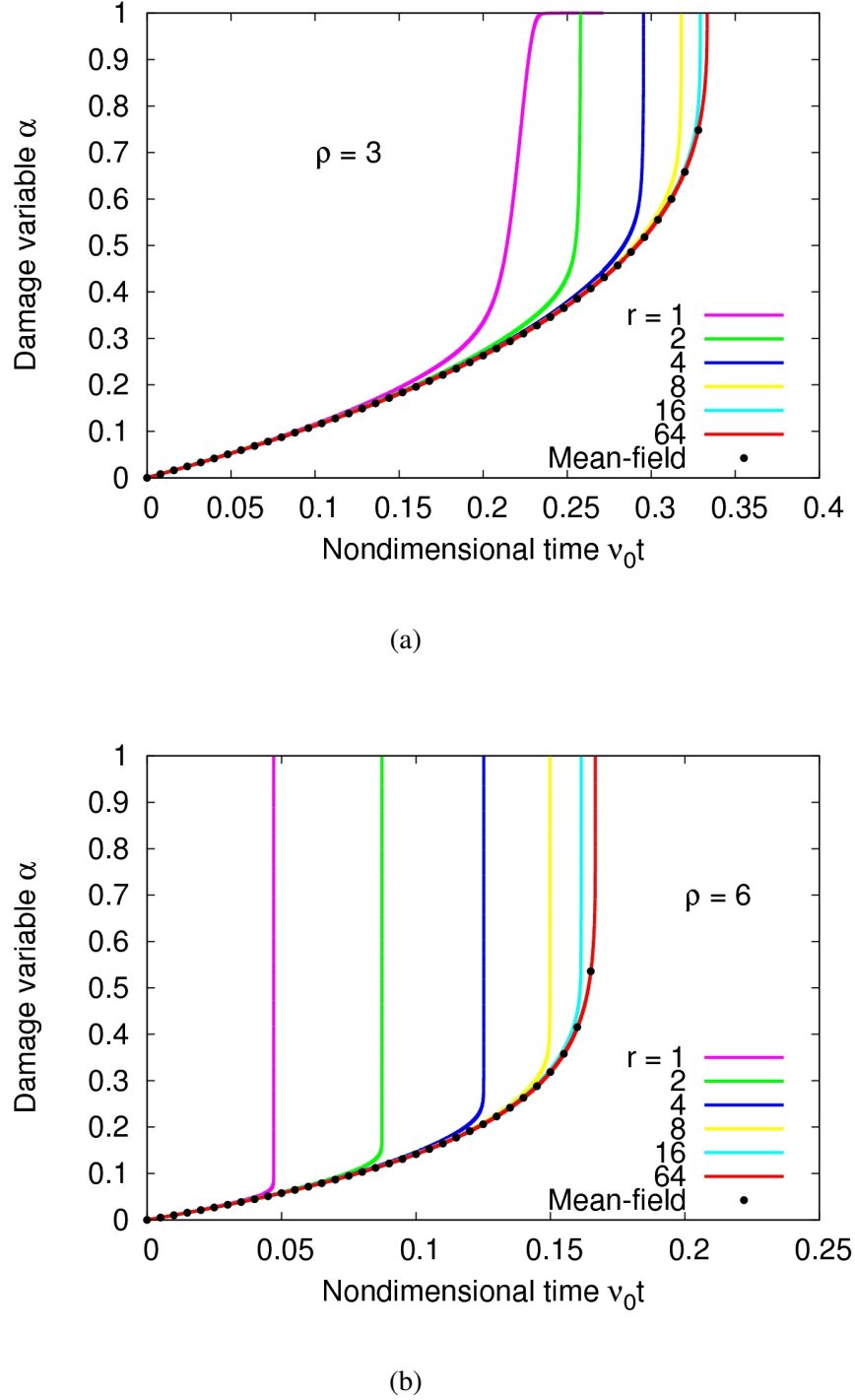


Figure 2.3: Dependence of the damage variable α on the nondimensional time $\nu_0 t$ after the application of the constant applied force. (a) Stress exponent $\rho = 3$. (b) Stress exponent $\rho = 6$. Results are given for ranges of interaction $r = 1, 2, 4, 8, 16, 32$ and 64 (mean field). Also shown is the mean-field solution given in Eq. (2.13).

r	$\rho = 3$	$\rho = 6$
1	0.204	0.047
2	0.252	0.087
4	0.292	0.125
8	0.313	0.149
16	0.327	0.157
32	0.330	0.159

Table 2.1: Non-dimensional times of transition from the nucleation phase to propagation phase are given for several values of the interaction range r and stress exponent ρ . The transition times are computed by locating the point of maximum curvature in the curves plotted in Fig. 2.3(a) and 2.3(b).

maximum curvature of the curves for $\alpha(t)$ plotted in Fig. 2.3. The curvature k is given by

$$k = \frac{\partial \alpha}{\partial t} \quad (2.15)$$

The non-dimensional transition times $\nu_0 t_t$ corresponding to the maximum values of k are given in Table 2.1. For $\rho = 3$ the values decrease systematically for increasing r . For $\rho = 6$ the maximum value is at $r = 2$.

The non-dimensional times to failure $\nu_0 t_{gf}$ is given as a function of the range of interaction r ($r = 1, 2, 4, 8, 16, 32$ and 64 , mean field) in Fig. 2.4. Results are given for the power-law exponent values $\rho = 3, 4, 5 \dots 8$. The failure times decrease with increasing values of ρ as would be expected. As the range of interaction is increased for fixed ρ the failure times asymptotically approach the mean-field limit. For $r = 64$ (mean field) the results are in agreement with the mean-field theory given in Eq. (2.14). Again, each value is the average of 500 simulations.

In Fig. 2.5 the statistical distributions of failure times are given. The cumulative distribution function of failure times P_c is given as a function of the ratio of the non-dimensional failure time to its mean value $t_{gf} = \bar{t}_{gf}$. This dependence is given in Fig. 2.5 for $\rho = 6$ and $r = 1, 2, 4, 8$ and 16 . In the mean field limit ($r = 64$) the standard deviation of the failure times goes to zero. The standard deviation increases systematically with decreasing values of r . It is also of interest to study the dependence of the damage parameter α on the time prior to failure $\nu_0(t_{gf}t)$. This is given in Fig. 2.6 for $\rho = 6$ and several values of r . For $r = 64$ the mean field result given in Eq. (2.13) is found with the power law dependence

$$1 - \alpha = \left(1 - \frac{t}{t_{gf}}\right)^{\frac{1}{3}} \quad (2.16)$$

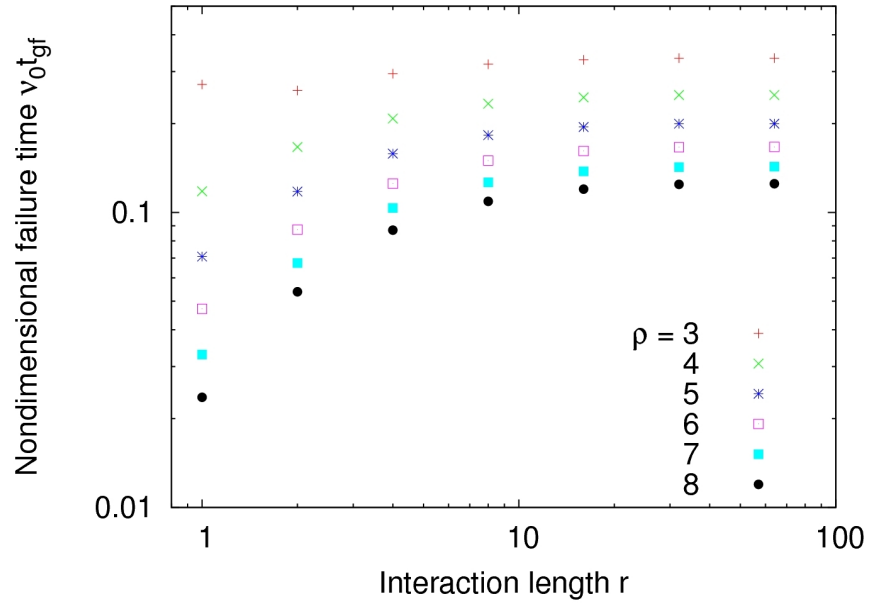


Figure 2.4: Dependence of the nondimensional time to failure $\nu_0 t_{gf}$ on the interaction length r . Results are given for stress exponents $\rho = 1, 2, 3, \dots, 8$.

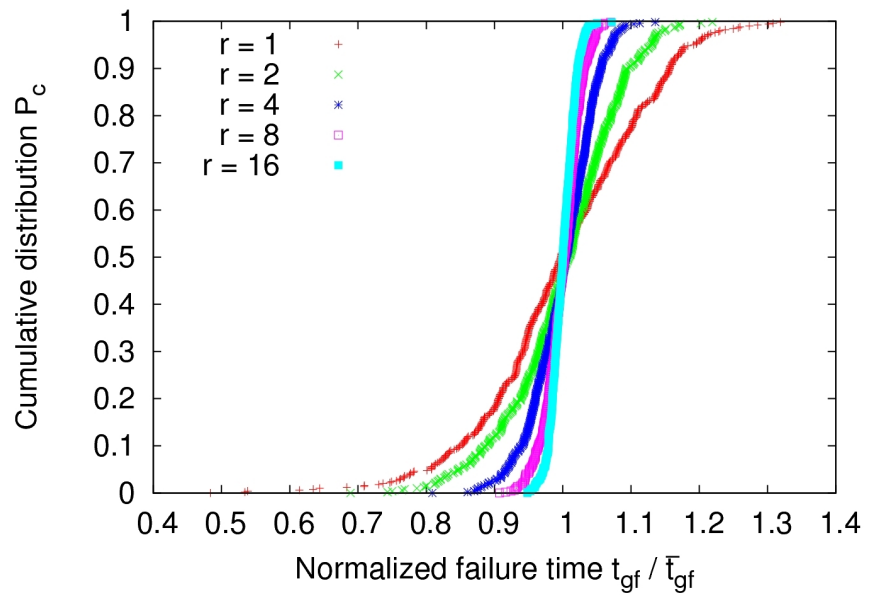


Figure 2.5: Cumulative probability function P_c of failure times t_{gf}/\bar{t}_{gf} for several values of the interaction length r , for $\rho = 6$.

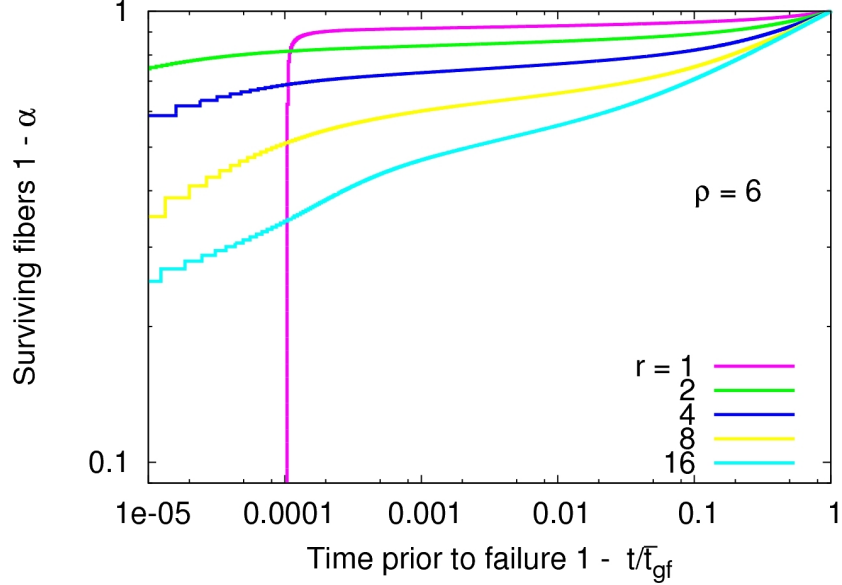


Figure 2.6: Dependence of $1 - \alpha$ on the time prior to failure $1 - t/\bar{t}_{gf}$ for $\rho = 6$ and several values of r .

As r approaches the mean field limit the initial power-law behavior becomes apparent. For $r = 1$ the initial power-law behavior is absent. Again, these results are averages over 500 simulations.

2.5 Discussion

The simulations given above show a wide range of behaviors from gradual failure to catastrophic failure. The principle control parameter is the range of interaction r . When the range of interaction is equal to the system size the model is in equal load sharing mode. When an element fails the stress on the element is transferred equally to all surviving elements. This is the mean-field limit for this problem. The analytic solution for this problem has been given in Eqs. (2.13) and (2.14). A gradual power-law increase in damage is found. There is no fracture propagation. All systems fail at about the same time, the standard deviation of failure times is small. The distribution of failed elements is identical to the distribution of percolating sites in site percolation. The other extreme of the behavior is nearest neighbor load sharing with $r = 1$. For the case illustrated in Fig. 2.2, the failure patch is well defined with the $\alpha = 0.05$ value of the damage parameter. Over 95% of the damage is associated with the propagating fracture. The time to failure is also much

more rapid than compared to the mean-field case. From Fig. 2.4 and with $\rho = 6$ the time to failure is $\nu_0 t_{gf} = 0.047$, this compares with an equal load sharing value $\nu_0 t_f = 1/3$. There is also a relatively large range of failure times as shown in Fig. 2.5.

2.6 References

- [1] H. E. Daniels. The statistical theory of the strength of bundles of threads. I. *Proc. Roy. Soc. Lond. A*, 183:405–435, 1945. doi: 10.1098/rspa.1945.0011.
- [2] B. D. Coleman. Time dependence of mechanical breakdown in bundles of fibers. I. Constant total load. *J. Ap. Phys.*, 28:1058–1064, 1957.
- [3] B. D. Coleman. Statistics and time-dependence of mechanical breakdown in fibers. *J. Ap. Phys.*, 29:968–983, 1958.
- [4] W. I. Newman and S. L. Phoenix. Time-dependent fiber bundles with local load sharing. *Phys. Rev. E*, 63:021507, 2001.
- [5] D. Krajcinovic. *Damage Mechanics*. Elsevier, Amsterdam, 1996.
- [6] R. Shcherbakov and D. L. Turcotte. Damage and self-similarity in fracture. *Theor. Ap. Frac. Mech.*, 39:245–258, 2003.
- [7] D. L. Turcotte, W. I. Newman, and R. Shcherbakov. Micro and macroscopic models of rock fracture. *Geophys. J. Int.*, 152:718–728, 2003.
- [8] R. Burridge and L. Knopoff. Model and theoretical seismicity. *Bull. Seismol. Soc. Am.*, 57: 341–371, 1967.
- [9] J. B. Rundle and D. D. Jackson. Numerical simulation of earthquake sequences. *Bull Seismol. Soc. Am.*, 67:1363–1377, 1977.
- [10] J. M. Carlson and J. S. Langer. Mechanical model of an earthquake fault. *Phys. Rev. A*, 40: 6470–6484, 1989.
- [11] J. B. Rundle and W. Klein. Scaling and critical phenomena in a cellular automaton slider-block model for earthquakes. *J. Stat. Phys.*, 72:405–412, 1993.

- [12] J. B. Rundle, D. L. Turcotte, R. Shcherbakov, W. Klein, and C. Sammis. Statistical physics approach to understanding the multi-scale dynamics of earthquake fault systems. *Rev. Geophys.*, 41:1019, 2003.
- [13] W. Klein, M. Anghel, C. D. Ferguson, J. B. Rundle, and J. S. Sa Martins. Statistical analysis of a model for earthquake faults with long-range stress transfer. In J. B. Rundle, D. L. Turcotte, and W. Klein, editors, *Geocomplexity and the Physics of Earthquakes*, Geophysical Monograph 120, pages 43–71. American Geophysical Union, Washington D.C., 2000.
- [14] C. A. Serino, W. Klein, and J. B. Rundle. Cellular automaton model of damage. *Phys. Rev. E*, 81(1):016105, Jan 2010. doi: 10.1103/PhysRevE.81.016105.
- [15] K. Brendel, G. T. Barkema, and H. van Beijeren. Nucleation times in the two dimensional Ising model. *Phys. Rev. E*, 71:031601, 2005.
- [16] W. A. Curtin and H. Scher. Time-dependent damage evolution and failure in materials. I. Theory. *Phys. Rev. B*, 55:12038–12050, 1997.
- [17] D. Stauffer and A. Aharony. *Introduction to Percolation Theory*. Taylor and Francis, London, second edition, 1992.
- [18] D. L. Turcotte. Self-organized criticality. *Rep. Prog. Phys.*, 62:1377–1429, 1999.

Chapter 3

A damage model based on failure threshold weakening

Abstract

A variety of studies have modeled the physics of material deformation and damage as examples of generalized phase transitions, involving either critical phenomena or spinodal nucleation. Here we study a model for frictional sliding with long range interactions and recurrent damage that is parameterized by a process of damage and partial healing during sliding. We introduce a failure threshold weakening parameter into the cellular-automaton slider-block model which allows blocks to fail at a reduced failure threshold for all subsequent failures during an event. We show that a critical point is reached beyond which the probability of a system-wide event scales with this weakening parameter. We provide a mapping to the percolation transition, and show that the values of the scaling exponents approach the values for mean-field percolation (spinodal nucleation) as lattice size L is increased for fixed R . We also examine the effect of the weakening parameter on the frequency-magnitude scaling relationship and the ergodic behavior of the model.

3.1 Introduction

The physics of progressive material damage and healing under load has been studied using models that incorporate both failure thresholds and load sharing. Models of this class include slider-block models and fiber-bundle models. In both models, external loads are applied to a “loader plate” to which the blocks or fibers are attached.

One type of avalanche model, using sliding blocks have been used to study the physics of frictional sliding, earthquakes [1, 2, 3], neural networks [4], as well as other driven threshold systems in nature. A variety of phenomena have been studied using these models, including aspects of scaling and critical phenomena [5, 6, 7, 8, 9], as well as nucleation near the spinodal. A primary focus has been placed upon understanding the origins of the frequency-size relation seen in earthquake systems [1, 2, 3, 4, 5, 6, 7, 8, 9]. Slider-block models are closely related to other types of models for distributed failure, including fiber-bundle models [10, 11, 12, 13, 14, 15] and fuse models [16] for the study of material damage and degradation and forest fire models [17].

Models for damage usually involve a system with a large number N of brittle elements such as fiber-bundles [18, 19, 20, 21]. Often the elements have a statistical distribution of strengths. An external load is applied to the system, and several failure modes are typically observed. In some models, the fibers are completely brittle, so that failure occurs when the load on the fiber reaches the fiber strength [10]. In other models, the strength of the element can degrade and weaken with time when the element load reaches a weakening value, with the time to failure dependent on the amount by which the stress exceeds the weakening value [11, 12, 13]. In these models, an upper brittle strength value allows immediate failure when the stress on the element equals or exceeds the brittle strength. In these models, a damage variable α can be defined as the fraction of elements or fibers that have failed.

Load sharing is an important property of both damage models and slider-block models. In the classical hierarchical fiber-bundle models [10, 22, 23], all fibers are connected to end plates to which the external tensional stress is applied. When a fiber fails, its load is transferred in equal parts to all the other intact fibers through the end plates.

In the slider-block model, a loader plate is connected by springs to an array of blocks sliding on a frictional surface, with the blocks interconnected by coupling springs [1, 2]. In the earliest slider-block models, a failure threshold (static friction threshold) was prescribed along with a residual or arrest stress level. Stress transfer in a slider-block model can occur through the coupling springs as well as through the loader plate. The loader plate is typically driven either by a constant applied force F or by a constant applied velocity V . The dynamics of the sliding blocks can be governed either by a set of continuous differential equations [1] or in a discrete manner using the cellular automaton approach. The cellular automaton approach lends itself well to large system sizes and is appropriate for this model under the assumption that the interevent time is much longer than the duration of an event. An extensive comparison of the continuous vs. discrete versions of the slider block model has been investigated by Xia et al. [24]

Healing is another physical process that occurs in some models of recurrent damage [25, 26, 27], and can be observed in the laboratory [28] and in nature. When an element fails, it transitions suddenly to a new state (“ruptured state”). For a process such as cracking under tensile load, separation of the crack surfaces generally precludes healing. However, for shear failure, the crack surfaces typically remain in close proximity, and healing re-strengthening is possible under certain load conditions [28]. This is the case, for example, in sliding friction experiments, where strength increases as $\log(\Delta t)$ following a slip event, where Δt is the time interval since the slip. Presumably, the same process operates on natural faults and shearing surfaces, since sudden stick-slip events are observed to reoccur regularly on these surfaces as earthquakes [29, 30], and therefore healing must occur.

To summarize our results: We study a modified cellular automaton slider-block model for damage and failure in materials leading to a family of scaling exponents that can be measured in simulations. Our model differs from a traditional slider-block model in that we have included failure threshold weakening. Subsequent failures of a block during an event, will occur at a reduced failure threshold, parameterized by w . The failure threshold weakening parameter w represents the percentage reduction of the failure threshold after a block’s initial slip. We investigate the behavior of the model as w is varied and show that above a critical value, w_c , system-wide events occur regularly. The probability of a system-wide event scales with the distance from the critical point, $w - w_c$. We examine the finite size effects and show in the limit of $L \rightarrow \infty$ the scaling exponent β , which characterizes the probability of system-wide events, approaches the corresponding order parameter exponent of mean-field percolation.

This paper is organized as follows. In section 2 we discuss details of the model we use for simulations. In section 3 we present the results of our simulations, and in section 4 we discuss the mapping to percolation theory. In particular, we compare values of scaling exponents we obtain from the simulations to values for mean-field percolation and spinodal nucleation. We also place our results into the context of other recent work on similar models, with particular attention to the question of punctuated ergodicity [31, 8, 32, 33] which has been observed in both models as well as in natural earthquake fault systems.

3.2 Model Definition

The model we investigate here is a cellular automata slider-block model. We incorporate an idea for the physics of weakening and healing proposed in a different context [34], which was

a model for damage evolution in a continuum model of the earth’s crust. Inasmuch as cellular automata slider-block models are simple systems in which to examine the physics of correlation and scaling, we have constructed a modified form of the usual slider-block model which has loader or pulling springs, connecting or interacting springs, and fixed failure and residual strengths.

Our model includes loader and coupling springs as well as additional “weakening” and “healing” properties [34]. By suitably tuning the threshold weakening, we find intervals in which a quasi-periodic earthquake cycle is observed that are dominated by large “characteristic” or “nucleation” events interspersed with time intervals in which a Gutenberg-Richter, or scaling distribution of events is observed. In the following, we investigate and extend this model further, focusing in particular on the values of scaling exponents that are observed. It will be seen that the amount of threshold weakening can be described by means of a parameter w which appears to act as a relevant scaling field in the sense of nucleation and critical phenomena.

Many dynamical models, for example forest fires [17], display clusters of sites that are typically mapped onto percolation clusters, therefore our focus in this paper is on determining how the scaling exponents for the slider-block clusters are related to the scaling exponents typical of percolation theory. In particular, as we are interested in slider-block models with long range interactions, approaching mean-field, we examine mean-field percolation models in spatial dimensions $d \geq 6$ [35], the upper critical dimension.

An example of mean-field percolation is provided by the Bethe lattice (Cayley Tree), which is equivalent to percolation in $d \rightarrow \infty$ [35]). In that problem, two of the critical exponents have the values (Stauffer and Aharony [see 35, table 2]): Order parameter exponent $\beta = 1$, and Fisher exponent $\tau = 2.5$. The remaining critical exponents can be recovered from the well-known scaling relations [35]. We note that for site percolation, the order parameter $P(p)$ can be defined as the probability that a spanning or percolating cluster is present, i.e., a cluster whose bonds connect all sides of the lattice.

Scaling in the slider-block model: In the model we consider here, each of the individual avalanches or clusters of “microscopic” blocks, which can be quite large, is considered to be a co-operative “macroscopic” slip event, or “earthquake”. Many studies have shown that if the frequency of events is plotted as a function of the number of event size (e.g. blocks in a cluster), the result is a power law of the form [5, 7, 17, 36, 37]:

$$N = \frac{N_0}{A^{\tau-1}} e^{-\varepsilon A^\sigma} \quad (3.1)$$

where τ and σ are critical exponents. Here N is the number of clusters in the simulation with area

A and ε is a scaling field. In percolation theory, equation 3.1 is called the Fisher-Stauffer droplet model [35], and $\varepsilon \propto (p - p_c)$, where p is the occupation probability and p_c is the value at the percolation threshold (critical point). In earthquake seismology, a similar scaling equation is called the Gutenberg-Richter frequency-magnitude relation [1, 2, 4, 5, 8]. The dynamics of the model are therefore reflected in the clusters of failed blocks and their statistics.

3.2.1 Base Model

We first introduce the standard cellular automata slider-block model. Our model consists of a 2d lattice of blocks sliding on a frictional surface. Our simulations are carried out on $L \times L$ square lattices ranging in size from $L = 256$ to $L = 1024$, using periodic boundary conditions. Each of the blocks is coupled to a loader plate by means of a loader spring having spring constant K_L . Each block is connected to q neighbor blocks by means of coupling springs having uniform spring constants K_C . The “total spring constant” is $qK_C + K_L$. The neighbor blocks form a square region with sides of length $2R + 1$. Thus $q = (2R + 1)^2 - 1$, where R is the range of interaction. Under rather general assumptions, it can be shown that the system can be regarded as approaching long range interactions $R \rightarrow \infty$, the mean-field limit, as $qK_C \rightarrow \infty$ [36]. Typical slider-block model dynamics occur when the loader plate is advanced in displacement until the force or stress σ on a single block meets or exceeds a failure threshold value σ_F , at which point the block is advanced a slip distance corresponding to a decrease in stress to the residual value. The residual stress value is drawn from a uniform distribution centered at σ_R with a spread of $\delta\sigma_R$ for each slip event. This small random component added to the slip distance has the effect of thermalizing the system [38].

A fraction of the stress from the slipping block is dissipated through the relaxation of the loader spring. The remaining stress is redistributed uniformly to all q neighbors. The fraction of stress dissipated is given by $D = (1 + q\frac{K_C}{K_L})^{-1}$, where D is typically in the range 10^{-2} to 10^{-1} . After stress is redistributed to neighboring blocks, they, in turn, may slip as well. The result is a cascade of slipping or failing blocks, often called an avalanche or event. We note that we use “zero-velocity” dynamics, meaning that the loader plate is advanced just enough so that only a single block is at the failure threshold at the initiation of an event and the loader plate is held fixed in location until the event has ceased. The loader plate is then advanced until the next event begins and the process is repeated. These events share much in common with avalanche phenomena in other physical systems, including sandpiles, neural networks, and electronic devices such as diodes.

We illustrate the behavior of our base model in Fig. 3.1. In Fig. 3.1(a) we plot the size

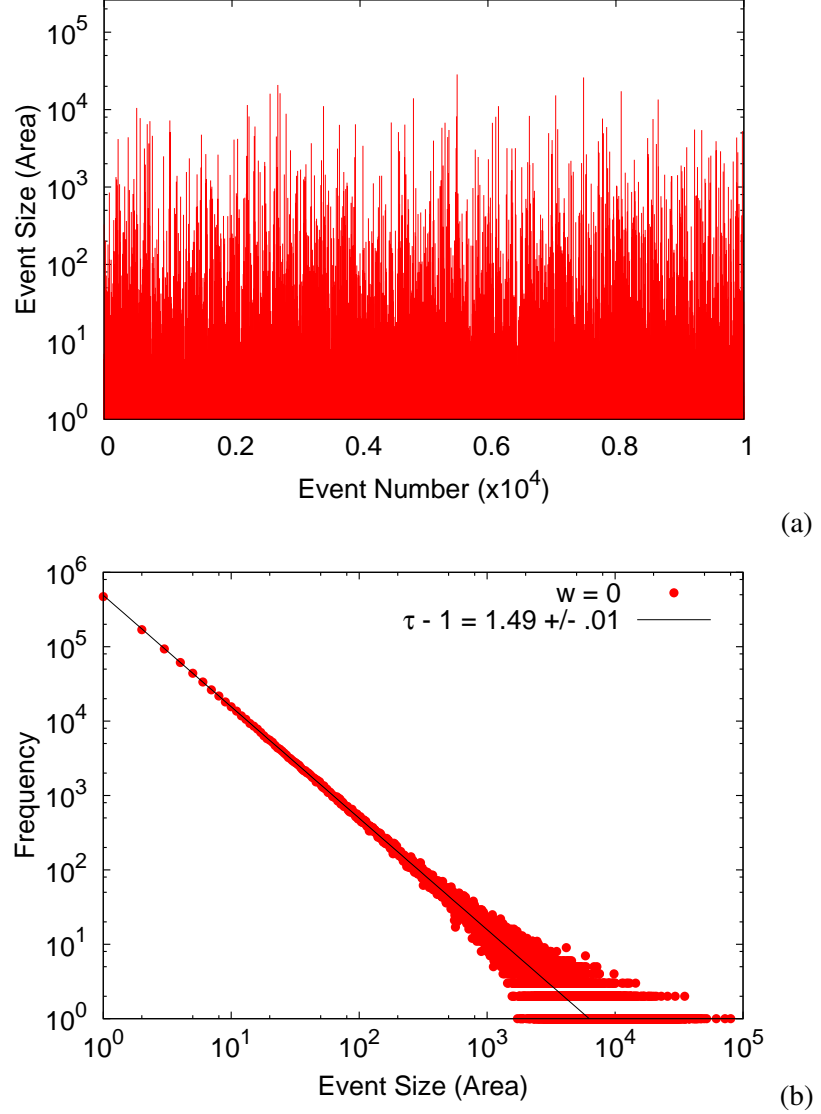


Figure 3.1: (a) A sequence of event areas A are given as a function of event number (natural time) for zero weakening ($w = 0$). A small segment of the total sequence is shown. The largest events are semi-periodic but are much smaller than the lattice area $L^2 = 512^2 = 262,144$. The other parameters of the model run are: $\sigma_F = 100$, $\sigma_R = 25 \pm 25$, $R = 15$ ($q = 960$), $K_C/K_L = 0.10$. (b) Frequency-magnitude statistics for weakening parameter $w = 0$. The frequency of events of area A , is plotted as a function of area A . The smaller events correlate well with the mean-field scaling relation taking $\tau - 1 = 1.49 \pm .01$.

of sequential avalanches A as a function of event number (natural time). The size of an avalanche is characterized by the total area (number of blocks) that slips during the event. We give results for 10,000 events from the middle of a simulation in which we collected 10^6 events. The sequence of events shown is in the steady-state regime, after a large number of transient events were discarded. To choose the system parameters, we begin with the assumption of long range interactions and then vary the stiffness of the system K_C/K_L until the model shows a steady state mean-field scaling relationship with exponent $\tau - 1 = 1.5$ after the transient effects were discarded [36]. In this simulation the system size is $L = 512$, the interaction range is $R = 15$ ($q = 960$), $K_C/K_L = 0.1$, $\sigma_F = 100$ and $\sigma_R = 25 \pm 25$. Several different values of the threshold stress σ_F , residual stress σ_R and the width of the random component of the residual stress were tested with similar results. From Fig. 3.1(a) we see a wide range of rupture areas, the largest events occurring at relatively regular intervals. No system-wide events occur and the largest events, $A \approx 25000$ are much smaller than the system size $L^2 = 262,144$. In Fig. 3.1(b) we plot the probability density function for the distribution of event sizes over the whole simulation run, the Gutenberg-Richter distribution. The frequency of events of area A is plotted as a function of area A . This plot shows the mean-field scaling relation for the frequency of events with a scaling exponent $\tau - 1 \approx 1.5$ [36].

3.2.2 Threshold damage model

Our damage model uses the cellular automaton dynamics with a failure threshold σ_F for the initial failure and slip of all blocks and a residual stress σ_R drawn from a random uniform distribution, as described above. We include damage into our model by considering any block that fails during an event to be weak or “damaged” for the remainder of the event. The first failure of all blocks occurs at an initial failure threshold of σ_F . Any subsequent failure of a damaged block (one which has slipped once or more during the current event) will occur at a reduced failure threshold value $\sigma_F * (1 - w)$, where $0 < w < 1$. The amount of damage to a block is controlled by the input weakening parameter w . Following termination of the avalanche of slipping blocks, the initial failure stress threshold of each block is reset to the original value σ_F . Thus we have damage, or weakening of the system following initial slip of each block by the ratio w , followed by healing back to the original failure threshold σ_F at the termination of the avalanche (macroscopic sliding event). In the following results, we investigate how the weakening parameter w effects the behavior of the system, particularly how beyond the critical value w_c , the weakening parameter acts as a scaling field for the probability of system-wide events to occur.

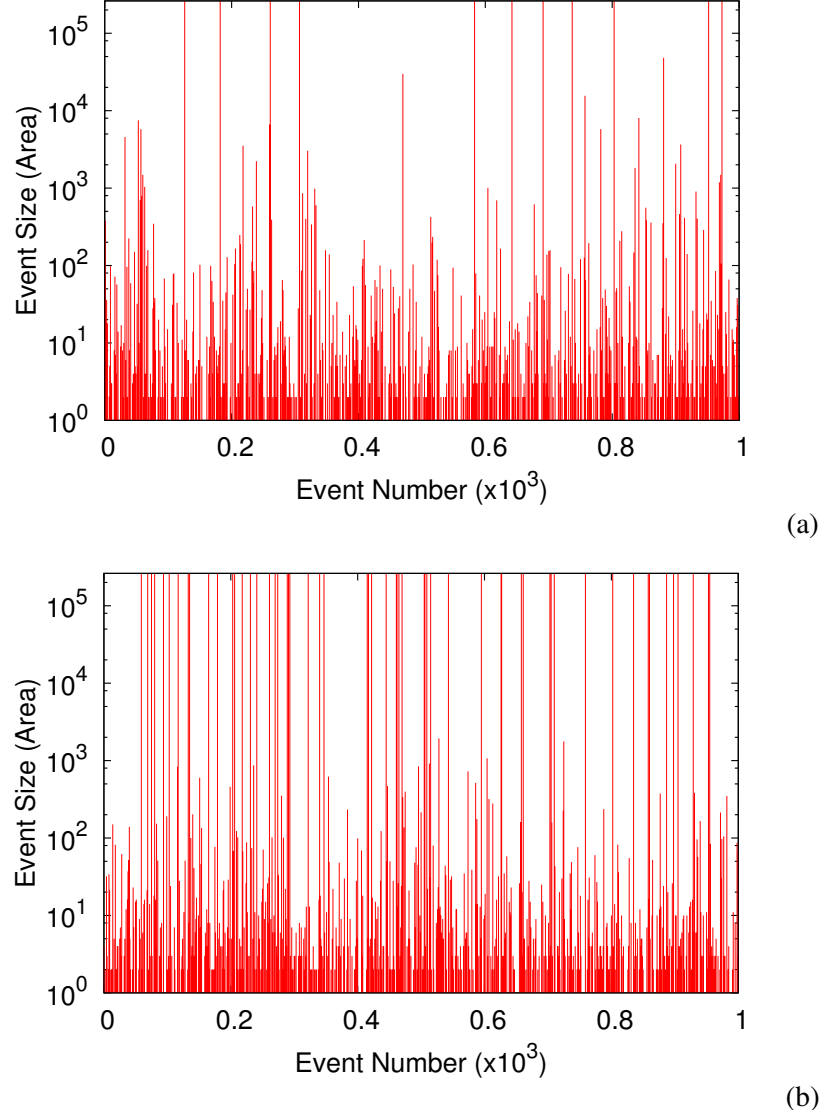


Figure 3.2: A sequence of 1000 event areas A are given as a function of event number N (natural time) for two values of the weakening parameter ($w > w_c$). We show the event sequence for (a) $w = 0.016$ and (b) $w = 0.04$. Comparing this figure to Figure 1(a) illustrates the transition through the critical point, where below the critical point no system wide events occur and above the critical point system wide events occur and grow in frequency as w is increased. System-wide events $A = L^2 = 512^2 = 262,144$ occur quasi-periodically and increase in frequency as w is increased.

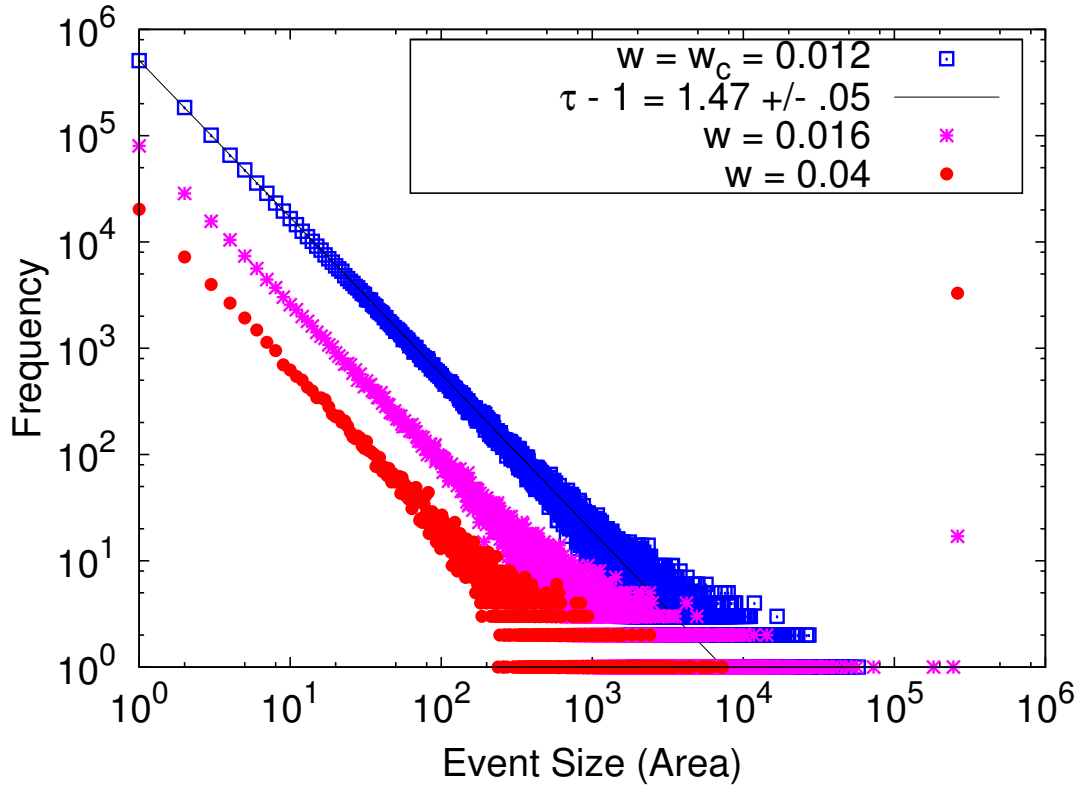


Figure 3.3: Frequency-magnitude statistics for three values of the weakening parameter: $w = w_c$ and two cases where $w > w_c$. The frequency of events of area A , is plotted as a function of area A . At the critical point $w = w_c = 0.012$ there are no system-wide events and the smaller events correlate well with equation 2.3 taking $\tau - 1 = 1.47 \pm .05$. Slightly above the critical point $w = 0.016$ large events begin to appear and there is a non-zero probability of system-wide events occurring. Far beyond the critical point $w = 0.04$ there are system-wide events occurring regularly producing the spike (lone red dot) at $A = 262,144$, while the smaller events continue to obey the GR scaling relationship with τ very near 2.5.

We next illustrate the behavior of our damage model when the weakening parameter w is greater than the critical value ($w > w_c$) so that system-wide events occur regularly. In Fig. 3.2 we plot the rupture areas A as a function of event number (natural time) for two values of the threshold weakening parameter (a) $w = 0.016$ and (b) $w = 0.04$. In Fig. 3.2(a) ($w = 0.016$), the system is slightly above the critical value and there are only a few system-wide events occurring. These system-wide events are a new behavior of the model and only appear above the critical value. As w is increased further, the system-wide events become more frequent as illustrated in Fig. 3.2(b), with $w = 0.04$. For all values of w above the critical value the system wide events occur quasi-periodically in natural time.

In Fig. 3.3 we give the frequency-magnitude (Gutenberg-Richter) distribution for cluster sizes A for three values of the weakening parameter, $w = 0.012 = w_c$, $w = 0.016 > w_c$ and $w = 0.04 > w_c$. The frequency of events of area A , is given as a function of area. For $w = w_c$, shown with boxes, there are no system-wide events and the frequency-magnitude distribution resembles that of the base model in Fig. 3.1(b). Slightly above the critical value, we show $w = 0.016$ with stars. Here a small number of large events begin to appear that are outside the scaling region of GR distribution. A few system-wide events occur that demonstrate the new behavior of the model. This data also shows an increase in the average cluster size (excluding the system-wide events), indicating an increase in the correlation length near the critical point [35]. For $w > w_c$, shown with circles, system-wide events occur regularly, producing the large spike at area $A = 262, 144$. The large gap between the GR scaling events and the system-wide events indicates that far from the critical point the average cluster size (excluding the system-wide events) is shrinking and thus, so is the correlation length. This is expected for critical point phenomena which has a diverging correlation length at the critical point [35, 39]. The system-wide events have a different structure than the smaller events. The smaller events have a diffuse structure with a mixture of failed and unfailed blocks where each failed block typically slips only once during the event. The system-wide events are dense with all blocks failing and each failed block is likely to slip multiple times during the event. Also included in this figure is the correlation between the $w = w_c$ data and the straight-line relation given in equation 2.3. Good agreement is obtained by fitting the region from $A = 1 - 1000$ giving a scaling exponent $\tau - 1 = 1.47 \pm .05$. The system parameters are the same as in 3.1 and the results are for the steady state portion of the simulation after the transient events have been discarded. Similar results are obtained for simulations using a larger lattice sizes $L = 768$ and 1024 .

3.3 Simulation Results

The primary purpose of our simulations is to study the role of the weakening parameter w . All simulations will assume a failure stress $\sigma_F = 100$, a residual stress $\sigma_R = 25 \pm 25$, and a loader spring constant $K_L = 1$ and periodic boundary conditions. For no weakening (base model), $w = 0$, system-wide clusters of failed sites in slider-block models are exceedingly rare, and appear only in the mean-field limit as $qK_C \rightarrow \infty$, or alternatively as the range of interaction $R \rightarrow \infty$ [40]. In our simulations, we find that as the weakening parameter w increases ($w > 0$), a value is reached at which system-wide events (“characteristic earthquakes”) begin to appear. Indeed, this result was noted for a different model in [34], which demonstrated that it is possible to tune such a model so that intermittency in the appearance of system-wide avalanches is observed. This suggests that we view the existence of system-wide events of failed sites in our slider-block model in a similar way to the infinite cluster in percolation, namely, that system-wide events should be associated with an order parameter and that there are associated critical exponents.

Since the weakening parameter w controls the nature of the scaling in this model, we conjecture that w plays a similar role to the occupation probability p in site percolation. Thus we define an order parameter $P(w)$ to be the ensemble average of the probability of a site (block) selected at random being part of a system-wide cluster (“characteristic event”). Here we consider system-wide events to be those that have a total area equal to the lattice area. The order parameter we have defined is analogous to the ‘strength of the infinite network’ order parameter $P(p)$ defined in percolation theory [35]. By defining a “characteristic events” as encompassing the entire lattice area, we can calculate $P(w)$ simply as the fraction of observed avalanche events that are system-wide events during the simulation run. In general we find that for $w < w_c$, $P(w) = 0$ in any finite time interval, but that for some value, $P(w) > 0$.

The value of w_c represents the value of w beyond which system-wide events (“characteristic earthquakes”) begin to appear. As discussed above we define the order parameter $P(w - w_c)$ as the ensemble average of the probability a site selected at random is part of the system-wide event, where a system-wide event encompasses then entire lattice. We calculate the order parameter as the fraction of observed avalanche events that are system-wide events. Near a critical point we would expect to find that:

$$P(w - w_c) \propto (w - w_c)^\beta. \quad (3.2)$$

The critical value of the weakening parameter w_c is estimated to be $w_c = 0.012$ for the simulation parameters used in Figs. 3.1 and 3.2. The critical value is determined by assuming the scaling

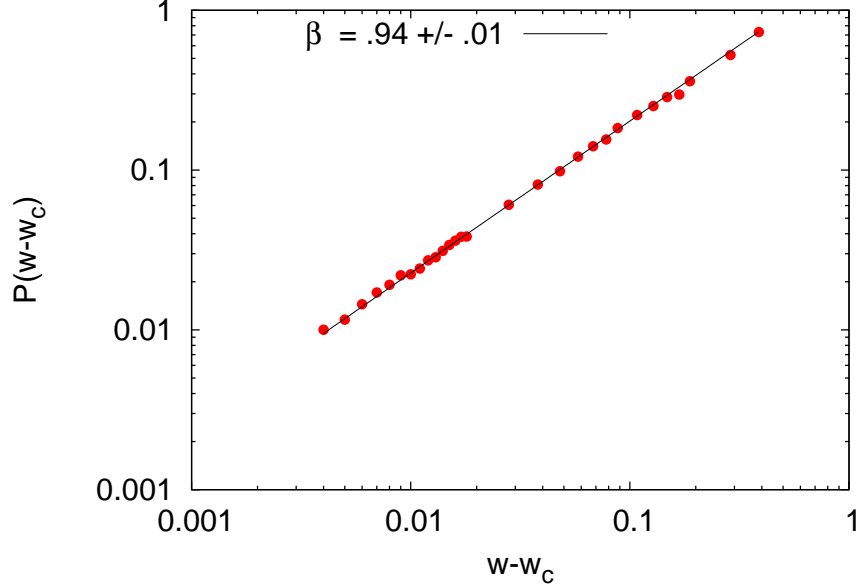


Figure 3.4: The order parameter vs the weakening value adjusted by the critical weakening value. The order parameter is defined as the probability of a system wide event occurring. The plot is on a logarithmic scale emphasizing the power-law dependence of $P(w - w_c)$ with a scaling exponent very near $\beta = 1$. The parameters of the model are the same as in Fig. 3.1.

relationship defined in 3.2 is valid and using the constraint that w_c is smaller than the first value of w produces a non-zero probability P of finding a system-wide event. The error in the reported value of w_c is .002. Examining the scaling relationship in equation 3.2 for systems of size $L = 256, 512$ and 768 suggest the value of the critical point is, at most, weakly dependent on the lattice size L . The dependence of w_c on other system parameters $q, K_C/K_L, \sigma_F$ and σ_R is currently under investigation.

In Fig. 3.4 we plot the dependence of $\log P$ on $\log(w - w_c)$ using $w_c = 0.012$. Each data point represents a simulation run with differing value of w . The range of $w - w_c$ is bounded on the right by the system that has all events spanning the entire lattice, that is $P(w - w_c) = 1$. The value of scaling exponent for the initial scaling region is near 1, the same value that characterizes mean-field percolation as defined in equation 3.2. The observed value is $\beta = 0.94$. The data presented here span roughly 2 orders of magnitude of the scaling field $w - w_c$. These results suggest the relationship between the order parameter and the scaling field is in fact a power-law relationship. We are currently investigating this model further with larger lattice sizes and varying system parameters

to increase the extent of the scaling relationship. A preliminary results suggests as we increase the system size, smaller values of $w - w_c$ yield non-zero probabilities of system-wide events, extending the scaling region to the left. In addition, the larger system sizes produce a slightly larger value of the scaling exponent β with an apparent asymptotic value of $\beta = 1$. We have measured the scaling exponent for systems with lattice dimension L of 256, 512 and 768.

3.4 Analysis

3.4.1 Scaling in non-equilibrium systems

It is well known that high dimensional models composed of interacting sites, spins, trees, cells, units, or blocks demonstrate clustering and scaling phenomena [39, 41, 42, 43]. Ising models, which are often used to demonstrate both equilibrium phase transitions (second order) and non-equilibrium transitions (nucleation), have been extensively analyzed [39]. More recently, it has been observed that non-equilibrium systems, including sandpile (self-organized critical) and forest fire models [42, 43] also exhibit clustering and scaling phenomena. For the case of slider-blocks, it was found that the energetics of the model in the near mean-field regime lead to a Boltzmann factor for the energy fluctuations [38, 8, 32]. The Boltzmann distribution of energy fluctuations, along with the apparent punctuated ergodicity as measured by the TM metric, described below, imply that the scaling properties of these models may have a similar origin to scaling properties in equilibrium systems. Later, it was found that the same ergodic property holds for coupled map lattices in the near mean-field regime [44].

For Ising models, it has been known for many years [45] that the scaling exponents associated with the Ising critical point can be mapped onto a percolation model constructed from a correlated site-bond probability. By themselves, random-site percolation clusters are not isomorphic to Ising clusters, because Ising clusters have both a correlated component, as well as a random (geometric) component. However, it was shown [45] that a bond probability can be constructed to define bond percolation clusters from the Ising spin clusters that are in fact isomorphic to random site percolation clusters. The critical exponents are the same, and the percolation critical point maps onto the Curie temperature defining the ferromagnetic-paramagnetic transition. Thus the bond probability is used to separate the correlated and geometric effects that define the Ising clusters.

For slider-block models, the physics is different but related, and in fact, simpler. Here a block fails only if the stress is large enough. So as Klein et al. [36, pg. 64] note, all clusters of failed

blocks are constructed from correlated components, and there is no need for an additional bond probability. For that reason, we expect that the scaling exponents should map directly onto those for an associated site percolation problem. Since we are dealing with a near mean-field model having long range interactions, this implies that the scaling exponents for the slider-block model should be the same as the Bethe lattice (mean-field percolation), as the range of interaction of the slider-block model becomes large. Determining the validity of this correspondence is a major motivation for the results presented here.

We have shown in Figs. 3.1(b) and 3.2(b), the frequency-magnitude scaling for the slider-block model obeys the scaling relation given in 2.3. In Fig. 3.4 we have also indicated the scaling relation between the order parameter P and the scaling field $w - w_c$ introduced into our damage model. The values $\tau - 1 = 1.51$ and $\beta = .94$, provided we are using a finite lattice, are within experimental error of the corresponding mean-field percolation model scaling exponents.

3.4.2 Ergodic Dynamics

The slider-block model is an example of a driven nonlinear threshold system where the dynamics of the system are strongly correlated in space and time. It has been shown that as the range of interaction becomes large, the slider-block model approaches a mean-field spinodal resulting in scaling phenomena, such as the frequency-magnitude (Gutenberg-Richter) shown in Fig 3.1(a) [36]. In this limit, the system resides in a metastable equilibrium, where equilibrium-like properties, such as stationary dynamics, equally probable microstates, and effective ergodicity all hold true. This metastable state is disrupted by large events, and the system evolves to a new metastable state. Therefore, the slider-block model displays punctuated or intermittent ergodicity [46].

A measure of ergodicity can be obtained using the Thirumalai-Mountain (TM) fluctuation metric [31, 47]. The TM metric, $\Omega(t)$, measures the difference between the time average of an observable at each site and its ensemble average over the entire system. The TM metric relies on the idea of statistical symmetry, where the statistics of one particle (block) is presumed identical to those of the entire system. Here the observable is the stress on each block $\sigma(t)$. The metric is defined as follows:

$$\Omega(t) = \frac{1}{N} \sum_i [\bar{\sigma}_i(t) - \langle \bar{\sigma}(t) \rangle]^2 \quad (3.3)$$

where N is the number of blocks, and the quantities $\bar{\sigma}_i(t)$ and $\langle \bar{\sigma}(t) \rangle$ are given by

$$\bar{\sigma}_i(t) = \frac{1}{t} \int_0^t dt' \sigma_i(t') \quad (3.4)$$

and

$$\langle \bar{\sigma}(t) \rangle = \frac{1}{N} \sum_i \bar{\sigma}_i(t). \quad (3.5)$$

If the system is effectively ergodic at long times, the TM metric decreases in time as, $\Omega(t) = \frac{D_e}{t}$ [31], where D_e is a diffusion constant related to the rate at which the phase space is explored. This inverse time relationship is due to the self-averaging of the observable $\sigma(t)$, without this feature, the metric will go as $1/t^2$ [see 31, pg. 42]. In Fig. 3.5, we plot the inverse of stress metric introduced in [36]. As noted above, a system is effectively ergodic if the stress metric decreases as $1/t$, therefore, a plot of the inverse metric, $\frac{1}{\Omega}$, vs time, t , will show a linear relationship for ergodic systems. In Fig. 3.5(a), we plot the inverse stress metric, with “boxes”, and the sequence of events, with “dots”, as a function of the loader plate position (time) for the “threshold damage model” at the critical point ($w = w_c$). The inverse TM metric shows a linear trend from loader plate position 300 – 600. The initial curved portion of the plot is due to transient effects. In Fig. 3.5(b), we show a small section of the plot in Fig. 3.5(a) centered on a large event of size $A \approx 50000$. Here we show that large events disrupt the ergodicity of the model for a short period of time as evident by the “kink” in the inverse TM metric. This model has punctuated ergodicity. In Fig. 3.6 we plot the inverse metric for the “threshold damage model” above the critical point. Here the system is not ergodic over any time period. The grid size events prevent the system from residing in a metastable equilibrium for a long period of time. The inverse metric is well fit to a quadratic function as noted in [31] for systems that are non-ergodic. This result is in agreement with a different adaptation of “damage” into the long-range slider-block model proposed by [33]. Here blocks in the lattice are removed and no longer contribute to the dynamics of the system after a specified number of failures. At the onset of the blocks becoming “damaged” the system loses its ergodicity.

3.5 Discussion

We have discussed the various types of simulations used to model the physics of material deformation and damage, including fiber-bundle models and slider-block models as well as the experimental and observational motivation for incorporating damage and healing into these models. We infer that healing must occur on faults where stick-slip events (earthquakes) occur regularly, motivating the addition of damage and partial healing into a traditional earthquake model. We

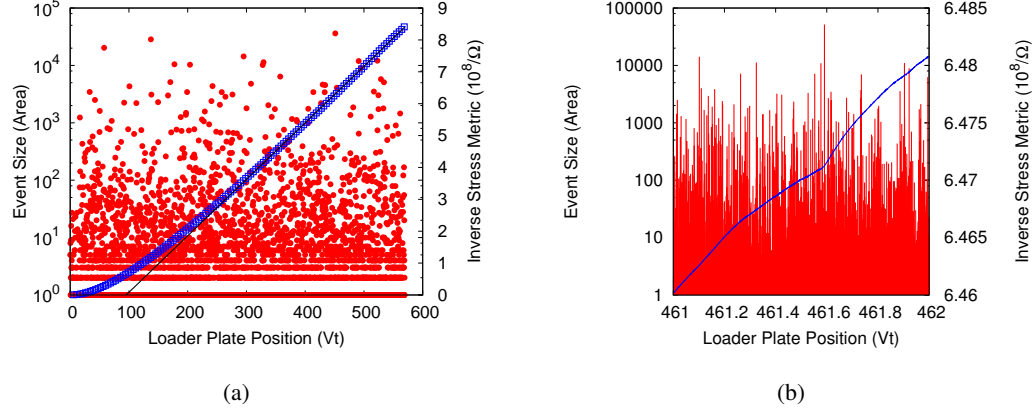


Figure 3.5: The inverse TM metric for measuring effective ergodicity is overlayed with the event size sequence as a function of loader plate position, for the "threshold damage model" at the critical point $w = w_c$. A system is effectively ergodic if the stress metric decreases as $1/t$. In (a) we plot the inverse TM metric vs loader plate position (time). This plot shows a linear trend, displaying the system is effectively ergodic from $Vt = 300 - 600$. In (b), we show a detailed view of a break in the ergodicity caused by a large event.

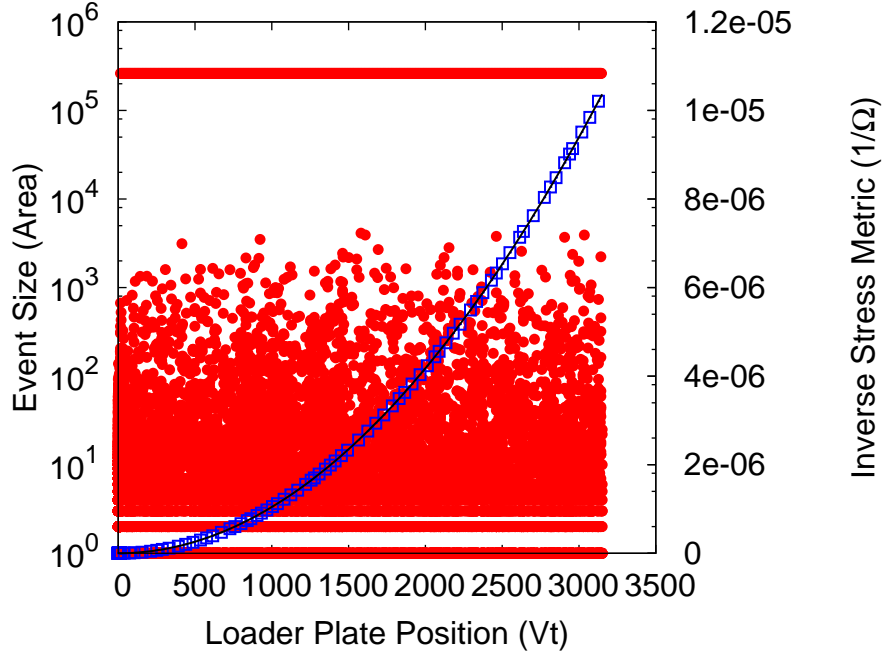


Figure 3.6: The inverse TM metric and the event size sequence are shown for the "threshold damage model" above the critical point ($w > w_c$). The inverse metric shows a t^2 trend, displaying that this model is not ergodic over the observed time period. The grid-size events, shown with "dots", prevent the system from residing in a meta-stable equilibrium for any extended period of time.

included the concept of damage and healing into the standard cellular-automata slider-block model by means of failure threshold weakening. We reduced (“damaged”) each block that slips during an event by allowing subsequent failures of the damaged blocks to occur at a lower failure threshold parameterized by w . After the event has terminated we heal all blocks to their original failure threshold levels.

We have shown that the weakening parameter w behaves as a scaling field for the ensemble average probability of a site selected at random to be part of a system-wide event $P(w - w_c)$, just as the occupation probability is a scaling field for the strength of the infinite network in percolation theory. We also discussed the mean-field percolation problem along with the various critical exponents that can be measured. The results of our simulation yield scaling exponents that approach those of the in Bethe lattice (mean-field) percolation problem, specifically $\beta = 1$. We have demonstrated that the “threshold weakening model” displays ergodic behavior up to the critical point. Beyond the critical point w_c , the model is no longer ergodic. We conclude that “damage” as we have modeled it, is a non-equilibrium process. We have also shown the scaling exponents found in our slider-block model to be within the range of those found in experiments. We conclude that the mean-field interactions may dominate the failure of material.

It is useful to compare the scaling exponents determined from our numerical simulations with scaling exponents seen in laboratory experiments and in nature. In all of these experiments, the fracturing and acoustic emissions are mixed-mode, not simple shear sliding as is the case for our simulations. As a result, we expect to observe a range of values for scaling exponents. Typically, the data are in the form of probability density function (PDF) as a function of energy E of acoustic emissions (AE). For frequency vs. energy measurements, and assuming that area of microcrack is proportional to energy released, which would be the case if crack area is proportional to crack energy for these microcracks, a range of scaling exponents $\tau - 1$ are observed, from 1.2 to 2.0, with most values clustering around 1.5 as is observed in our simulations [48, 49, 50, 51]. On the other hand, if crack energy released is proportional to crack area to the 3/2 power, as is the case for macroscopic cracks, then we would expect scaling exponents at the lower end of the observed range, clustering around $\tau - 1 = 1.0$.

The model we present here is limited by the discrete dynamics for stress accumulation, dissipation and redistribution. A follow up study of the threshold weakening parameter introduced here, applied to a continuous slider-block model [24], would be of considerable interest. We expect, although the dynamics are different, the scaling exponent β will approach 1 for the appropriate system parameters. In addition, further studies of this model including an investigation of time de-

pendent healing are currently being studied. Here we raise the failure threshold of each block at a rate proportional to $\log(t)$ where t is the time since the last slip of that block. This is motivated by the static friction "healing" experiment conducted by Dieterich [28]. Initial results from this study indicate the logarithmic healing changes the inter-event time distribution following a "characteristic" event from exponential to a inverse power-law distribution.

3.6 References

- [1] R. Burridge and L. Knopoff. Model and theoretical seismicity. *Bull. Seismol. Soc. Am.*, 57: 341–371, 1967.
- [2] J. B. Rundle and D. D. Jackson. Numerical simulation of earthquake sequences. *Bull Seismol. Soc. Am.*, 67:1363–1377, 1977.
- [3] S. R. Brown, C. H. Scholz, and J. B. Rundle. A simplified spring-block model of earthquakes. *Geophys. Res. Lett.*, 18:215–218, 1991.
- [4] A. V. M. Herz and J. J. Hopfield. Earthquake cycles and neural reverberations: collective oscillations in systems with pulse-coupled threshold elements. *Phys. Rev. Lett.*, 75:1222–1225, 1995.
- [5] J. M. Carlson and J. S. Langer. Properties of earthquakes generated by fault dynamics. *Phys. Rev. Lett.*, 62:2632–2635, 1989.
- [6] J. B. Rundle and W. Klein. Nonclassical nucleation and growth of cohesive tensile cracks. *Phys. Rev. Lett.*, 63:171–174, 1989.
- [7] J. B. Rundle, W. Klein, and S. Gross. Dynamics of a traveling density wave model for earthquakes. *Phys. Rev. Lett.*, 76:4285–4288, 1996.
- [8] W. Klein, J. B. Rundle, and C. D. Ferguson. Scaling and nucleation in models of earthquake faults. *Phys. Rev. Lett.*, 78:3793–3796, 1997.
- [9] J. B. Rundle, W. Klein, S. Gross, and C. D. Ferguson. The traveling density wave model for earthquakes and driven threshold systems. *Phys. Rev. E*, 56:293–307, 1997.
- [10] H. E. Daniels. The statistical theory of the strength of bundles of threads. I. *Proc. Roy. Soc. Lond. A*, 183:405–435, 1945. doi: 10.1098/rspa.1945.0011.

- [11] W. A. Curtin, M. Pamel, and H. Scher. Time-dependent damage evolution and failure in materials. II. Simulations. *Phys. Rev. B*, 55:12051–12061, 1997.
- [12] W. I. Newman and S. L. Phoenix. Time-dependent fiber bundles with local load sharing. *Phys. Rev. E*, 63:021507, 2001.
- [13] S. L. Phoenix and W. I. Newman. Time-dependent fiber bundles with local load sharing. II. General Weibull fibers. *Phys. Rev. E*, 80:066115, 2009.
- [14] Srutarshi Pradhan, Alex Hansen, and Bikas K. Chakrabarti. Failure processes in elastic fiber bundles. *Rev. Mod. Phys.*, 82(1):499–555, 2010.
- [15] F. Kun, S. Zapperi, and H. J. Herrmann. Damage in fiber bundle models. *Eur. Phys. J. B*, 17(2):269–279, 2000.
- [16] S. Zapperi, A. Vespignani, and H. E. Stanley. Plasticity and avalanche behavior in microfracturing phenomena. *Nature*, 388:658–660, 1997.
- [17] B. Drossel and F. Schwabl. Self-organized critical forest fire model. *Phys. Rev. Lett.*, 69:1629–1632, 1992.
- [18] S. R. Pride and R. Toussaint. Thermodynamics of fiber bundles. *Physica A*, 312:159–171, 2002.
- [19] D. L. Turcotte, W. I. Newman, and R. Shcherbakov. Micro and macroscopic models of rock fracture. *Geophys. J. Int.*, 152:718–728, 2003.
- [20] A. Virgili, A. Petri, and S. R. Salinas. A thermodynamical fibre bundle model for the fracture of disordered materials. *J. Stat. Mech.: Th. & Exp.*, 2007. doi: 10.1088/1742-5468/2007/04/P04009.
- [21] H. Nechad, A. Helmstetter, R. E. Guerjouma, and D. Sornette. Andrade and critical time-to-failure laws in fiber-matrix composites: Experiments and models. *J. Mech. Phys. Sol.*, 53:1099–1127, 2005.
- [22] F. T. Pierce. Tensile tests for cotton yarns, V: The weakest link, Theorems on the strength of long and short composition. *J. Textile Inst.*, 17:355–375, 1926.

- [23] W. I. Newman, D. L. Turcotte, and A. M. Gabrielov. Log-periodic behavior of a hierarchical failure model with applications to precursory seismic activation. *Phys. Rev. E*, 52:4827–4835, 1995.
- [24] Junchao Xia, Harvey Gould, W. Klein, and J. B. Rundle. Near-mean-field behavior in the generalized burridge-knopoff earthquake model with variable-range stress transfer. *Phys. Rev. E*, 77(3):031132, 2008.
- [25] V. Lyakhovsky, Y. Ben-Zion, and A. Agnon. A viscoelastic damage rheology and rate- and state-dependent friction. *Geophys. J. Int.*, 161:179–190, 2005.
- [26] V. Lyakhovsky. Scaling of fracture length and distributed damage. *Geophys. J. Int.*, 144: 114–122, 2001.
- [27] I. G. Main. A damage mechanics model for power-law creep and earthquake aftershock and foreshock sequences. *Geophys. J. Init.*, 142:151–161, 2000.
- [28] J.H. Dieterich. Modeling of rock friction, 1, experimental results and constitutive relations. *J. Geophys. Res.*, 84:2161–2168, 1979.
- [29] Y. Hamiel, O. Katz, V. Lyakhovsky, Z. Reches, and Y. Fialko. Stable and unstable damage evolution in rocks with implications to fracturing of granite. *Geophys. J. Int.*, 167:1005–1016, 2006.
- [30] O. Katz and Z. Reches. Microfractureing, damage, and failure of brittle granites. *J. Geophys. Res.*, 109, 2004. doi: doi:10.1029/2002JB001961d.
- [31] D. Thirumalai and R. D. Mountain. Ergodic convergence properties of supercooled liquids and glasses. *Phys. Rev. A*, 42:4574–4587, 1990.
- [32] K. F. Tiampo, J. B. Rundle, W. Klein, J. S. Sá Martins, and C. D. Ferguson. Ergodic dynamics in a natural threshold system. *Phys. Rev. Lett.*, 91:238501, 2003.
- [33] C. A. Serino, W. Klein, and J. B. Rundle. Cellular automaton model of damage. *Phys. Rev. E*, 81(1):016105, Jan 2010. doi: 10.1103/PhysRevE.81.016105.
- [34] Y. Ben-Zion, K. Dahmen, V. Lyakhovsky, D. Ertas, and A. Agnon. Self-driven mode switching of earthquake activity on a fault system. *Earth Planet. Sci. Lett.*, 172/1-2:11–21, 1999. doi: 10.1016/S0012-821X(99)00187-9.

- [35] D. Stauffer and A. Aharony. *Introduction to Percolation Theory*. Taylor and Francis, London, second edition, 1992.
- [36] W. Klein, M. Anghel, C. D. Ferguson, J. B. Rundle, and J. S. Sa Martins. Statistical analysis of a model for earthquake faults with long-range stress transfer. In J. B. Rundle, D. L. Turcotte, and W. Klein, editors, *Geocomplexity and the Physics of Earthquakes*, Geophysical Monograph 120, pages 43–71. American Geophysical Union, Washington D.C., 2000.
- [37] X. Gabaix, P. Gopikrishnan, V. Plerou, and H. E. Stanley. A theory of power-law distributions in financial market fluctuations. *Nature*, 423:267–270, 2003.
- [38] J. B. Rundle, W. Klein, S. Gross, and D. L. Turcotte. Boltzmann fluctuations in numerical simulations of nonequilibrium threshold systems. *Phys. Rev. Lett.*, 75:1658–1661, 1995.
- [39] N. Goldenfeld. *Lectures on Phase Transitions and the Renormalization Group*. Addison-Wesley, Reading, MA, 1992.
- [40] P. Grassberger. Efficient large-scale simulations of a uniformly driven system. *Phys. Rev. E*, 49:2436–2444, 1994.
- [41] B. D. Malamud and D. L. Turcotte. Cellular automata models applied to natural hazards. *Comp. Sci. Eng.*, 2:42–51, 2000.
- [42] P. Bak, C. Tang, and K. Wiesenfeld. Self-organized criticality. *Phys. Rev. A*, 38:364–374, 1988.
- [43] S. Clar, B. Drossel, and F. Schwabl. Forest fires and other examples of self-organized criticality. *J. Phys: Condensed Matter*, 8:6803–6824, 1996.
- [44] D. A. Egolf. Equilibrium regained: From nonequilibrium chaos to statistical mechanics. *Science*, 287:101–104, 2000. doi: 10.1126/science.287.5450.101.
- [45] A. Coniglio and W. Klein. Clusters and Ising critical droplets: A renormalization group approach. *J. Phys A: math Gen.* 13, pages 2775–2780, 1980.
- [46] C. D. Ferguson, W. Klein, and J. B. Rundle. Spinodals, scaling, and ergodicity in a threshold model with long-range stress transfer. *Phys. Rev. E*, 60:1359–1373, 1999.
- [47] D. Thirumalai, , and R. D. Mountain. Activated dynamics, loss of ergodicity, and transport in supercooled liquids. *Phys. Rev. E*, 47:479–489, 1993.

- [48] M. B. J. Meinders and Ton van Vliet. Scaling of sound emission energy and fracture behavior of cellular solid foods. *Phys. Rev. E*, 77:036116, 2008.
- [49] C. Maes, A. VanMoffaert, H. Frederix, and H. Strauven. Criticality in creep experiments on cellular glass. *Phys. Rev. B*, 57:4987–4990, 1998.
- [50] P. A. Houle and J. P. Sethna. Acoustic emission from crumpling paper. *Phys. Rev. E*, 54: 278–283, 1996.
- [51] A. Garcimartin, A. Guarino, L. Bellon, and S. Ciliberto. Statistical properties of fracture precursors. *Phys. Rev. Lett.*, 79:3202–3205, 1997.

Chapter 4

A possible mechanism for aftershocks: Damage and time-dependent failures

Abstract

We propose a time-dependent slider-block model which incorporates a time-to-failure function for each block dependent on the stress. We associate this new time-to-failure mechanism with the property of stress fatigue. We test two failure time functions including a power-law and an exponential. Failure times are assigned to “damaged” blocks with stress above a damage threshold, σ_W and below a static failure threshold, σ_F . If the stress of a block is below the damage threshold the failure time is infinite. During the aftershock sequence the loader-plate remains fixed and all aftershocks are triggered by stress transfer from previous events. This differs from standard slider-block models which initiate each event by moving the loader-plate. We show the resulting behavior of the model produces both the Gutenberg-Richter scaling law for event sizes and the Omori’s scaling law for the rate of aftershocks when we use the power-law failure time function. The exponential function has limited success in producing Omori’s law for the rate of aftershocks. We conclude the shape of the failure time function is key to producing Omori’s law.

4.1 Introduction

The physics of earthquakes is often investigated through simple models. The underlying concept in creating these minimalistic models is pinpointing the physics that produces results comparable with nature, without being overwhelmed by the complexity of the problem. Several models

have been proposed that successively demonstrate Gutenberg-Richter scaling for event magnitudes. One property of earthquakes these models have not had as much success reproducing, however, is Omori's law for the rate of decay of aftershocks following a mainshock.

A model commonly used to describe earthquakes that does not have well defined aftershocks is the slider-block (or spring-block) model. Originally proposed by Burridge and Knopoff [1], this model was transformed into a cellular automata (CA) version by Rundle and Jackson [2] and again by Rundle and Brown [3]. It is often referred to as the RJB model. This CA slider-block model has been shown to produce power-law statistics for the frequency of events of magnitude m , that follow Gutenberg-Richter scaling for earthquakes [2, 3, 4, 5]. This model does have limitations. For example, each event is triggered by a loader-plate update. In other words, all events are initiated by external driving forces rather than internal redistributions of stress. Thus, when comparing the slider-block model to observed earthquakes, one has to assume a substantial amount of time passes between each loader-plate triggered event. Events occur independently of each other in time and thus, there is no temporal clustering beyond random clustering. In this light, there are no well defined foreshocks or aftershocks. However, the RJB model is advantageous to research the basic physical principles contributing to earthquake scaling laws due to its simple rules, ease of programming and speed of simulations. For these reasons it has often been used to test additional physical principles, such as damage and threshold weakening [6, 7].

In this paper, we investigate the addition of stress fatigue and subsequent time-delayed failures triggering events in the CA slider-block model. The motivation is to produce aftershock sequences which obey Omori's law as well as retain the Gutenberg-Richter scaling for event magnitudes, all while maintaining simple physics. Stress fatigue introduces a time-dependent failure mechanism for the CA slider-block model that occurs after each loader-plate update. Now, in addition to the static failure threshold where slips occur instantaneously, a lower damage threshold is assigned to each block which marks the onset of stress fatigue. A block with stress above the damage threshold will be assigned a failure time as a function of stress and will be allowed to slip at a stress below the static failure threshold. We retain the instantaneous healing process from the original CA slider-block model. This modification allows multiple events to occur after the initial loader-plate triggered event and within this sequence we can define a mainshock, foreshocks and aftershocks.

The focus of this model is on the time dependence of the rate of aftershocks and the compliance of the resulting sequence of events with the known scaling relations for earthquakes and aftershocks. These scaling relations include: Gutenberg-Richter scaling for frequency of event

magnitudes [8], Omori's Law for scaling of the rate of aftershock occurrence following a main-shock [9], and Bath's Law for the magnitude of the largest aftershock [10].

Gutenberg-Richter distributions are cumulative distributions for the number of events occurring greater than size m :

$$N(>m) \propto m^{-b} \quad (4.1)$$

This scaling relationship is observed in nature for aftershock sequences, and both global and regional earthquake catalogs with a scaling exponent of approximately $b = 1$ [8]. In the slider-block model the same frequency-magnitude relationship can be described using a probability distribution function:

$$N \propto A^{-b'} \quad (4.2)$$

where A is the area of the events.

Omori's Law applies only to aftershocks and is independent of event magnitudes. The rate of events occurring within a time window τ_w as a function of time follows the inverse power law:

$$\frac{N}{\tau_w}(t) \propto t^{-p} \quad (4.3)$$

The size of τ_w is unimportant to the power-law relationship, but allows the definition of rate of events. The values of p varies from earthquake to earthquake with a range of approximately $1 < p < 1.2$ [11].

Bath's law suggests the largest aftershock will be approximately one unit of magnitude smaller than the mainshock of the same sequence:

$$M_{MS} - M_{AS} = 1.2 \quad (4.4)$$

Under the assumption that the moment is proportional to the area, Bath's law implies the area of the mainshock should be 10 times larger than the area of the largest aftershock [10, 12]. For a range of model parameters, the time-dependent slider-block model satisfies these three scaling relationships.

This paper is organized as follows: First, we will define the CA slider-block model with long range interactions, the assumptions in creating the time-dependent model, and the modifications that allow time-dependent failures, including the additional damage threshold parameter. Next we will show the resulting behavior for the time-dependent slider-block model complies with equations (4.1)- (4.4) using two failure time functions. Last, we will discuss our results and compare this model to a similar lattice model proposed by Dieterich [13] using rate and state friction [14, 15] to

produce aftershocks. This model incorporates both a time-dependent failure mechanism and a time-dependent healing process, to promote aftershocks. Rate and state friction, however, is controversial since the physical meaning of the state variable is unclear.

4.2 The slider-block model

Here we describe the CA slider-block model in the zero-velocity limit as defined by Klein et al. [5]. A 2D lattice of blocks is constructed in which each block is connected to a loader-plate with a loader spring of spring constant K_l . It is assumed the lattice is square, but this is not necessary. Each block is then connected to a surrounding neighborhood of blocks with coupling springs of uniform spring constant K_c . The interacting neighborhood is a square region centered on each block with a linear dimension $2r + 1$. The total number of interacting neighbor blocks is $q = (2r + 1)^2 - 1$. The total spring constant for each block is then $K_T = qK_c + K_l$. The uniform interaction strengths used here are a simplification of a more realistic $1/r^3$ decaying interaction strength for two dimensional dislocations in linear elastic media [16]. It has been shown, however, this simplification produces consistent Gutenberg-Richter scaling with the $1/r^3$ interaction, while allowing simulations to run on smaller lattices [17, 5], and is thus ideal for our simple computer simulations. The use of long range interactions is essential for event areas to obey a power-law scaling relationship.

Each block is assigned a static failure threshold σ_F , which can be uniform or spatially varying. If the stress on a block overcomes this threshold, the block will slip and subsequently redistribute stress through the coupling springs to neighboring blocks. The dynamics of the model are as follows: The loader-plate position is increased, which add stress uniformly to all blocks, until a single block reaches its failure threshold. This will be the “seed” block for the first event. This block then slips according to the slip rule

$$\Delta x = \frac{\Delta\sigma}{K_T} = \frac{\sigma - \sigma_R}{qK_c + K_l}. \quad (4.5)$$

σ_R here is a residual stress that remains on the block after slip occurs. We include noise in the slip rule by choosing a random residual stress, σ_R , for each slip of each block. That is

$$\sigma_R = \eta * \sigma_{Rmax}, \quad (4.6)$$

where η is drawn from a uniform distribution between 0 – 1 and σ_{Rmax} is an input parameter. A portion of the stress that is lost from the block that slips is dissipated through the relaxation of

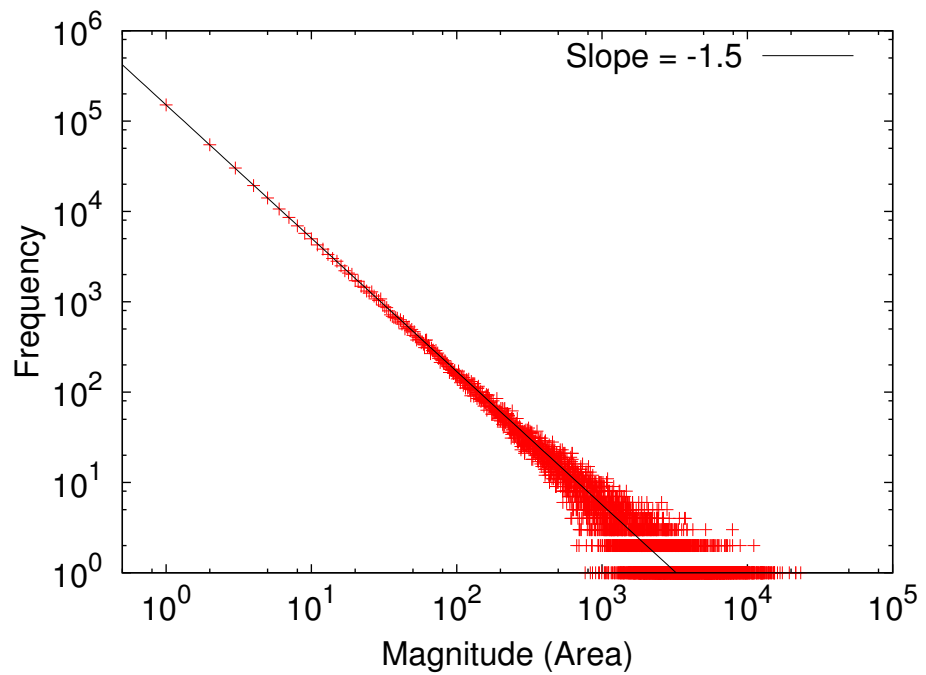


Figure 4.1: The Gutenberg-Richter scaling for the CA slider-block model with long range interactions is shown here. The scaling relationship shows a scaling exponent of approximately $b' = 1.5$. This agrees previously published results [5]

the loader spring, while the remaining stress is uniformly distributed to the q blocks within the interaction region. Specifically the fraction of stress dissipated D , and redistributed R , are

$$D = \frac{K_l}{K_T}, \quad R = 1 - D = \frac{qK_c}{K_T}. \quad (4.7)$$

After the stress is redistributed following the slip of the initial “seed” block, all neighboring blocks that now have a stress greater than their respective thresholds slip according to the same slip rule, Eq. (4.5). This process is continued until all the blocks are below their failure stress thresholds.

All blocks that slipped following a single loader-plate update combine to form an “event”, and the event size, or area, is defined as sum of these blocks. Event sizes are confined to the range $[1, L^2]$, where L is the lattice dimension and L^2 is the total number of blocks in the lattice.

In Fig. 4.1, a frequency-magnitude distribution for event areas is shown. The parameters used for this simulation are $L = 256$, $\sigma_F = 100$, $\sigma_R = 50$, $K_c = 0.1$, $K_l = 1$, $r = 12$. There are a total of 400,000 events plotted after a sufficient transient period has passed. The distribution shows a power-law relationship with a scaling exponent of $b' = 1.5$. This is the expected value for long-range slider-block models in the limit of no frictional velocity dependence [5, 18].

It is assumed in the rules of this model that the time between two events initiated by the loader-plate is much longer than the duration of an event. In this regard the time it takes to transfer stress and cause a cascade of failures during an event can be considered instantaneous. This leads to the conclusion that only one event occurs during a single loader-plate update and thus there are necessarily no foreshocks or aftershocks by the action of this model.

4.3 Time-dependent slider-block model

The new modification to the standard slider block model produces a sequence of events following each loader-plate update. The system is identical to the CA slider-block model above with the addition of one attribute. The blocks are given, not only a static failure threshold σ_F , but also a lower damage stress threshold, σ_W . Any block whose stress lies between σ_W and σ_F is considered damaged (or weakened) and is assigned a time-to-failure, which is calculated as a function of the block’s stress. The damaged threshold represents the onset of static fatigue, in which failure is delayed but occurs at a stress lower than the static failure threshold. This procedure of allowing time dependent failures above a specified threshold is commonly performed in fiber-bundle models [19, 20, 21, 22, 23], and is adapted here for the slider-block model.

4.3.1 Assumptions

There are three assumptions in the creation of this model. 1) The new failure mechanism, stress fatigue, is applied only to those blocks that are within the elastically loaded region. This region surrounds a fracture or earthquake and is defined as the region where stress is transferred. In the slider-block model all blocks that slip during an avalanche transfer energy through the coupling springs to all blocks within their range of interaction. After an event has arrested, the elastically loaded region contains all blocks within the range of interaction R of the event's perimeter. It is in this region where failure times will be assigned and aftershock events will initiate. 2) A non-zero, finite, time-to-failure is assigned only to “damaged” blocks whose stress is above a damage threshold, σ_W , but below a static failure threshold, σ_F , where blocks slip immediately [24]. In this model, damage to a block can only occur by a sudden increase in the applied stress. This is the case during an event from a stress transfer of a slipped neighbor, but not from the slow increase of stress from the loader plate. And, 3) The duration of an event is much much smaller than any calculated time-to-failure while the calculated time-to-failure is much much smaller than the time between loader-plate triggered events.

$$t_{\text{event}} \ll t_{\text{failure}} \ll t_{\text{loader-plate}} \quad (4.8)$$

This allows the loader plate to be held fixed while the aftershock event sequence occurs. We further hypothesize, the time-to-failure is a maximum if the stress is equal to the damage threshold and goes to zero as the stress increases to the static failure threshold. Therefore the failure time should be a function of the stress difference between the static failure threshold and stress on the block.

$$t_f = \begin{cases} \infty & \sigma < \sigma_W \\ f(\sigma_F - \sigma) & \sigma_W \leq \sigma < \sigma_F \\ 0 & \sigma \geq \sigma_F \end{cases} \quad (4.9)$$

We are free to choose any form of the failure-time function, $f(\sigma)$, but, as noted by Amitrano and Helmstetter [19] and the references therein, experimental and theoretical results suggest failure-times decrease with increasing stress according to either a power-law or an exponential. Also, Díeterich [13] suggests a stress increase of $\Delta\sigma$ from a nearby event can alter the rupture time (or nucleation time) by a factor proportional to $\exp(-\Delta\sigma)$. This motivates us to construct both a power-law and an exponential function for the time-to-failure:

$$f(\sigma_F - \sigma) = \tau_0 \left(\frac{\sigma_F - \sigma}{\sigma_F - \sigma_W} \right)^\rho \quad (4.10)$$

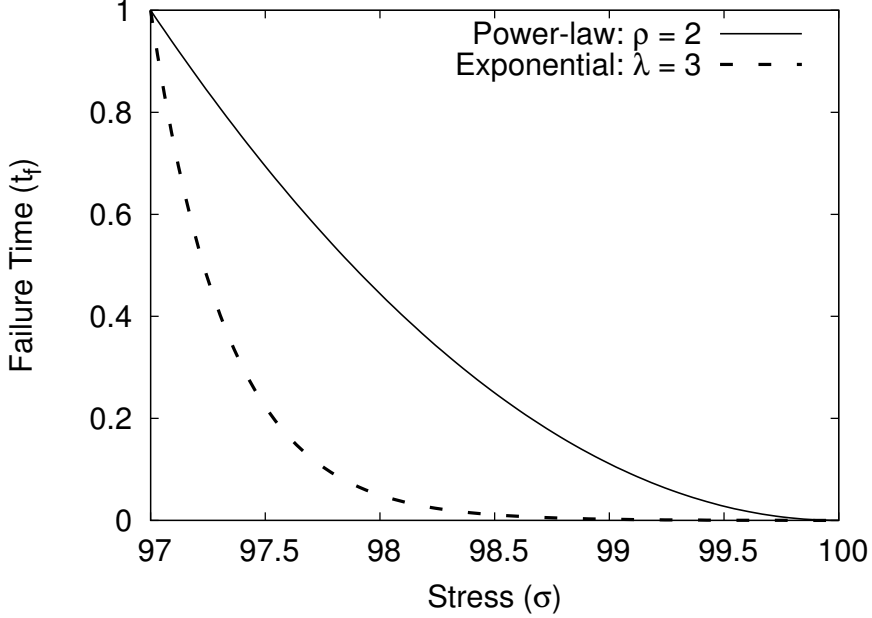


Figure 4.2: Here we plot the failure-time functions given in Eqs. (4.10) and (4.11). A time-to-failure is assigned to blocks only if the stress on that block is above the damage threshold, σ_W and below a static failure threshold, σ_F . Above σ_F the time-to-failure is zero and below the damage threshold, σ_W , the time-to-failure is infinite. Here we plot two failure-time functions, a power-law and an exponential. The values of σ_W and σ_F are 97 and 100 respectively, for both functions.

$$f(\sigma_F - \sigma) = \tau_0 \frac{e^{\lambda(\sigma_F - \sigma)} - 1}{e^{\lambda(\sigma_F - \sigma_W)} - 1} \quad (4.11)$$

These functions differ slightly from those presented in Amitrano and Helmstetter [19, Eqs. 3 & 4]. However, over the short range of stress that they are applied the shape of the failure time functions are very similar to those in [19]. As will be discussed later, the shape of the failure-time function is the key for the realization of Omori's law.

A plot of these failure-time functions is provided in Fig. 4.2. In this plot we have set $\sigma_W = 97$ and $\sigma_F = 100$ and failure-time function parameters ρ and λ to 2 and 3 respectively. These parameters are representative of parameters used in the simulation results presented below. The time-to-failure function is normalized so that the maximum failure-time, which corresponds to a stress of σ_W , is equal to $t_f = 1$ for both functions. Thus 1 unit of time is the duration required for a block at the damage threshold to fail. τ_0 has the units of time and included for just that reason. We use the term “aftershock time counter” to represent the clock that tracks the evolution of the model and will be represented by the symbol t .

4.3.2 Dynamics

The time-dependent slider-block model is run as follows: The loader-plate is advanced until a single block reaches the static failure stress threshold σ_F , and the aftershock-time counter is set to zero. This block then slips and the event proceeds according to the standard slider-block model rules described above. After this loader-plate event terminates, all blocks are at a stress below the static failure stress threshold. The aftershock-time counter remains at $t = 0$ due to the assumption that events occur instantaneously in comparison with the other time scales in the model. The loader-plate is now held fixed and does not add any stress to the system for the following sequence of aftershock events. The time-dependent stress relaxation process controls the remaining events prior to the next loader-plate update.

Any block that is within the elastically loaded region of the loader-plate event AND has a stress above the damage threshold, σ_W , is assigned a failure time according to Eq. (4.10). This is the application of assumptions 1 & 2 from above. The aftershock-time counter is then advanced to the minimum failure time, $t = t_{f,min}$. The block with this minimum failure time is the “seed” block for the next event, which from here on will be called the “first failure-time event”. Assumption 3 suggests all slips within a failure-time event occur at the static failure threshold according to Eq. (4.5). Note, only the “seed” block fails at a stress below the static failure threshold. That is, time dependent failures apply only to “seed” blocks of the aftershock events and all blocks that slip mid-event occur at the static failure threshold σ_F .

After the termination of the first failure-time event, there is a new elastically loaded region on the lattice. It is now a combination of the loaded region of the initial event and the loaded region of the first failure-time event. To initiate the second failure-time event, we first calculate failure times for all blocks within this new elastically loaded region. The blocks within this new loaded region can be categorized into four groups. First there are those with a stress below the damage threshold, σ_W . These blocks are left alone with a failure-time of $t_f = \infty$. Second, there are blocks with a stress above the σ_W which do not have a previously assigned failure time. These are assigned a failure time according to Eq. (4.10). Third, there are blocks with a stress above σ_W , have a previously assigned failure time and endured a stress increase during the first failure-time event. These blocks are also assigned a new failure time according to Eq. (4.10). And last, there are blocks with a stress above σ_W but did NOT endure a stress increase from the first failure-time event. These blocks simply have their failure-time reduced by the time that passed prior to the start of the first failure-time event, $t_{f,new} = t_{f,old} - \Delta t$. In essence, this fourth group of blocks are unaware that an

event has occurred and are simply waiting for their failure time to arrive. Here $\Delta t = t_{f,min}$ from the first failure-time event.

After the assignment of failure-times, the aftershock-time counter is again advanced to the minimum failure time and the second failure-time event is initiated. Now $t = t_{f,min}^1 + t_{f,min}^2$, where the superscript identifies the event number. This process of assigning and adjusting failure times and locating the “seed” block is repeated until all blocks are at a stress below σ_W and thus have a failure time of $t_f = \infty$. This marks the end of the aftershock sequence.

To initiate another sequence of events, the loader-plate is advanced such that a single block reaches the static failure threshold, the aftershock time for this new sequence of events is reset to zero and the process is started over. We track the total aftershock time of the simulation run, which includes many loader-plate updates.

4.4 Simulation Results

In Fig. 4.3 we show a representative time-line of the event magnitudes for a single sequence. The loader-plate triggered event occurs at $t = 0$ in this plot. This time-line shows there is an ever increasing spacing (waiting-time) between events as time progresses, as well as a decay in event size following the largest event at $t \approx 1$. During each sequence of events there is only a single mainshock which we define to be the event of the largest area. Applying this definition leads by default to all events prior to the mainshock being foreshocks and all events after the mainshock being aftershocks.

For any particular set of parameters, the sequence of events following a loader plate are comprised of foreshocks, a mainshock and its subsequent aftershocks. Each loader plate update produces mainshocks that are roughly equal in area to the mainshock following the previous loader-plate update. These mainshocks by themselves do not obey a Gutenberg-Richter scaling relationship and therefore can be considered characteristic events. The magnitude (area) of the mainshocks are dependent on the system parameters, particularly the damage threshold σ_W . In a simulation run with many loader-plate updates, there are many characteristic events and aftershock sequences.

4.4.1 Power-law time-to-failure

The first failure-time function we test is the power-law function, Eq. (4.10). A frequency-magnitude (GR) scaling relationship for 100 aftershock sequences is plotted in Fig. 4.4. The char-

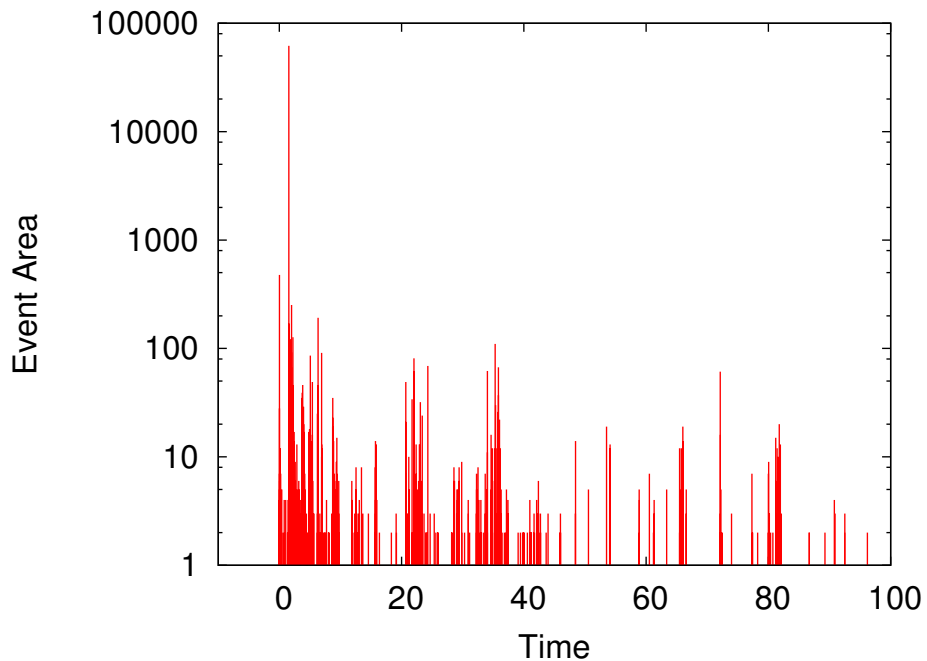


Figure 4.3: A plot of the magnitude of events vs time. The loader-plate update occurs at $t = 0$ and the mainshock of this sequence occurs a short time later. There are several foreshocks and a long sequence of aftershocks. The aftershocks continue past $t = 100$ but the sequence was truncated for illustrative purposes. The parameters of the model used to produce this time line are the same as those in Fig. 4.1, with $\frac{\sigma_W}{\sigma_F} = 0.97$ and $\rho = 2$.

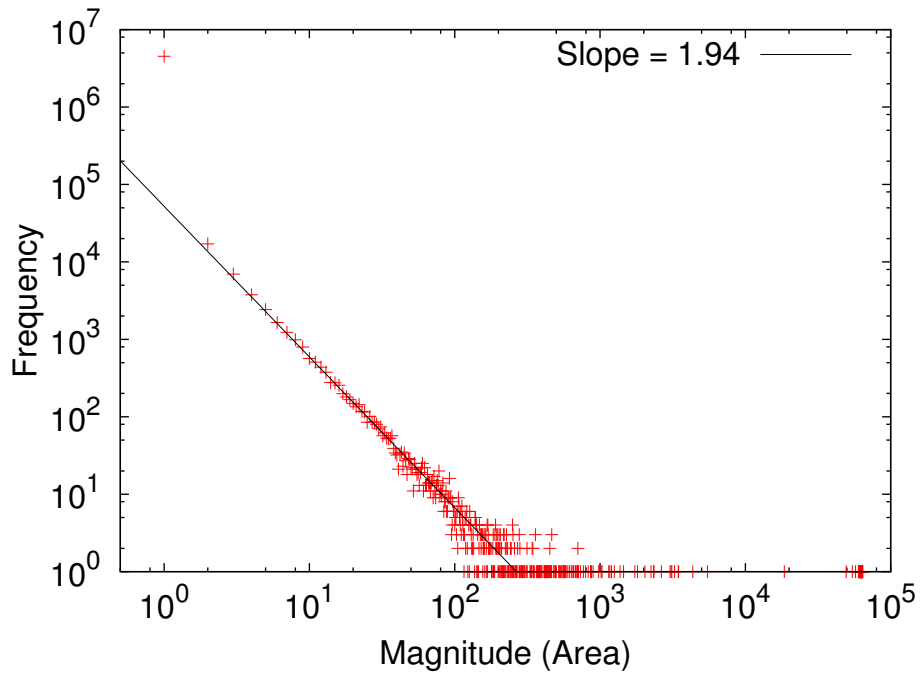


Figure 4.4: The Gutenberg-Richter scaling for all events during 75 loader-plate updates. This includes the foreshocks, mainshock and aftershocks of each cluster of events. The data is shown as a probability distribution rather than a cumulative distribution function. The corresponding CDF scaling exponent is 1 less than the PDF, which gives a b-value of roughly 0.94. This corresponds well with recorded data for earthquakes.

acteristic events (mainshocks) are also included in this plot. Any individual aftershock sequence displays GR scaling, but the stacked sequences produce a much cleaner distribution for determining the scaling exponent. Here the scaling exponent is $b' = 1.94$ as defined in Eq. (4.2). This distribution is a probability density function and so a corresponding cumulative distribution will have a scaling exponent of $b = b' - 1 = 0.94$. This b-value is on par with the observed scaling exponents for aftershocks in nature. It is important to note, however, that we are plotting event area rather than moment, which do not necessarily have a 1-to-1 correspondence. Additionally, there are two anomalies to the scaling relationship presented in Fig. 4.4. First there is an excess of data points at a large event area. This bump in the distribution corresponds to the characteristic events in each sequence. The second is the value of the events of area 1. These events correspond to blocks that slipped due to a failure-time, but do not slip far enough to start a cascade of slips in neighboring blocks. For the purposes of this model, we consider these events background noise and do not include them in any discussion of the properties of the aftershocks. In essence, these events can be considered too small to detect or since their slip distances are small, they can be considered creep events that did not produce noticeable energy release. Aftershocks have been shown to follow GR scaling and display Omori's law, so events that do not obey GR scaling will disrupt or change the scaling in the Omori's law plot.

Attention is now turned to the first property of aftershocks that the model is created to obey, namely Omori's Law. The rate of aftershocks in the model can be calculated by dividing the time after the mainshock into bins of fixed bin width τ_w , and counting the number of events that occur within each bin. The rate of events is then that number per bin width, $\frac{N}{\tau_w}$. For example, if the bin width corresponded to 1 day, and there were 20 events in the first bin, the rate of aftershocks would be 20 events/day for the first day. In this model, we consider only non-dimensional time, $\frac{t}{\tau_0}$, and thus the size of the bin width has no meaning other than there must be enough bins to distinguish the rate of events as time progresses. In Fig. 4.5, we plot the stacked rate of events that occur as a function of time for 75 sequences of events. This plot shows a scaling relationship for the rate of events occurring post mainshock with a scaling exponent of approximately $p = -1$. This scaling exponent is similar to Omori's law scaling exponents found in aftershock sequences in nature. In constructing this plot, we have ignored all events of size 1 as discussed earlier. We have tested this lower event size cutoff, by determining the rate of aftershock decay assuming only events of size greater than 2, 5, and 10 are relevant. The scaling exponent p remains constant within the numerical fitting error. This was expected since the Gutenberg-Richter scaling is satisfied down to events of size 2.

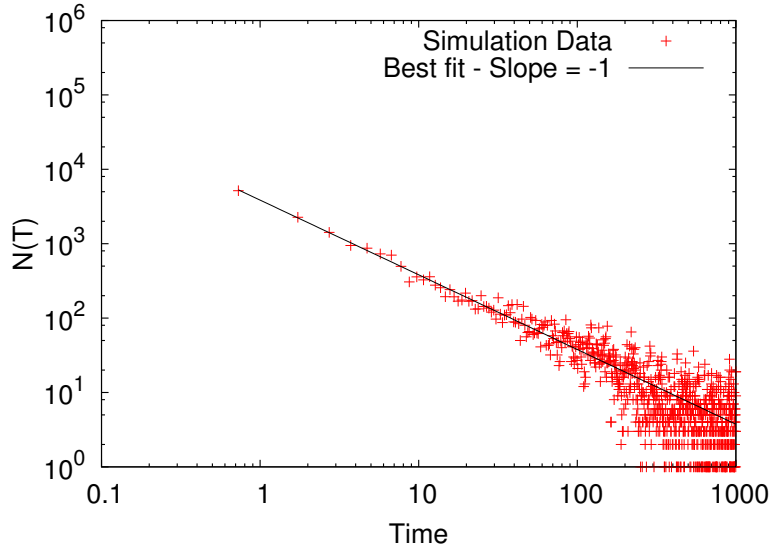


Figure 4.5: The number of events following the mainshock are binned and plotted. The bin width here is near 1 unit of time. The mainshock is defined as the largest event area in the sequence after 1 loader-plate update. The data is binned into 1000 equally spaced bins and fit to a power-law. This data is the sum of aftershocks following 75 loader-plate updates. The scaling exponent is $p \approx 1$, which corresponds well with observed values for Omori's law scaling in earthquakes.

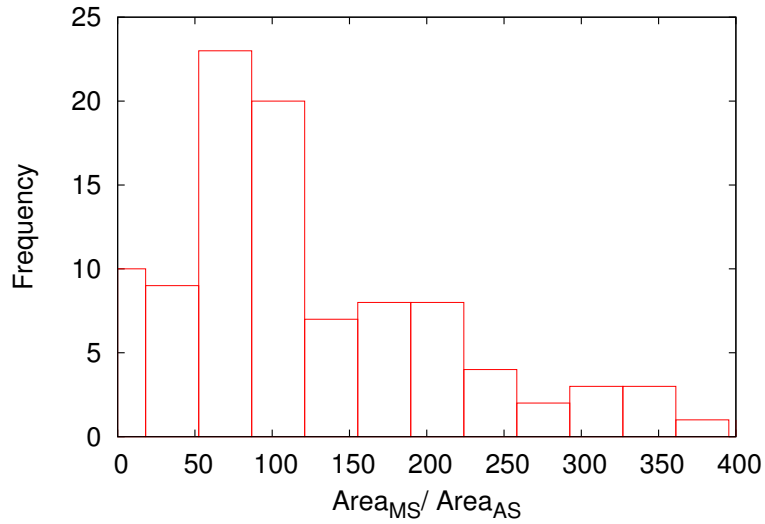


Figure 4.6: A histogram of the ratio of the area of the mainshock over the area of the largest aftershock is shown here. Bath's law suggests that this ratio should correspond to 1 magnitude unit on the Gutenberg-Richter scale.

In addition to Omori's law we test our aftershocks for the validity of Bath's law. We have calculated and binned the ratio of the area of the mainshock to the area of the largest aftershock $\frac{A_{MS}}{A_{AS}}$. Here we use A_{MS} to represent the area of the mainshock and A_{AS} for the area of the largest aftershock. The distribution of this ratio for the parameters used in Figs. 4.3 - 4.5 show a skewed distribution with a peak around 75. These ratios are fairly consistent but there is a considerable width to the distribution.

The behavior of the model is dependent on the simulation parameters which include: the coupling spring stiffness K_c , the maximum residual stress σ_R , the range of interaction r , the damage threshold σ_W and the failure-time exponent ρ . It is of interest to keep the parameters K_c , σ_R and r fixed such that the standard slider-block model produces the Gutenberg-Richter scaling as shown in Fig. 4.1. Thus the tuning parameters for this model are damage threshold σ_W and the failure-time function parameter, ρ . The Gutenberg-Richter distributions for event sizes in the time-to-failure model are minimally affected by changing $\frac{\sigma_W}{\sigma_F}$ from 0.97 – 0.995. The Omori's law rate of decay for aftershocks consistently displays power-law behavior over several orders of magnitude in time, but the scaling exponent p can vary from 0.5 – 1.5. In Fig. 4.7, we plot the various values of p for failure-time exponents $\rho = 1 – 4$ as a function of damage threshold. This plot shows that the scaling exponent p increases with the failure-time exponent ρ . The values of p vary with the damage threshold, with several different combinations of ρ and σ_W resulting in a p -value near 1. For the models presented here, both σ_F and σ_W are spatially constant. Fig. 4.7 suggests including randomness in the stress thresholds will also result in a power-law dependence for the rate of aftershock decay. This will also be a more physically realizable scenario.

4.4.2 Exponential time-to-failure

In addition to the power-law failure-time function, Eq. (4.10), we have also tested an exponential function of the stress given in Eq. (4.11). We test this function to compare the dependence of the rate of aftershocks that on the functional form of the failure-time function. It is of interest to determine how the shape of the failure-time function affects the emergence of Omori's law. Again, the maximum time-to-failure is normalized to 1 for blocks that fail at $\sigma = \sigma_W$.

We have run this exponential failure-time function for the same system parameters as reported in Figs. 4.3 - 4.6. The general result is that the Gutenberg-Richter scaling law remains for events greater than size 1, with a scaling exponent of $b' \approx 2$. There is not however, strong evidence that Omori's law is satisfied in general. Examples of Omori's law for a particular set of parameters

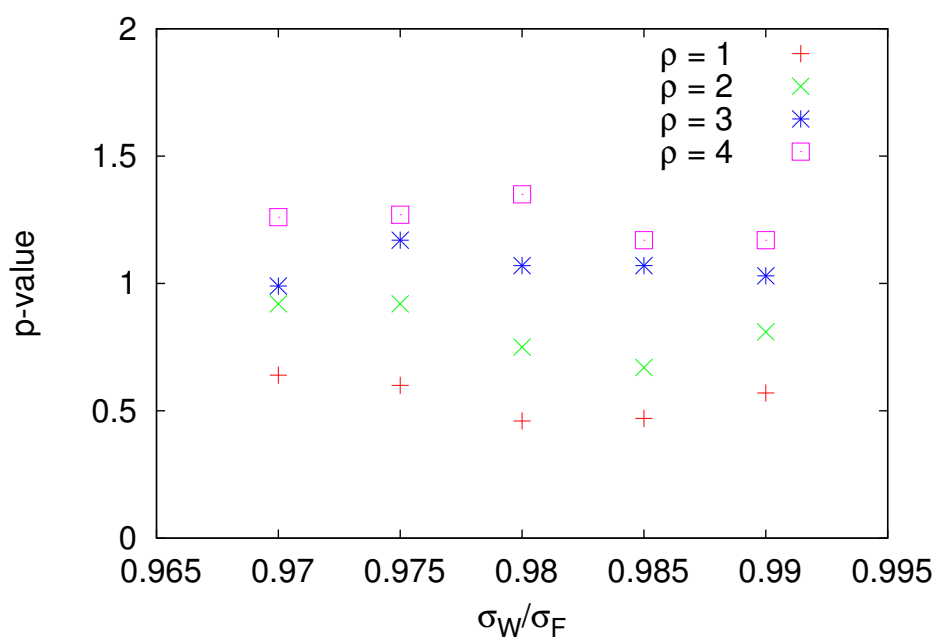


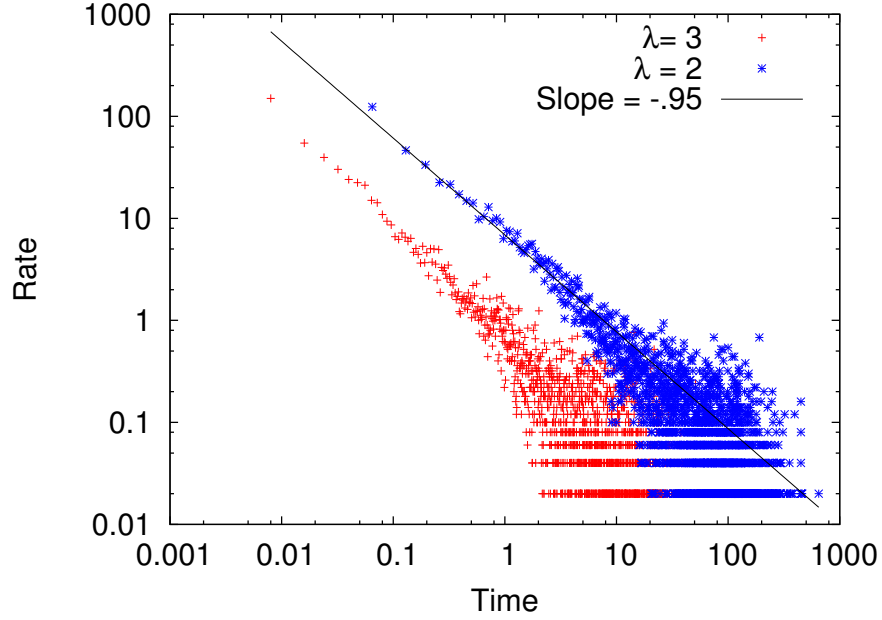
Figure 4.7: Various Omori's law scaling exponents, p -values, are plotted for failure-time exponents $\rho = 1 - 4$ as a function of the damage threshold. Each data point reported here is calculated ignoring events of size 1.

is shown in Fig. 4.8. Fig. 4.8(a) shows 2 simulation runs that display scaling behavior with a scaling exponent near 1. The parameters for these simulations are identical to those used in Fig. 4.1, with $\lambda = 2$ and 3 with $\frac{\sigma_W}{\sigma_F} = 0.97$. The corresponding Gutenberg-Richter plot for this simulation run has a scaling exponent of $b' = 1.94$. Fig. 4.8(b) shows two values of λ for $\frac{\sigma_W}{\sigma_F} = 0.98$. These simulation runs do not display a pronounced scaling behavior over several orders of magnitude. A power-law fit with a slope of $p = -0.53$ is shown for reference. The value of the damage threshold has significant impact on the resulting power-law behavior of the rate of aftershocks when using the exponential failure-time function. A power-law is recovered for smaller values of σ_W , while large values of σ_W yield a broken power-law as depicted in Fig. (4.8)b with a scaling exponent that is far from 1.0 This is in contrast to the power-law failure-time function that produces a power-law rate of aftershocks for all values of σ_W with varying scaling exponents.

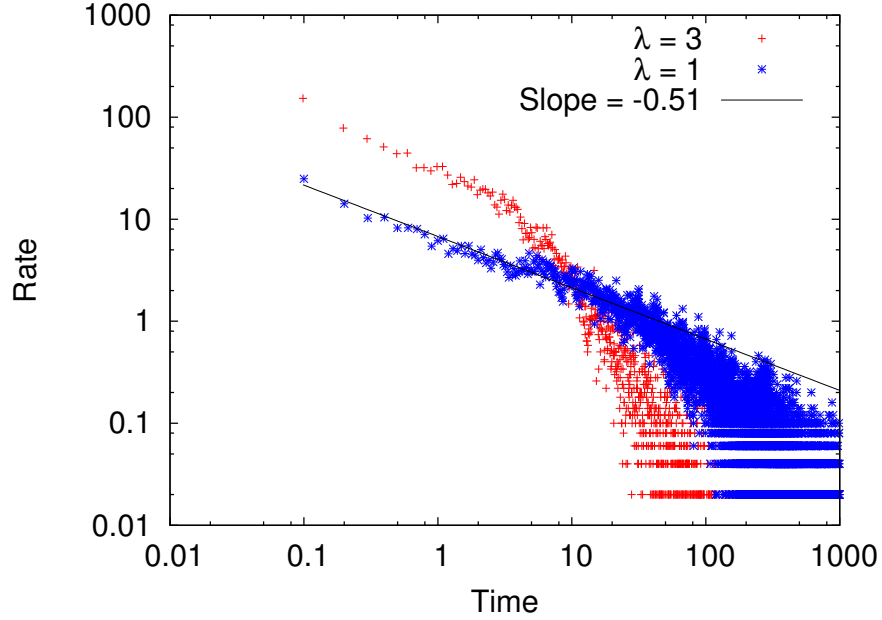
4.5 Discussion and Conclusions

In this paper we have proposed a modification to the standard slider-block model that promotes the occurrence of aftershocks. This modification represents the physics of stress fatigue and allows time-dependent failures at a stress below the static failure threshold σ_F . Three assumptions are necessary to build this model. These include: Aftershocks will initiate within the elastically loaded of the previous events, failure times are assigned only to blocks with stress in the range $\sigma_W < \sigma < \sigma_F$, and there are three time scales in this problem. In order from short to long these time scales are: the duration of an event, the waiting time between aftershocks, and the waiting time for the loader plate to trigger an event. This implies the duration of an event is negligible compared to the time-to-failure waiting time while the time-to-failure waiting time is much much shorter than the time between loader-plate initiated events. We have described the model dynamics for the CA slider-block model and the rules we have included to represent the time-dependent failure process.

A simple power-law time-to-failure function is proposed based on theoretical and experimental research and the model is run according to simple cellular automata rules. The resulting behavior shows that a time-to-failure feature can yield a Gutenberg-Richter scaling for event magnitudes, a rate of decay of aftershocks that obey's Omori's law, and compliance with Bath's law for the size of the largest aftershock. The results are compared against a second failure-time function, namely an exponential. The results are far better for the power-law dependence, in that the rate of aftershock decay shows a power-law dependence for a wide range of parameters, while the exponential failure-time function shows a power-law distribution only for a limited range in time



(a) Certain parameters produce scaling behavior. This plot shows the a p-value of approximately 1, for parameters $\lambda = 2$ and 3 with $\frac{\sigma_W}{\sigma_F} = 0.97$



(b) In other cases, for example $\frac{\sigma_W}{\sigma_F} = 0.98$, the scaling region for Omori's law is greatly reduced or not present. Here we show two cases that do not have a well-defined scaling region.

Figure 4.8: Rates of aftershocks for the model using an exponential failure-time function are plotted here. In certain cases there is a well-defined scaling region with a p -value near 1. In other cases the scaling region is significantly reduced in size or non-existent.

using a particular set of parameters. We can attribute this to the shape of the failure-time functions. As shown in Fig. (4.2), the shape of failure time function can vary significantly. The exponential function in Fig. (4.2) decays to nearly zero in a very short range of the stress and contributes to most events being triggered within a short time of the previous event and a much smaller number of events triggered at long waiting times. This contributes to the kink in the Omori's law plot for the exponential function in Fig. (4.8)b.

A comparable study of an earthquake model with time-dependent nucleation was carried out by Dieterich [13]. This study uses a simplified version of rate and state friction that includes both time-dependent fracture and a time-dependent healing process and produces a power-law rate of decay for aftershocks. Our model complements this study by focusing solely on the time-dependent fracture behavior to provide insight on the physical dependence that produces Omori's law. Our model shows that a time-to-failure mechanism can be responsible for the creation of aftershocks and in certain cases accurately depicts the inverse power-law decay rate for their occurrence. The time-to-failure method of triggering aftershocks proposed here, can be further tested in a large scale fault network simulator [25]. A model such as Virtual California generalizes the simple physics used here, namely, the uniform long range interactions and replaces them with Green's functions based on linear elastic continuum mechanics. In addition, these models transfer stress (and energy) from an earthquake to neighboring faults, which extends the elastically loaded region for aftershocks to occur and can allow aftershocks to spread in space and time.

4.6 References

- [1] R. Burridge and L. Knopoff. Model and theoretical seismicity. *Bull. Seismol. Soc. Am.*, 57: 341–371, 1967.
- [2] J. B. Rundle and D. D. Jackson. Numerical simulation of earthquake sequences. *Bull Seismol. Soc. Am.*, 67:1363–1377, 1977.
- [3] John B. Rundle and Stephen R. Brown. Origin of rate dependence in frictional sliding. *Journal of Statistical Physics*, 65:403–412, 1991.
- [4] J. M. Carlson and J. S. Langer. Mechanical model of an earthquake fault. *Phys. Rev. A*, 40: 6470–6484, 1989.
- [5] W. Klein, M. Anghel, C. D. Ferguson, J. B. Rundle, and J. S. Sa Martins. Statistical anal-

- ysis of a model for earthquake faults with long-range stress transfer. In J. B. Rundle, D. L. Turcotte, and W. Klein, editors, *Geocomplexity and the Physics of Earthquakes*, Geophysical Monograph 120, pages 43–71. American Geophysical Union, Washington D.C., 2000.
- [6] C. A. Serino, W. Klein, and J. B. Rundle. Cellular automaton model of damage. *Phys. Rev. E*, 81(1):016105, Jan 2010. doi: 10.1103/PhysRevE.81.016105.
 - [7] J. D. Gran, J. B. Rundle, D. L. Turcotte, J. R. Holliday, and W. Klein. A damage model based on failure threshold weakening. *Physica A*, 390:1269–1278, 2011.
 - [8] B. Gutenberg and C. F. Richter. *Seismicity of the Earth and Associated Phenomena*. Princeton University Press, Princeton, NJ, 1954.
 - [9] T. Utsu. A statistical study on the occurrence of aftershocks. *Geophys. Mag.*, 30:521–605, 1961.
 - [10] M. Båth. Lateral inhomogeneities in the upper mantle. *Tectonophysics*, 2:483–514, 1965.
 - [11] R. Shcherbakov, D. L. Turcotte, and J. B. Rundle. A generalized Omori’s law for earthquake aftershock decay. *Geophys. Res. Lett.*, 31(L11613), 2004. doi: 10.1029/2004GL019808.
 - [12] A. S. Helmstetter and D. Sornette. Båth’s law derived from the Gutenberg-Richter law and from aftershock properties. *Geophys. Res. Lett.*, 30(20):2069, 2003. doi: 10.1029/2003GL018186.
 - [13] J. Dieterich. Earthquake simulations with time-dependent nucleation and long-range interactions. *Nonlinear Proc. Geoph.*, 2:109–120, 1995.
 - [14] A. Ruina. Slip instability and state variable friction laws. *J. Geophys Res.*, 88(B12):10359–10370, 1983.
 - [15] J. R. Rice and A. L. Ruina. Stability of steady frictional slipping. *Journal of Applied Mechanics*, 50(2):343–349, 1983.
 - [16] J. A. Steketee. On volterra’s dislocations in a semi-infinite elastic medium. *Can. J. Phys.*, 36:192–205, 1958.
 - [17] E.F. Preston, J.S. Sa Martins, J.B. Rundle, M. Anghel, and W. Klein. Models of earthquake faults with long-range stress transfer. *Computing in Science Engineering*, 2(3):34 –41, 2000.

- [18] Junchao Xia, Harvey Gould, W. Klein, and J. B. Rundle. Near-mean-field behavior in the generalized burridge-knopoff earthquake model with variable-range stress transfer. *Phys. Rev. E*, 77(3):031132, 2008.
- [19] D. Amitrano and A. Helmstetter. Brittle creep, damage and time to failure in rocks. *J. Geophys. Res. B*, 111, 2006.
- [20] B. D. Coleman. Time dependence of mechanical breakdown in bundles of fibers. I. Constant total load. *J. Ap. Phys.*, 28:1058–1064, 1957.
- [21] W. A. Curtin, M. Pamel, and H. Scher. Time-dependent damage evolution and failure in materials. II. Simulations. *Phys. Rev. B*, 55:12051–12061, 1997.
- [22] W. I. Newman and S. L. Phoenix. Time-dependent fiber bundles with local load sharing. *Phys. Rev. E*, 63:021507, 2001.
- [23] S. L. Phoenix and W. I. Newman. Time-dependent fiber bundles with local load sharing. II. General Weibull fibers. *Phys. Rev. E*, 80:066115, 2009.
- [24] S. Das and C. H. Scholz. Theory of time-dependent rupture in the earth. *J. Geophys. Res.*, 86(B7):6039–6051, 1981.
- [25] P. B. Rundle, J. B. Rundle, K. F. Tiampo, A. Donnellan, and D. L. Turcotte. Virtual California: fault model, frictional parameters, applications. *Pure Ap. Geophys.*, 163:1819–1846, 2006.

Chapter 5

A numerical study of fracture nucleation

abstract

We discuss a general model for fracture nucleation and growth on the square lattice Z^2 . We determine the phase diagram and growth modes numerically under a variety of conditions, using a Metropolis algorithm. Distinct modes of fracture nucleation and propagation are seen under certain model parameters. Simulation experiments include a continuous slow loading, which demonstrates regions of elastic behavior and dependence on the loading rate, and instantaneous quenches of the applied load, yielding nucleation transitions near the spinodal. We also examine the behavior of the model under repulsive interactions and compare the resulting symmetry breaking transitions to the anti-ferromagnetic Ising model.

5.1 Introduction

Many experimental and numerical studies have been performed in order to understand the dynamics of material failure [1, 2, 3]. Material failure via fracture has often been modeled as a threshold process in which materials under load fail when a critical value of loading is reached(). Numerical studies have applied the foundations of statistical mechanics to the problem of material failure under tensile and shear stresses. These studies include comparing the fracture process to first and second order phase transitions [4, 5, 6]. Models of first order transitions have been proposed that include long range interactions, leading to conditions of metastable equilibrium and decay via nucleation and continuous ordering after quench. These same processes occur in many non-linear threshold systems in nature including, neural networks, financial markets, protein folding, traffic

flow, and failure of materials under load including sliding friction and earthquakes [7, 8, 9, 10, 11].

In the case of fracture of materials, the decay from metastability occurs by the nucleation of microcracks which coalesce to form a macroscopic fracture that propagates through the system. A thermodynamic approach was proposed using a one dimensional Monte Carlo simulation in which bonds occupy one of two states, intact or broken [12]. Here they found a critical crack length appears prior to rupture and the distribution of micro-cracks is approximately Boltzmann. It has also been shown that the slider-block model for shear failure, can be considered a nucleation process near the spinodal under the proper loading conditions [13].

To summarize our main result: We propose a 2-dimensional statistical mechanics model for fracture using a Monte Carlo simulation, which can be adapted to many systems in nature that display nucleation phase transitions. The dynamics of the model are controlled by the Metropolis algorithm and the system displays ergodic behavior while in a stable equilibrium. We define a free energy function that allows a single metastable “closed” state and a lower energy fractured state. Decay from metastability occurs via a nucleation process, where the rate of nucleation is dependent on the system parameters, i.e. temperature, external load, interaction amplitude and range of interaction. We use a generalized Cahn-Hilliard-Cook linear theory to describe the nucleation modes seen in the simulations. Specifically we have found under repulsive interactions, nucleation “droplets” of fracture appear and propagate similarly to “droplets” of spins in ferromagnetic Ising model. Our model also exhibits elastic behavior under slow-loading conditions and has a yield strength dependent on temperature. Nucleation times have been measured using intervention techniques as well as looking for a break in ergodicity with good agreement. When we impose repulsive interactions, we find the nucleation transition becomes a symmetry breaking transition similar to that seen in an antiferromagnetic Ising model [14, 15].. Here the final state has regions of positive offset organized into either “stripes” or “clumps”. We interpret our results in light of both tensile and shear applied loads.

5.2 Free Energy

We begin by defining a free energy functional for the offset field of the crack. We use a discrete version of the free energy motivated by a similar study [16] with the addition of a new term:

$$F(\zeta) = \sum_i \left(-p\zeta_i + \frac{1}{2} \sum_j G(i, j)\zeta_i\zeta_j + 2\gamma\{1 - \exp(-\zeta_i^2/a^2)\} + b\zeta_i^4 \right) \quad (5.1)$$

The first term is the energy associated with the external load, where p is the magnitude of the applied force. In our simulations p is uniform across the system and always positive. The second term represents the interaction between neighboring sites, where the interaction potential $G(i, j)$ can be a function of separation between sites i and j . For our simulation however, $G(i, j)$ is a constant, meaning sites a distance r away interact with the same strength G independent of r . The interaction coefficient G can be either positive or negative. A negative G amplifies the external load and represents typical fracture behavior while a positive G represents a repulsive-type interaction and will be discussed later. The exponential term is the binding energy due to the restoring force of the intermolecular bonds across the crack surface. Here γ is the strength of the cohesion and a is a lattice constant. The cohesion term contributes to the free energy only for small offset values, $\zeta \lesssim 3$. Any offset beyond this value can be considered fractured or broken. The final term is a stabilizing term which prevents an infinite run-away of the crack separation after nucleation occurs. If $b = 0$, the free energy is identical to free energy studied in 1D by Rundle and Klein [16]. We test our model under this condition to investigate the behavior in 2D. We also investigate our model using $b \neq 0$.

5.3 Cahn-Hilliard-Cook Theory

We now aim to rewrite our free energy to resemble the free energy studied by Dominguez et al. [15]. To do this we first Taylor expand our exponential cohesion term and coarse grain the free energy. We also make the correspondence:

$$\sum_j G(i, j) \zeta_i \zeta_j \rightarrow [R' \nabla \zeta(\mathbf{x}, t)]^2 \quad (5.2)$$

where R' is the range of interaction. See Klein et al. [5]. Our coarse grained free energy is then:

$$F[\zeta] = \int d\mathbf{x} \left\{ \frac{1}{2} [R' \nabla \zeta(\mathbf{x}, t)]^2 + \left(\frac{2\gamma}{a^2} \right) \zeta^2(\mathbf{x}, t) + \left(b - \frac{\gamma}{a^4} \right) \zeta^4(\mathbf{x}, t) - p\zeta(\mathbf{x}, t) \right\}. \quad (5.3)$$

We can further make the definitions:

$$\chi \equiv \left[4 \left(b - \frac{\gamma}{a^4} \right) \right]^{\frac{1}{4}} \quad (5.4)$$

and

$$\zeta \equiv \chi \hat{\zeta} \quad (5.5)$$

$$\epsilon \equiv \left(\frac{4\gamma}{\chi^2} \right) \quad (5.6)$$

$$R \equiv \frac{R'}{\chi} \quad (5.7)$$

$$p \equiv \frac{p}{\chi} \quad (5.8)$$

We can now write our free energy functional in the compact form:

$$F[\hat{\zeta}] = \int d\mathbf{x} \left\{ \frac{1}{2} [R' \nabla \hat{\zeta}(\mathbf{x}, t)]^2 + \frac{\epsilon}{2} \hat{\zeta}^2(\mathbf{x}, t) + \frac{1}{4} \hat{\zeta}^4(\mathbf{x}, t) - p \hat{\zeta}(\mathbf{x}, t) \right\}. \quad (5.9)$$

Note, in making these substitutions we must maintain the requirement that the coefficient of the highest order term of the free energy remain positive. This ensures the probability

$$P(\hat{\zeta}) = e^{-\beta F[\hat{\zeta}]} \quad (5.10)$$

where $\beta = T^{-1}$, remains finite for large $\hat{\zeta}$. To do this, we require that $b > \frac{\gamma}{a^2}$. This provides an upper limit on γ . All $\gamma < 0$ satisfy this condition. If b and γ are chosen such that χ^4 , as we have defined it, is negative, we must carry our expansion to the sixth-order term and include

$$\mathcal{O}(6) = \left(\frac{\gamma}{3a^6} \right) \zeta^6(\mathbf{x}, t) \quad (5.11)$$

in our initial Taylor expansion and redefine our variables accordingly.

Eq. (5.9) is now identical to the form of the Landau-Ginzburg free energy studied in Dominguez et al. [15]. We can now follow their prescription for determining the Fourier growth modes. First we can define a Langevin equation:

$$\frac{\partial \hat{\zeta}(\mathbf{x}, t)}{\partial t} = -M \left(\frac{\delta F[\hat{\zeta}]}{\delta \hat{\zeta}} \right) + \sqrt{2MT} \eta(\mathbf{x}, t) \quad (5.12)$$

where T is the temperature and M is a mobility that we assume to be constant. If we retain only up to quadratic terms in Eq. (5.9), and write the free energy in the Fourier transform domain we find:

$$\tilde{F}[\phi] = \int d\mathbf{k} \left\{ -\frac{1}{2} R^2 k^2 |\phi(\mathbf{k}, t)|^2 + \frac{\epsilon}{2} |\phi(\mathbf{k}, t)|^2 - p \phi(\mathbf{k}, t) \right\} \quad (5.13)$$

It can be shown (see [15]) that Eq. (5.13) can be diagonalized, and that the most unstable k -mode has an eigenvalue:

$$\lambda = -M(R^2 k^2 - |\epsilon|) \quad (5.14)$$

Thus the growth rate of the various modes depends not only on the term in the Free Energy multiplying γ but also on the term multiplying b . Following Dominguez et al. [15], if we define the structure factor:

$$S(\mathbf{k}, t) = \left\langle \hat{\zeta}(\mathbf{k}, t) \hat{\zeta}(-\mathbf{k}, t) \right\rangle / V \quad (5.15)$$

where V is volume. It is found that:

$$S(\mathbf{k}, t) = e^{2\lambda t} \left[S(\mathbf{k}, t=0) + \frac{M}{\beta\lambda} \right] - \frac{M}{\beta\lambda} \quad (5.16)$$

So the various Fourier modes here evolve independently. These equations describe the linear Cahn-Hilliard-Cook theory for our free energy which describe the evolution of the system from an unstable stationary state. Dominguez et al. [15] have taken into account the possibility of an unstable background state that depends on time as the order parameter evolves. The order parameter in this case can be written as:

$$\hat{\zeta}(\mathbf{x}, t) = \hat{\zeta}_b(\mathbf{x}, t) + R^{-d/2} \varphi(\mathbf{x}, t) \quad (5.17)$$

where $\hat{\zeta}_b(\mathbf{x}, t)$ is the evolution of the background state, and $\varphi(\mathbf{x}, t)$ is the fluctuation of the system about that point. The evolution of the order parameter can be written as the sum of the evolution of the background and the fluctuations. These are described by:

$$\frac{\partial \hat{\zeta}_b(\mathbf{x}, t)}{\partial t} = -M \left(\frac{\delta F[\hat{\zeta}]}{\delta \hat{\zeta}} \right) + \sqrt{2MT} \eta(\mathbf{x}, t) \quad (5.18)$$

which is identical to the original CHC theory described with Eq. (5.12), and

$$\frac{\partial \varphi(\mathbf{x}, t)}{\partial t} = \int d\mathbf{x}' \frac{\delta \Phi[\hat{\zeta}, \mathbf{x}]}{\delta \varphi(\mathbf{x}', t)} \Bigg|_{\hat{\zeta}=\hat{\zeta}_b} \varphi(\mathbf{x}, t) + \eta(\mathbf{x}, t) \quad (5.19)$$

which itself depends on the background state. This additional consideration leads to the distinction of two unique growth modes in the nucleation process. As defined in [15], stage 1 growth describes the system when the unstable state of the free energy is changing in time, and stage 2 describes the evolution from a fixed unstable state. The occurrence of stage 1 and 2 depend on the type of interaction, whether they be ferromagnetic (attractive) or antiferromagnetic (repulsive). Repulsive interactions can lead to solutions that exhibit both stage 1 and stage 2 kinetics and result in symmetry

breaking phase transitions. In the anti-ferromagnetic Ising model, for example, spin modes are seen in which disordered systems can give way to spatial patterns which can be described as either “clumps” or “stripes” of unidirectional spin modes [15].

In our fracture mode attractive interactions ($G < 0$) are analogous of an off-critical quench in the ferromagnetic Ising model, is described entirely by stage 2 kinetics. Under repulsive interactions ($G > 0$) our model exhibits symmetry breaking phase transitions which evolve in stage 1 and stage 2 kinetics similar to those seen in the anti-ferromagnetic Ising model in an off-critical quench. We test our model using a zero and non-zero coefficient b for the quartic term in Eq. (5.1) with both positive and negative interaction coefficients.

5.4 Simulation Dynamics

Simulations are run on a square 2D lattice plane with linear dimension L and periodic boundary conditions. The offset of each site is allowed to grow (fracture) and contract (heal) in the vertical (z) direction. We allow long range interactions in which a site interacts with all sites within a square neighborhood centered that site. The interaction region has a length $2r + 1$ on a side, where r is the interaction range. The total number of interacting neighbors is $q = (2r + 1)^2 - 1$. We use Monte Carlo dynamics, where lattice sites are sampled at random and the selected site will potentially grow or heal by a fixed, but small, $\delta\zeta$, with a 50% probability. We then compute the associated change in energy of the system due to the proposed change in offset according to the free energy in Eq. (5.1) and follow the standard Metropolis algorithm for acceptance. Time is measured in Monte Carlo steps (MCS) per unit site. A single MCS is defined to be when $N = L * L$ sites have been sampled.

5.4.1 Ergodicity

We tested the application of the Metropolis algorithm by verifying the system is ergodic when in equilibrium. Ergodicity is measured using a metric developed by Thrimulai and Mountain [17, 18]. This TM metric has been previously applied to fracture studies including slider-block models [13, 19] and natural fault systems [20, 21]. Originally formulated using the energies of individual particles in supercooled and glassy states of binary allows, we reconstruct the TM metric using the observable quantity defined for each lattice site, namely the crack offset, ζ . The TM metric is then:

$$\Omega(t) = \frac{1}{N} \sum_i [\bar{\zeta}_i(t) - \langle \bar{\zeta}(t) \rangle]^2 \quad (5.20)$$

where N is the number of sites in the lattice, and the quantities $\bar{\zeta}_i(t)$ and $\langle \bar{\zeta}(t) \rangle$ are given by

$$\bar{\zeta}_i(t) = \frac{1}{t} \int_0^t dt' \zeta_i(t') \quad (5.21)$$

and

$$\langle \bar{\zeta}(t) \rangle = \frac{1}{N} \sum_i \bar{\zeta}_i(t). \quad (5.22)$$

where t is measured in MCS.

If the system is effectively ergodic at long times, the TM metric decreases in time as, $\Omega(t) = \frac{D_e}{t}$ [18], where D_e is a diffusion constant related to the rate at which the phase space is explored. Since we are primarily concerned with the effective ergodicity of our model, we plot the inverse of the TM metric $1/\Omega(t)$ and look for a linearly increasing trend. The inverse TM metric is plotted in Figs. 5.3 along with the average offset during a nucleation transition. We expect the system to display ergodic properties when residing in a meta-stable or stable state. Since fracture is initiated by nucleation which is a non-ergodic process, any simulation resulting in a fracture will eventually break ergodicity and the inverse TM metric will show this by deviating from its linear trend.

5.5 Simulation Results I: $G < 0$

Fracture in our model occurs via the decay from a metastable state. As the applied load increases, the energy barrier the system must overcome is lowered and thus the nucleation rate is increased. Eventually the load is increased to a value where the energy barrier vanishes. This is the limit of metastability in the model, or the spinodal value of the applied load. A nucleation phase transition occurs only for p below the spinodal load, $p < p_{sp}$. The phase diagram for our model with $G < 0$ is shown in Fig. 5.1. We show the load vs interaction amplitude phase space, where qG which is the total interaction amplitude due to all interacting neighbors q . There is a lower limit on the interaction coefficient where the spinodal line intersects the $p = 0$ axis. If G is below this limit, the contribution of the interaction term to the free energy dominates the contribution from the cohesion term and no metastable well exists for all $p > 0$. We determined the location of the spinodal line numerically setting 1st and 2nd derivatives to zero and solving for p as a function of qG . Within the phase diagram, region I is the primary region of interest and represents systems

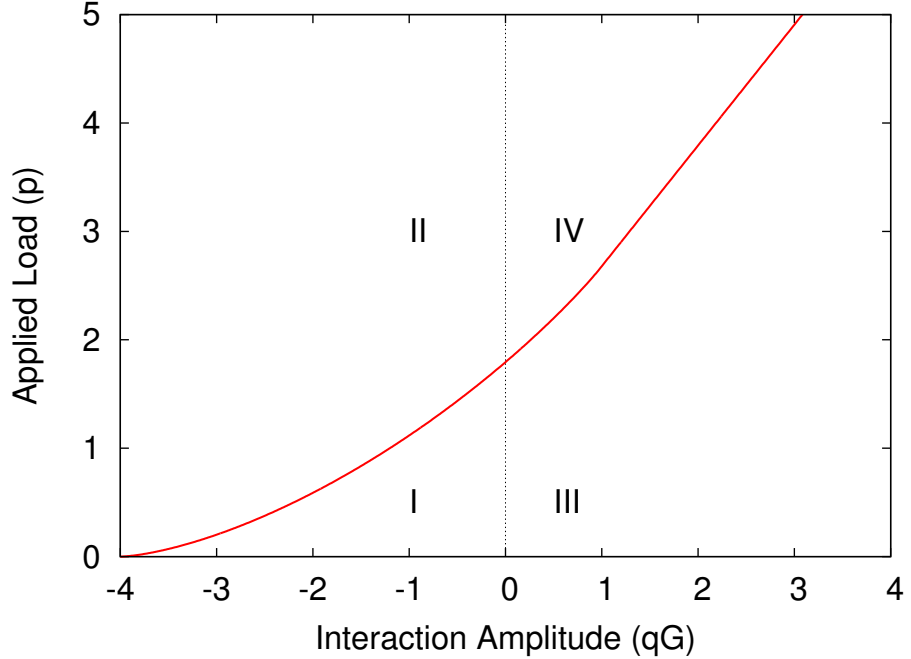


Figure 5.1: The phase diagram for our model is shown for $b = 0$. We include here both positive and negative interactions. There are four regions to the phase space. Region I has an applied load smaller than the spinodal value p_{sp} and allows fracture to occur via nucleation. Region II has an applied load larger than the spinodal value and thus the free energy has no metastable state. Nucleation does not occur in Region II. If $G < -4$, the free energy curve has no metastable state for all $p > 0$. Regions III and IV have temperature dependent symmetry breaking phase transitions that result in a lattice structure of sites with positive offset. This is discussed in Sec. 5.6.

which allow a meta-stable ‘‘closed’’ state and decay via nucleation to a lower energy fractured state. Region II is beyond the spinodal where there is only one well in the free energy and the crack offset will grow for any temperature without nucleation or the coalescence of microcracks to initiate a fracture. Regions III and IV will be discussed in Sec. 5.6

We focus our attention on region I in Fig. 5.1, $G < 0$ and $p < p_{sp}$, where meta-stable states exist prior to fracture. For these systems, transitions to the lower energy fractured state occur through a nucleation process initiated by thermal equilibrium fluctuations. The amplitude and frequency of fluctuations is controlled by the temperature. For any non-zero temperature there is a finite lifetime for the system to reside in the meta-stable state, although it can be extremely long.

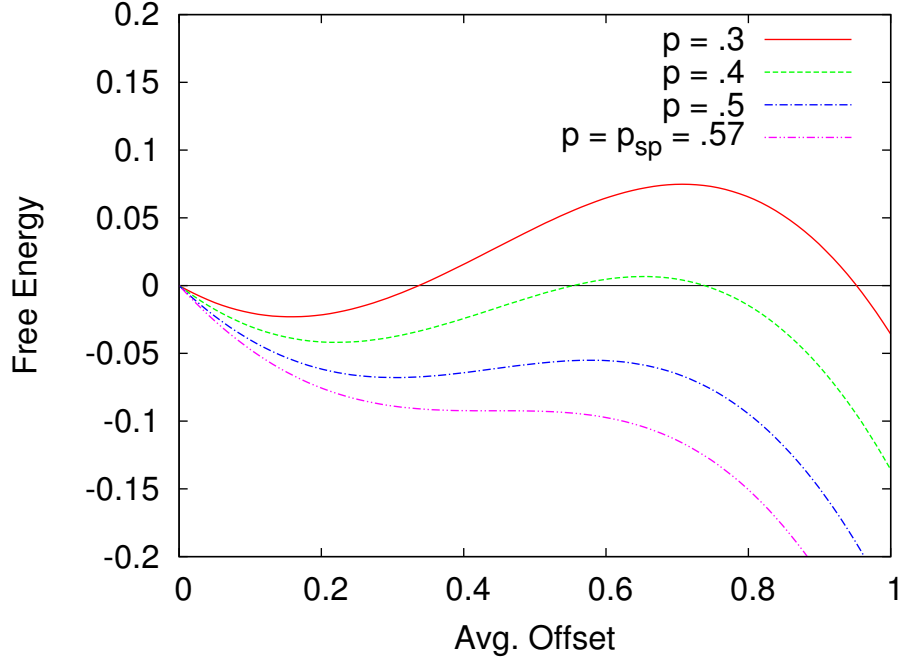


Figure 5.2: The free energy plot illustrates that as p is increased the metastable well vanishes leaving a transition to the lower energy state without nucleation. Nucleation from the metastable well leads to a runaway fracture state.

5.5.1 Runaway fracture nucleation, $b = 0$

In Fig. 5.2 we plot the free energy for various values of the load p approaching the spinodal value p_{sp} with the coefficient of the quartic term equal to zero. Using $b = 0$ we can verify the results originally published in [16] using 2D simulations, as compared with the original work done in 1D. The free energy has a single metastable well for applied loads below the spinodal value. The free energy for large offset goes to negative infinity, so any system that leaves the metastable state for a lower energy state at a larger offset will continue to grow indefinitely. This is a runaway fracture model. The application of this model is to the early time dynamics of the rupture process.

$$F(\bar{\zeta}) = -p\bar{\zeta} + \frac{1}{2}G\bar{\zeta}^2 + 2\gamma\{1 - \exp(-\bar{\zeta}^2)\} + b\bar{\zeta}^4 \quad (5.23)$$

Quench Experiment

We examine the nucleation transition of our model by quenching from a small applied load, where the lifetime of the meta-stable equilibrium $\rightarrow \infty$, to a load near but less than the spinodal value p_{sp} where the lifetime of the meta-stable state is small but non-zero. In Fig. 5.3, we plot the average offset of the system during a nucleation process vs time with “crosses” as well the inverse TM metric with “x’s”, corresponding to the same fracture along with two intervention measurements we will discuss below. After the quench is applied, the system quickly transitions from the small initial offset to the meta-stable offset. The system remains at this constant offset, deviating by only minor fluctuations until nucleation occurs and the system jumps to the lower energy fractured state. The runaway fracture propagation occurs roughly around 30,000 MCS. The inverse of the TM metric shows a linear trend from $t = 10000$ to approximately $t = 25500$, this is the duration the system resides in the meta-stable state. As noted above, this linear trend implies ergodic behavior while the break in ergodicity is an indication that nucleation has begun. The lifetimes of the meta-stable equilibrium and the fracture pattern of the nucleation transition depend on the range of interaction r , the strength of the interactions, G and the proximity of the applied load to the spinodal.

The nucleation time is determined using two independent methods and the results are compared. First, we use the intervention technique developed to aid the understanding of perturbations on nucleating droplets near the spinodal and applied to an Ising type model by Monette et al. [22]. The intervention procedure is as follows: we pick a time (MCS) where we believe nucleation has occurred and reset the random number generator used in the MC simulations. If the system proceeds to catastrophic failure at approximately the same time as with the original sequence of random numbers, the system is said to have nucleated prior to the time we chose. This is because after nucleation has occurred, the sequence of random numbers is somewhat irrelevant. The nucleating “droplet” has already formed and the fracture is in a propagation mode which dominates the behavior of the system. If, however, the lifetime of the metastable state is greatly increased after we reset the random number generator, nucleation has not yet occurred at the time intervention took place. Again this is because the fluctuations that cause the nucleating “droplet” to appear are dependent on the sequence of random numbers.

In Fig. 5.3, we also plot the average offset vs time (MCS) for the same simulation after interventions. The “crosses” represent the original run while the average offsets for two intervention times, 25000 and 26000 are plotted with “asterisks” and “boxes” respectively. From the plot, inter-

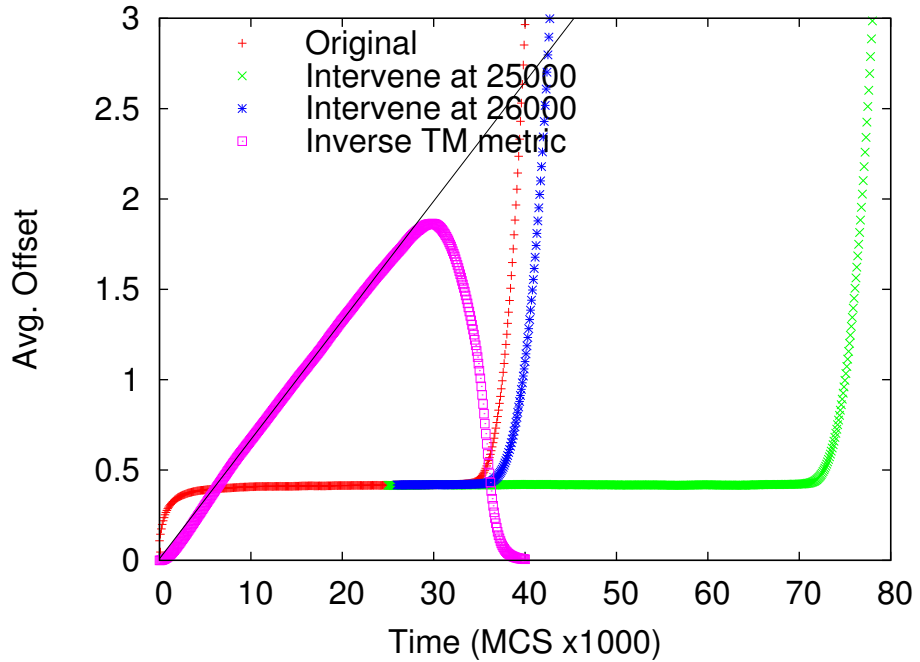


Figure 5.3: The average offset for a simulation is plotted against MCS with “crosses”. Nucleation occurs and the system transitions to the lower energy state at a larger offset. The inverse TM metric is plotted with “x’s” for the same simulation. The linear trend of the TM metric indicates the system is ergodic while in the metastable state, ergodicity is broken when nucleation begins. Here we also plot the average offset vs time for two nucleation transitions after intervention has occurred with “boxes” and “asterisks”. Intervention prior to nucleation at $t = 25000$ delays nucleation substantially, while intervention post nucleation at $t = 26000$ hardly deviates the failure time. Thus we can say at approximately $t = 25500$, nucleation occurs and catastrophic failure ensues. The intervention technique agrees with time of the break in ergodicity.

vention at 25000 greatly increases the lifetime of the metastable state, while intervention at 26000 seems to have little effect on the system. These interventions were repeated multiple times with similar results. We, therefore, can conclude that nucleation has occurred between these two times at approximately 25500. As noted above, ergodicity breaks down as the inverse TM metric deviates from a linear trend, which in this simulation occurs near MCS $t = 25500$. This is consistent with our intervention results for nucleation times and previous studies that show damage and fracture are inherently non-ergodic processes [23, 19]. It is also of interest to note that the nucleation time occurs prior to the jump in the average offset of the system, indicating that nucleation is a restructuring process of the offset field and occurs prior to the macroscopic formation and propagation of the fracture.

The fracture process we have described occurs via the formation of fracture “droplets” which propagate through the system. The number and size of these nucleating “droplets” is controlled by p , G and the range of interaction r . In Fig. 5.4 we show a representative fracture propagation process for a negative interaction coefficient G using short and long range interactions. The interaction amplitude is $qG = -2$ and $p - p_{sp} = .02$. Here we show time progressing to the right, the first row (figures a-c) is short range interactions $r = 1$. This fracture has many nucleation sites that propagate with well defined edges and grow independently of each other until coalescence occurs. In the second row (figures d-f), we show the same parameters, but increasing the range of interaction to $r = 8$. Here the short wavelength fluctuations are damped and the resulting fracture nucleation occurs at just one site and the fracture propagates in a circular fashion across the surface. This rupture has a process zone surrounding the main fracture that proceeds the growth of the offset field.

Linear Elastic Behavior

In addition to load quenching experiments, we have tested our model under slow-loading conditions. We run the simulations similar to those above but after each MCS we increase the applied load by a small constant amount, δp . Under these conditions our model exhibits elastic behavior for applied loads below the yield strength. In addition, as the temperature of the system is lowered towards zero, the elastic region of the stress-strain (applied load vs avg. offset) curve becomes linear. If the loading rate is too high compared to the step-size for the growth of the offset, the dynamics of the model do not allow the system to reach its meta-stable well before the location of the well moves due to the increasing load. In this regard we focus on loading rates slow-

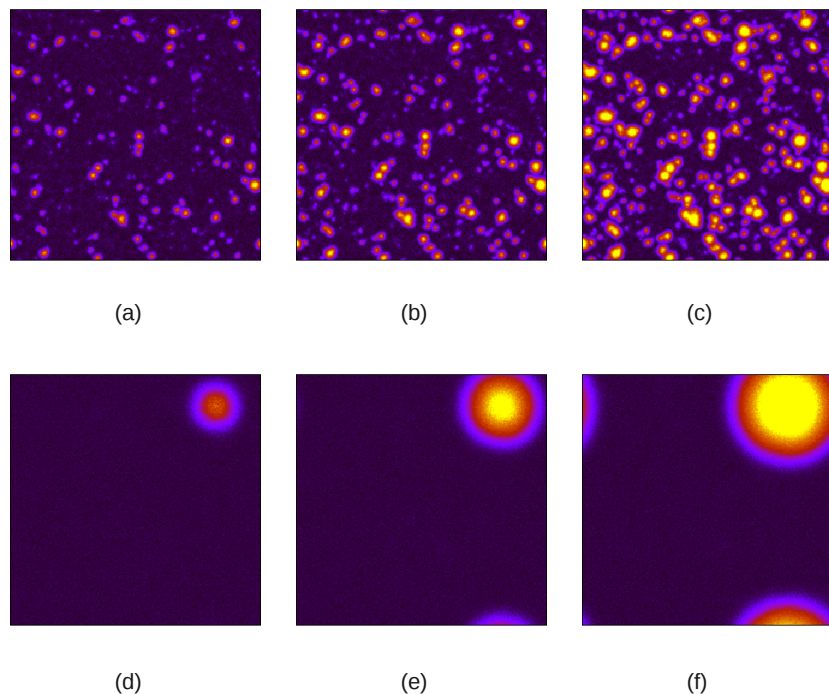


Figure 5.4: Here we plot the nucleating fracture for 3 different scenarios, where time progress to right. The top line we show, $r = 1$ and $G < 0$. The second line is $r = 8$, $G < 0$. The third line shows $r = 8$ and $G > 0$ and shows the lattice structure nucleation pattern that occurs for positive interaction coefficients.

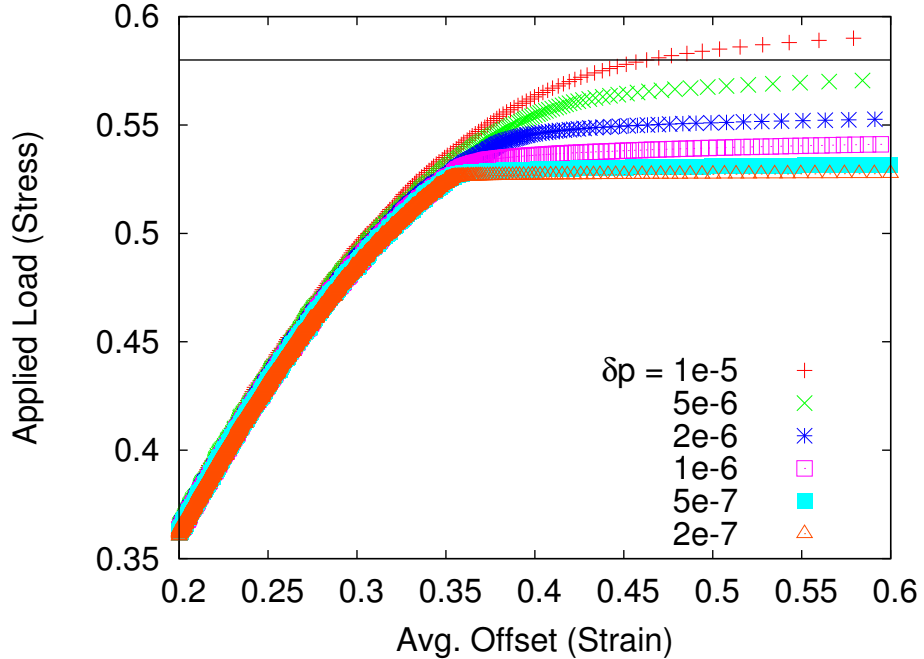


Figure 5.5: The linear elastic behavior of the model is shown here. The applied load is stress on the system and the average offset of the lattice is the strain. As the loading rate δp is reduced the system fails at a smaller applied load. The horizontal line is the value of stress beyond which there is no metastable well. The parameters used here are $G = -2$, $\gamma = 1$ and $b = .05$.

enough that the system does not reach the spinodal stress prior to rupture. As the loading rate is decreased the fracture occurs at lower applied loads and the damage prior to fracture is minimized. This linear elastic behavior is a reflection of the linear dependence of the free energy on the load.

In Fig. 5.5, we plot a stress-strain curve for our model under several loading rates. We mark the limit of applied stress where there is no longer a meta-stable well for reference. A loading rate of $\delta p = 1e - 5$ is too large for this system. All curves display a linear trend as the stress is increased towards the failure stress. The abrupt failure of the system occurs at lower stress thresholds when the loading rate is decreased due to the longer amount of time allowed for nucleation to occur. As the loading rate approaches zero the failure stress will approach the yield strength of our model. This test illustrates that although our model was built using statistical methodologies it retains important material properties such as linear elasticity.

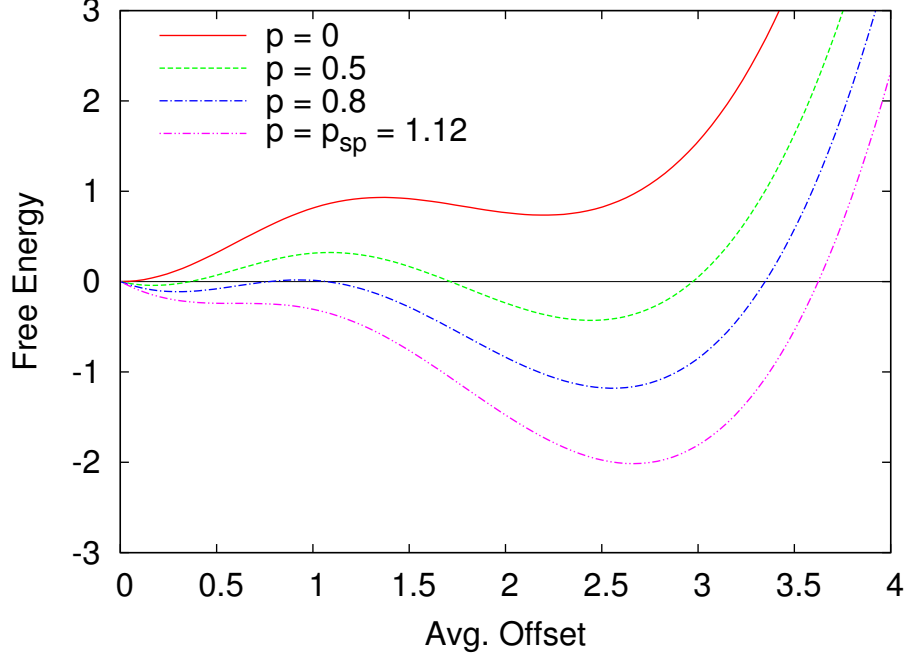


Figure 5.6: The free energy plot illustrates that as p is increased the metastable well vanishes leaving a transition to the lower energy state without nucleation. In the phase diagram Region I which allow a metastable state is separated from Region II which does not by the spinodal line.

5.5.2 Nucleation transition to a stable fractured state, $b \neq 0$

We now turn our attention to the inclusion of the quartic term in the free energy Eq. (5.1). We use a small value of b , so that this term provides its main contribution to the free energy at large ζ . In a similar fashion to Fig. 5.2, we plot the free energy, Eq. (5.23), with a positive b in Fig. 5.6. The parameters used in this plot are $G = -1$, $\gamma = 1$ and $b = .05$. Here we show that there is a second well in the free energy curve which transitions from metastable to stable as p is increased. The purpose of including this term is to prevent the runaway fracture that occurs with $b = 0$.

In Fig. 5.7 we plot the average offset vs time (MCS) for the load quench experiment described above and the inverse TM metric for the same simulation. Using the break in ergodicity as an approximate nucleation time indicates that nucleation occurs much earlier in this model as compared with the runaway fracture model. There is an extended period of time after nucleation occurs before the fracture propagates through the system. Once the system reaches the stable fracture state, the inverse TM metric once again shows a linear trend indicating ergodicity in the stable state. The structural pattern for fracture propagation also differs to that of the runaway model. Since there is

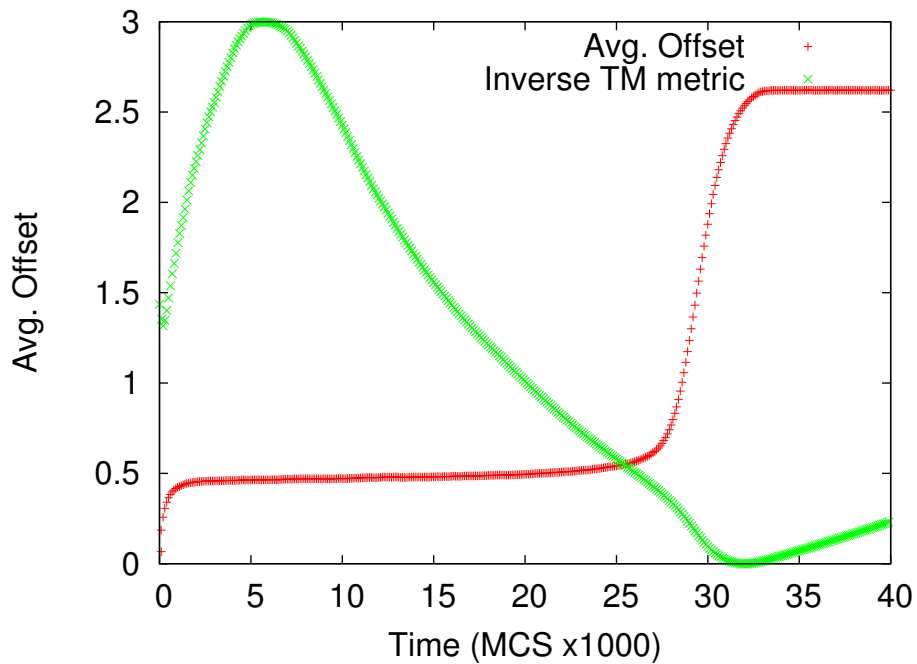


Figure 5.7: The average offset for a simulation is plotted against time (MCS) with “crosses”. The initial state of the system is zero offset and quickly moves into the meta-stable region. After sitting in the meta-stable state for a period of time, nucleation occurs and the system transitions to the lower energy state at a larger offset. The inverse TM metric is plotted with “x’s” for the same simulation.

essentially an upper limit on the growth of the offset for each site, the “droplets” of fracture do not remain circular for the entirety of the fracture process. The propagating fracture rather begins circular in shape but as it reaches the boundaries of the system, the fracture begins a filling out process similar to that seen in sliderblock models and fiber-bundle models [24].

5.6 Simulation Results II: $G > 0$

We next examine the model under repulsive interactions, i.e., $G > 0$. The interaction term now works against the applied load term and lowers the energy when the offset of sites shrink (heal). This repulsive interaction is analogous to the anti-ferromagnetic Ising model, in which spins prefer to point in the opposite direction of its neighbors. Simulations are run using the instantaneous load quenching experiment. Similar to when the “attractive” or positive interactions are in effect, the behavior of the system can be controlled with the applied load and temperature. For appropriately chosen values of the applied load we find symmetry breaking phase transitions can occur. We first report the symmetry breaking phase transitions with $b = 0$ and then with $b \neq 0$. When $b \neq 0$ The final stable state of the these transitions can be described as regions of positive offset confined to either “clumps” or “stripes”. These clumps and stripes are periodic in space and have previously been seen in the antiferromagnetic Ising model with long range interactions [15, 14].

5.6.1 Originally proposed free energy: $b = 0$

Similar to the attractive interations there is a threshold of the load p . Above this threshold, a temperature dependent phase transition occurs which results in a symmetry breaking evolution of the offset field. Below the threshold, the system resides in non-zero fixed offset state for all temperature. These phases are shown in Fig. 5.1 as regions III and IV. The free energy in Region III has only a single globally stable state at a uniform positive offset for all p . Region IV is where the symmetry breaking transition occurs. A representative evolution of the this transition is shown in 6 snapshots in Fig. 5.8. The initial deviation of the system from a uniform offset field, is by the formation of stripes of positive offset. These stripes are not energetically favorable and they decay in to clumps and eventually into a single site lattice arrangement. This behavior occurs for all parameters within Region IV of the phase diagram, Fig. 5.1.

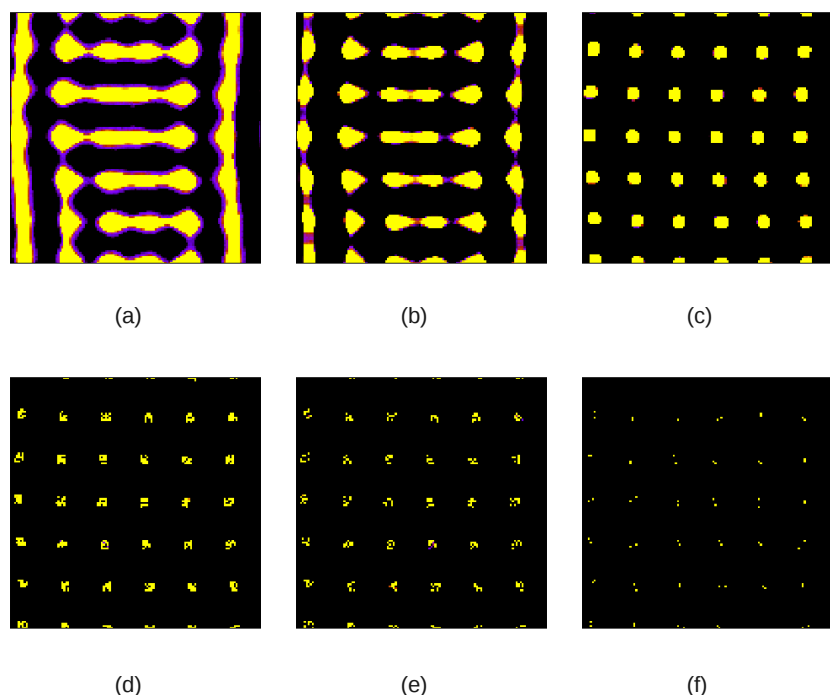


Figure 5.8: Here we see the time evolution of the symmetry breaking phase transition for $b = 0$ with repulsive interactions. The initial decay from a uniform offset field, shows the formations of stripes. These stripes decay into clumps and eventually the system stabilizes in an isolated site lattice structure.

5.6.2 Modified free energy: $b \neq 0$

In Fig. 5.9 we plot an approximate phase diagram for the emergence of stripes and clumps with a small coefficient of the quartic term $b = 1e - 4$. The cohesion coefficient remains $\gamma = 1$. Under these conditions the correct expansion of the exponential term in the free energy must be carried to at least the sixth-order term.

The cohesion term in this model acts as a prohibiting factor in the formation of stripes or clumps. If the load p and interaction amplitude G are small, such that the average offset of system remains in the region where the cohesion term contributes substantially to the free energy, stripes and clumps do not form and the system remains in a uniform offset state. For a larger interaction coefficient and applied load, the effect of the cohesion term is reduced. Sites begin to overcome an energy barrier and move to a larger offset stable state. These sites do not form any coherent structure but rather form random clusters of sites, analogous to a percolation lattice at low occupation probability. See Fig. 5.10(a). If p is increased further, the first symmetry breaking transition is allowed and clumps of positive offset form. See Fig. 5.10(b). As p is increased further still, the system reaches the phase boundary of clumps and stripes. Near this boundary the system initially forms stripes from the initial conditions of a uniform offset, but the stripes are not energetically favorable and decay into clumps. These clumps are sometimes elongated in the direction of the stripes or form partial stripes. See Fig. 5.10(c-e). Once the phase boundary is crossed by increasing p further, the stripes become the energetically favored state and remain after formation. See Fig. 5.10(f). And finally as p becomes very large, the applied load term dominates the free energy and pulls all sites to a uniform offset once again. In Fig. 5.10 we show the structure of the final stable state for increasing the load as described above. The interaction amplitude is set to $G = 3$, $b = 1e - 4$ and $\gamma = 1$. We increase the applied load from $p = 3.5$ to $p = 20$.

As expected the value of b contributes in determining the final structure of the system, whether it be a stripes, clumps or a stable uniform offset. As the magnitude of b increases, while the other parameters remain fixed, the stable structure of the system changes from clumps to stripes to a uniform offset where there is no spatial symmetry breaking.

The additional quartic term in the free energy is critical for the stability of the periodic structures in this phase transition. This is due to the fact that we allow a zero offset, $\zeta = 0$, as a possible state for each site. If any site has a zero offset the contribution to the free energy from this site interacting with neighboring sites goes to zero. Setting $b = 0$ does not prohibit the initial formation of stripes or clumps but in all cases where these structures emerge the system eventually

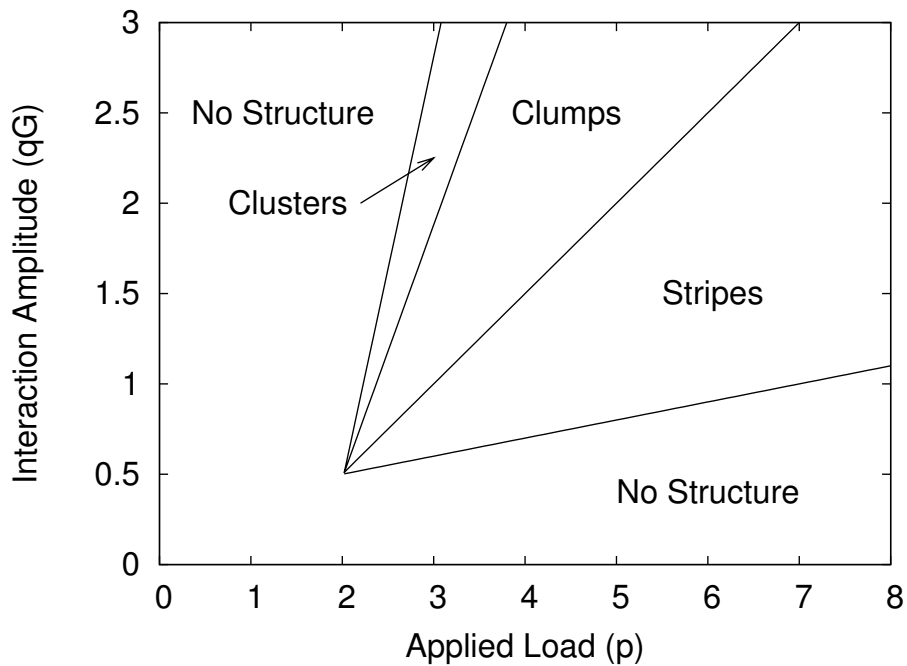


Figure 5.9: Here we plot an approximate phase diagram for the formation of stripes and clumps of positive offset for fixed parameters $\gamma = 1$, $b = 1e - 4$ and at low temperatures approaching $T \rightarrow 0$. These periodic structures occur by a symmetry breaking phase transition only for positive or repulsive interactions, $G > 0$. We normalize the interaction amplitude to the number of neighbors q . The location of the phase boundaries was determined by testing many parameter sets within the phase space.

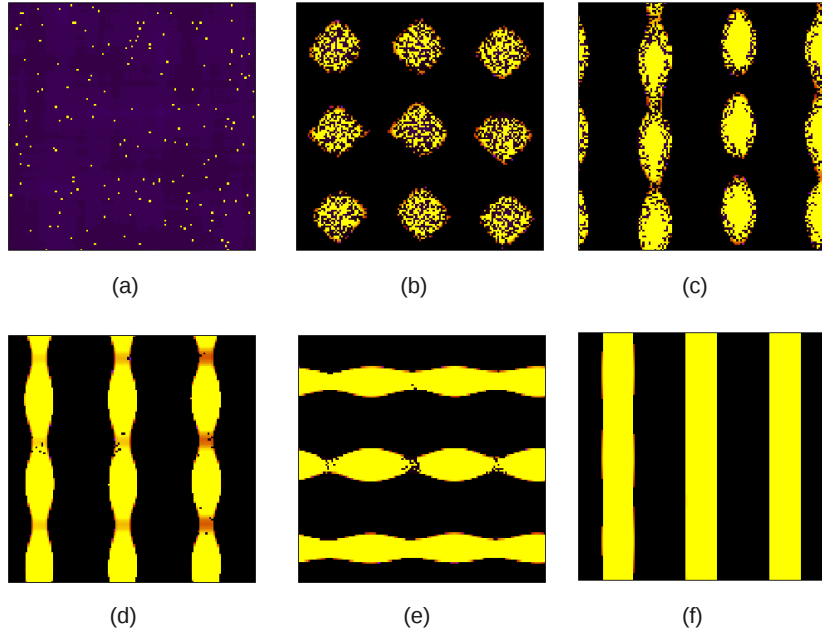


Figure 5.10: Here we show the final state of the system after a phase transition has occurred using repulsive interactions. We set the interaction amplitude to $G = 3$ and $b = 1e - 4$. We increase the applied load from the case where only random sites form percolation-type clusters, to that in which the final state is solid well defined stripes. All the final states depicted here are represented in the phase diagram in Fig. 5.9.

decays into single site clumps or nodes located at the center of the decaying clumps. The single site nodes are a stable spatial structure.

5.6.3 $b \neq 0, \gamma < 0$

As noted in Sec. 5.3, the cohesion parameter is bounded on the positive side by the coefficient b of the quartic term. However, there is no restraint on allowing negative cohesion. A negative cohesion contributes to the applied load term of the free energy and promotes growth of the offset field ζ . In our model, we interpret a positive cohesion to represent brittle materials, while a negative cohesion can represent ductile materials. Nucleation of fracture droplets, when $G < 0$, is still allowed for negative γ but the process begins at much lower applied loads. For all $\gamma < 0$ there is a non-zero stable offset for zero applied load. If the magnitude of γ is on the order of p and

G as was the cases above, there are still final stable states that appear as “clumps” and “stripes”.

5.7 Summary and Discussion

We have presented a 2D fracture model with dynamics governed by a free energy originally proposed in [16]. We introduce a modification to this free energy and investigate the phase transitions allow for both positive and negative interaction coefficients. We outline the linear CHC theory as applied to our model and show that phase transitions in our model is analogous to those in Ising model after off-critical quenches. Our model displays nucleation of fracture droplets with nucleation rates dependent on the proximity to the spinodal. Under slow-loading conditions we have found the model to exhibit linear-elastic behavior. Using the repulsive or anti-ferromagnetic interactions, our model displays two types of symmetry breaking phase transitions. These phase transitions result in either periodic clumps or stripes of positive offset.

We interpret these periodic structures in light of shear failure. It has been shown that if rapid loads are applied, inducing mode III fractures in ductile materials, shear banding can occur. These bands are regions of increased strain. The periodic “stripe” phase of the model presented here can be interpreted as a representation of shear bands. Redefining the interaction parameter G to be a function of temperature in which the sign changes as a transition temperature is crossed, allows the interpretation of a transition from a brittle to ductile material. The brittle material will have a negative G in which fracture occurs via nucleation of fracture droplets and the ductile material will allow shear bands that appear as a symmetry breaking phase transition. We plan to follow up on defining this ductile-brittle transition temperature within the model.

This model is the foundation of further research to understand the fracture nucleation process in materials with damage and defects. A modification of this type might be to vary the values of γ and G for the damaged sites. The cohesion for a damaged site will be reduced and influence on neighboring sites to grow might be increased in close proximity of the damaged site. Following the Monte Carlo procedures above fracture should occur at lower applied loads for systems with substantial damage, and nucleation times should be lowered in comparison to the undamaged systems for constant loads. Nucleation sites should also tend to align with the damaged sites. It is also of interest to see how the periodicity of the stripes and clumps is affected by inclusion of damaged sites.

5.8 References

- [1] J. K. Gran, Y. M. Gupta, and A. L. Florence. An experimental method to study the dynamic tensile failure of brittle geologic materials. *Mechanics of Materials*, 6:113–125, 1987.
- [2] O. Katz and Z. Reches. Microfractureing, damage, and failure of brittle granites. *J. Geophys. Res.*, 109, 2004. doi: doi:10.1029/2002JB001961d.
- [3] H. Néchad, A. Helmstetter, R. E. Guerjouma, and D. Sornette. Andrade and critical time-to-failure laws in fiber-matrix composites: Experiments and models. *J. Mech. Phys. Sol.*, 53: 1099–1127, 2005.
- [4] J. B. Rundle, W. Klein, and S. Gross. Dynamics of a traveling density wave model for earthquakes. *Phys. Rev. Lett.*, 76:4285–4288, 1996.
- [5] W. Klein, J. B. Rundle, and C. D. Ferguson. Scaling and nucleation in models of earthquake faults. *Phys. Rev. Lett.*, 78:3793–3796, 1997.
- [6] X. Lei and T. Satoh. Indicators of critical point behavior prior to rock failure inferred from pre-failure damage. *Tectonophysics*, 431:97–111, 2007.
- [7] A. V. M. Herz and J. J. Hopfield. Earthquake cycles and neural reverberations: collective oscillations in systems with pulse-coupled threshold elements. *Phys. Rev. Lett.*, 75:1222–1225, 1995.
- [8] Tobias Preis and H. Eugene Stanley. Trend switching processes in financial markets. In Misako Takayasu, Tsutomu Watanabe, and Hideki Takayasu, editors, *Econophysics Approaches to Large-Scale Business Data and Financial Crisis*, pages 3–26. Springer Japan, 2010.
- [9] Alan R. Fersht. Nucleation mechanisms in protein folding. *Current Opinion in Structural Biology*, 7(1):3 – 9, 1997.
- [10] Boris S. Kerner. Congested traffic flow: Observations and theory. *Transportation Research Record*, 1678:160–167, 1997.
- [11] Douglas A. Dodge, Gregory C. Beroza, and W. L. Ellsworth. Foreshock sequence of the 1992 lander, california, earthquake and its implications for earthquake nucleation. *J. Geophys. Res.*, 100(B6):9865–9880, 1995.

- [12] Robin L. Blumberg Selinger, Zhen-Gang Wang, William M. Gelbart, and Avinoam Ben-Shaul. Statistical-thermodynamic approach to fracture. *Phys. Rev. A*, 43(8):4396–4400, 1991.
- [13] W. Klein, M. Anghel, C. D. Ferguson, J. B. Rundle, and J. S. Sa Martins. Statistical analysis of a model for earthquake faults with long-range stress transfer. In J. B. Rundle, D. L. Turcotte, and W. Klein, editors, *Geocomplexity and the Physics of Earthquakes*, Geophysical Monograph 120, pages 43–71. American Geophysical Union, Washington D.C., 2000.
- [14] K. Barros, R. Dominguez, and W. Klein. Beyond cahn-hilliard-cook ordering theory: Early time behavior of spatial-symmetry-breaking phase transition kinetics. *Phys. Rev. E*, 79: 042104, 2009.
- [15] R. Dominguez, K. Barros, and W. Klein. Early time kinetics of systems with spatial symmetry breaking. *Phys. Rev. E*, 79:041121, 2009.
- [16] J. B. Rundle and W. Klein. Nonclassical nucleation and growth of cohesive tensile cracks. *Phys. Rev. Lett.*, 63:171–174, 1989.
- [17] D. Thirumalai, R. D. Mountain, and T. R. Kirkpatrick. Ergodic behavior in supercooled liquids and in glasses. *Phys. Rev. A*, 39(7):3563–3573, 1989.
- [18] D. Thirumalai and R. D. Mountain. Ergodic convergence properties of supercooled liquids and glasses. *Phys. Rev. A*, 42:4574–4587, 1990.
- [19] J. D. Gran, J. B. Rundle, D. L. Turcotte, J. R. Holliday, and W. Klein. A damage model based on failure threshold weakening. *Physica A*, 390:1269–1278, 2011.
- [20] K. F. Tiampo, J. B. Rundle, W. Klein, J. S. Sá Martins, and C. D. Ferguson. Ergodic dynamics in a natural threshold system. *Phys. Rev. Lett.*, 91:238501, 2003.
- [21] K. F. Tiampo, J. B. Rundle, W. Klein, J. Holliday, J. S. Sá Martins, and C. D. Ferguson. Ergodicity in natural earthquake fault networks. *Phys. Rev. E.*, 75:066107, 2007.
- [22] L. Monette, W. Klein, and M. Zuckermann. Monte carlo study of the effect of perturbations on critical droplets. *J. Stat. Phys.*, 66:117–132, 1992.
- [23] C. A. Serino, W. Klein, and J. B. Rundle. Cellular automaton model of damage. *Phys. Rev. E*, 81(1):016105, Jan 2010. doi: 10.1103/PhysRevE.81.016105.

- [24] G. Yakovlev, J. D. Gran, D. L. Turcotte, J. B. Rundle, J. R. Holliday, and W. Klein. A damage-mechanics model for fracture nucleation and propagation. *Theoretical and Applied Fracture Mechanics*, 53:180–184, 2010.

